Title	金属-半導体界面層あるいは絶縁体-半導体界面層を用いたAlGaN/GaNデバイスの閾値電圧制御
Author(s)	DENG, YUCHEN
Citation	
Issue Date	2024-06
Type	Thesis or Dissertation
Text version	ETD
URL	http://hdl.handle.net/10119/19335
Rights	
Description	Supervisor: 鈴木 寿一, 先端科学技術研究科, 博士

Doctoral dissertation

Threshold voltage modulation in AlGaN/GaN devices using metal-semiconductor or insulator-semiconductor interfacial layers

YUCHEN DENG

Supervisor: Toshi-kazu SUZUKI

Graduate School of Advanced Science and Technology

Japan Advanced Institute of Science and Technology

Materials Science

June, 2024

Abstract

We have systematically investigated effects of metal-semiconductor or insulator-semiconductor interfacial layers (ILs) in AlGaN/GaN devices, where AlO_x, TiO_x, or NiO_x is employed as an IL. From capacitance-voltage characteristics of metal/IL/AlGaN/GaN devices with a metal-semiconductor IL between the gate metal and AlGaN, it is shown that the IL modulates the threshold voltage V_{th}, attributed to the vacuum level step induced by the dipole of the IL. We find negative vacuum level steps for AlO_x and TiO_x ILs, and positive for NiO_x, from which the IL dipole density is estimated for each IL material. The two-dimensional electron gas carrier concentration in the metal/IL/AlGaN/GaN devices is also modulated by the vacuum level step. Furthermore, X-Ray photoelectron spectroscopy of the IL/AlGaN interfaces suggest a formation of NiGa in the NiO_x/AlGaN interface. On the other hand, from capacitance-voltage characteristics of metal/Al_2O_3/IL/AlGaN/GaN devices with an insulator-semiconductor IL between Al_2O_3 and AlGaN, the fixed charge density of the Al_2O_3/IL/AlGaN interface is evaluated by the Al_2O_3 thickness dependence of V_{th}. For AlO_x and TiO_x ILs, the fixed charge density is higher than that of the Al_2O_3/AlGaN interface with no IL, while lower for NiO_x. The fixed charge density for an IL shows a positive correlation with the IL dipole density, suggesting that the fixed charge is related to the unbalanced IL dipole. Furthermore, using the conductance method, we find a low trap density of the Al_2O_3/IL/AlGaN interface for AlO_x and NiO_x ILs, in comparison with that of the Al_2O_3/AlGaN interface with no IL.

Keywords: AlGaN/GaN device, interfacial layer, threshold voltage control, vacuum level step, fixed charge

Contents

Chapter 1

Introduction

1.1 Compound semiconductor Gallium nitride (GaN)

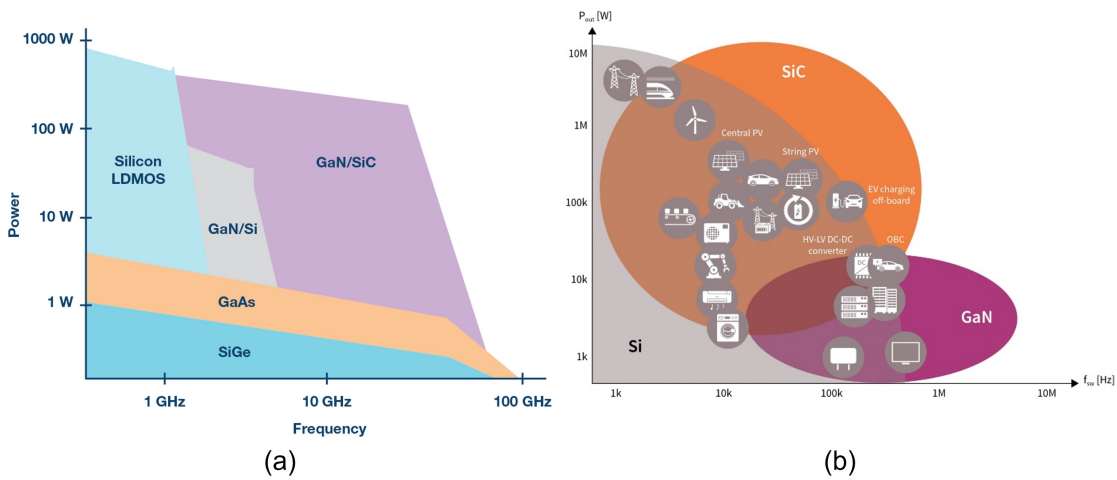

Figure 1.1: Relations between frequency and power for (a) wireless-communication applications [1] and (b) power-switching applications [2].

Compound semiconductor is important in high-speed wireless-communication and/or high-power switching. Figure 1.1(a) shows the relation between power and frequency requirements for several wireless-communication applications [1], where each semiconducting material has a suitable application based on its physical properties. For examples, Si-based transistors [3] are widely employed in mo-

bile communications, which require a middle range frequency $\sim$ 1G Hz and a power $\sim$ 1-1000 W. Meanwhile, GaAs-based transistors [4, 5] are employed for radar communications, where working frequencies are up to $\sim$ 100G Hz. In future wireless-communication, devices being capable for both high-speed and high-power applications are important [6]. Figure 1.1(b) shows the requirements for power-switching applications [2], where the frequency range is downscale by 10^5 orders while the power range is upscale by the same orders compare to Fig. 1.1(a). In these applications, the semiconductor devices are required to to handle a large power, and a moderate switching speed is also required depending on the application. However, there is a trade-off between speed (frequency) and power for both high-speed and high-power applications, which means that the devices can operate at high frequency are unlikely to be capable for high-power applications, and vice versa. Gallium Nitride (GaN), a Ⅲ-V compound semiconductor, shows potentials to overcome this trade-off. GaN, a nitride compound semiconductor, has potentials to overcome this trade-off.

In order to measure the suitability of a semiconducting materials for high-speed and high-power applications, we employ two types of figure of merit (FoM) in the following. The first one is Johnson's FoM, which is given by

$$f_{\mathrm{T}} V_{\mathrm{Br}} \leq \frac{F_{\mathrm{Br}} v_{\mathrm{sat}}}{2\pi}, \tag{1.1}$$

where f_{T} is the cut-off frequency, F_{Br} is the breakdown field, and V_{Br} is the breakdown voltage. Figure 1.2(a) shows the relation between V_{Br} and f_{T}, indicating that GaN is superior than Si or GaAs in both breakdown voltage and cut-off frequency.

The other FoM is Baliga's, which is given by

$$\epsilon_0 k \mu F_{\mathrm{br}}^3 \geq \frac{4V_{\mathrm{br}}^2}{R_{\mathrm{on}}}, \tag{1.2}$$

where ϵ_0 is the vacuum permittivity, k is the dielectric constant of the semiconducting material, and R_{on} is the on-resistance. The relation between R_{on} and V_{br} for several semiconductors is depicted in Fig. 1.2(b). It is clear that GaN with relatively low R_{on} at high V_{Br} in comparison with other semiconducting materials.

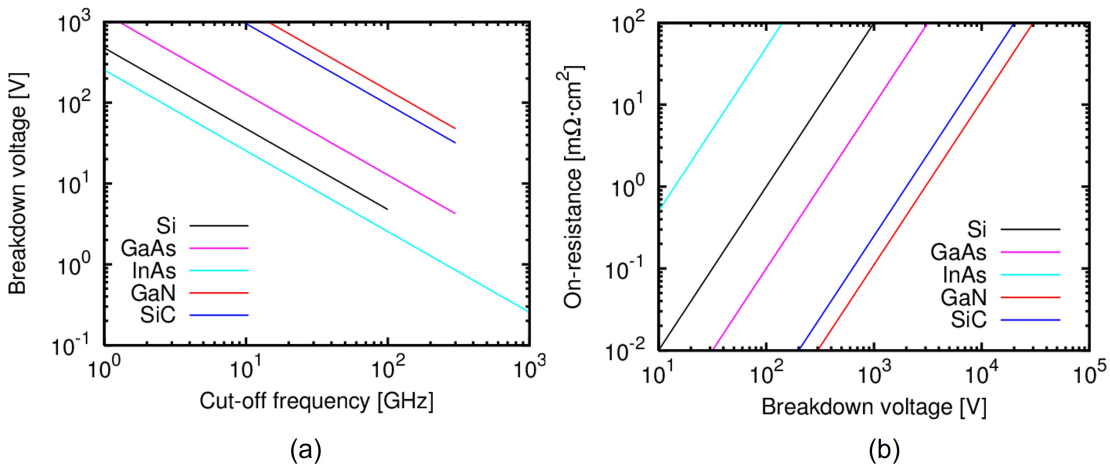

Figure 1.2: (a) Relation between V_{Br} and f_{T} for several semiconductors. (b) Relation between R_{on} and V_{Br} for several semiconductors.

In high-power applications, the applied source-drain voltage is high. Moreover, due to the decrease in the gate length, the electric field under the gate becomes stronger, leading to earlier breakdown of the semiconductor. Therefore, materials with high breakdown field are advantageous for power-handling applications. The breakdown field F_{Br} of a semiconductor is usually related to its energy gap E_{g} by the relation

$$F_{\mathrm{Br}} \propto E_{\mathrm{g}}^{\alpha}, \tag{1.3}$$

where $\alpha \simeq$ 1-3, making F_{Br} an increasing function of E_{g} [7]. Therefore, for high-power applications, wide band gap semiconductors are preferable. Figure 1.3 shows the relation between the energy gap and the lattice constant for several semiconductors [8, 9], where we can find that GaN has a large band gap E_{g} of 3.4 eV, corresponding to a very high breakdown field of 3.3 MV/cm. These properties indicate that GaN is a favorable semiconductor for high-power applications.

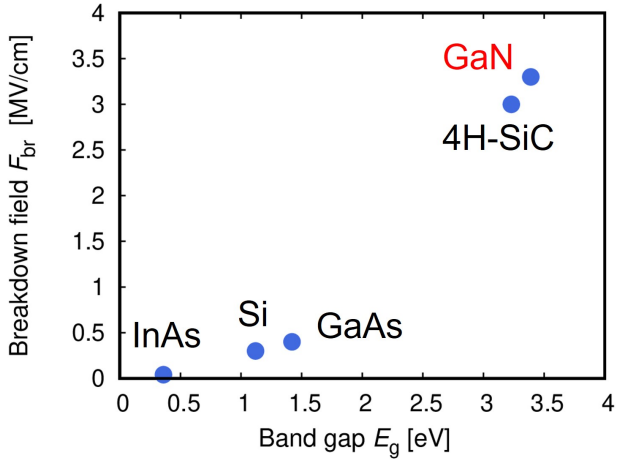

Figure 1.3: The breakdown field F_{br} as a function of the band gap E_{g} for several semiconductors [8, 9].

On the other hand, there is a trend of proportional relation [10]

$$m_{\Gamma}^{*} \propto E_{\mathrm{g}}^{\alpha}, \tag{1.4}$$

which leads to a relatively large effective mass $m^{*} = 0.20$ for GaN as shown in Figure 1.4.

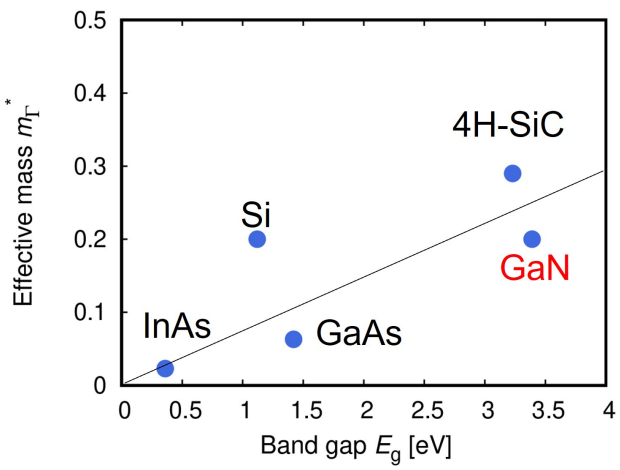

Figure 1.4: The effective mass m_{Γ}^{*} at Gamma point as a function of the band gap E_{g} for several semiconductors.

The effective mass m^{*} affects the electron transport in semiconductors. The

carrier velocity in a FET v is determined by the drift velocity v_{d} at low electric field and the saturation velocity v_{sat} at high electric field as shown in Figure 1.5.

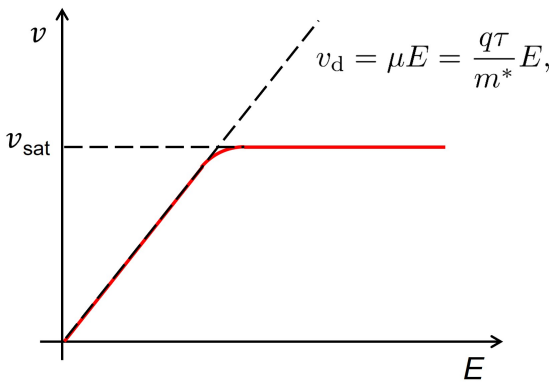

Figure 1.5: Carrier velocity v as a function of the electric field.

The drift velocity at low electric field is

$$v_{\mathrm{d}} = \mu E = \frac{q\tau}{m^*}E, \tag{1.5}$$

where μ is the electron mobility, $q > 0$ is the electron charge, τ is the scattering time, m^* is the electron effective mass, and E is the electric field. At low electric field, v in a material is directly proportional to the electric field, where the slope is the electron mobility μ. Thus a high mobility leads to a high drift velocity. Meanwhile, at high electric field, carriers have high enough kinetic energy to emit optical phonons between collisions, leading to a decrease in velocity and a consequent prohibition in further acceleration. The saturation velocity, which is the velocity a carrier can reach before emitting a phonon, is given by

$$v_{\mathrm{sat}} = \sqrt{\frac{2\hbar\omega_{\mathrm{op}}}{m^*}}, \tag{1.6}$$

where $\hbar\omega_{\mathrm{op}}$ is the optical phonon energy. From Eq. (1.5) and (1.6), we find that both v_{d} and v_{sat} are proportional to $1/m^*$, thus materials with small m^* are advantageous for high-speed applications.

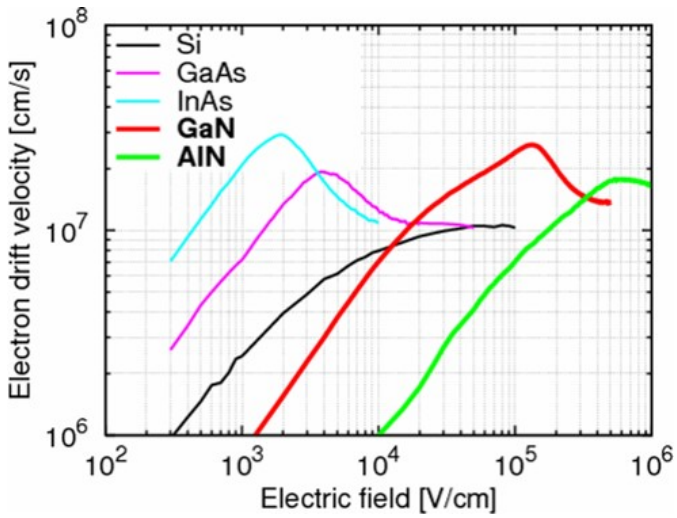

Figure 1.6: Relation between drift velocity and electric field obtained by Monte Carlo simulation [11].

Figure 1.6 shows the electron drift velocity as functions the electric field for several semiconductors obtained by Monte Carlo simulation [11]. For GaN, the relatively large m^* leads to a relatively low mobility, and a consequent low electron velocity in low-field region. However, in high-field region, GaN possesses a high electron peak velocity of 2.5×10^7 cm/s and a high electron saturation velocity $\geq 1.5 \times 10^7$ cm/s as expected, owing to a large optical phonon energy $\hbar\omega_{\mathrm{op}} \simeq 90$ meV, and a large valley-separation energy.

A large valley-separation energy ΔE can suppress the transferred-electron effect, depicted in Fig. 1.7. The energy difference between the upper valley and the lower valley in the conduction band known as the valley-separation energy ΔE. A small ΔE leads to a easier transition from the lower valley with a higher mobility, to the upper valley with a lower mobility, resulting in a decrease in the total mobility, hence the carrier velocity. Figure 1.8 shows the calculated energy band structures of zinc-blende GaAs, InP, and wurtzite GaN [12, 13], where GaN shows a large valley-separation energy of $\Delta E = 1.4$ eV in comparison with that of GaAs $\Delta E = 0.32$ eV and InP $\Delta E = 0.52$ eV, leading to a higher saturation velocity v_{sat} for GaN.

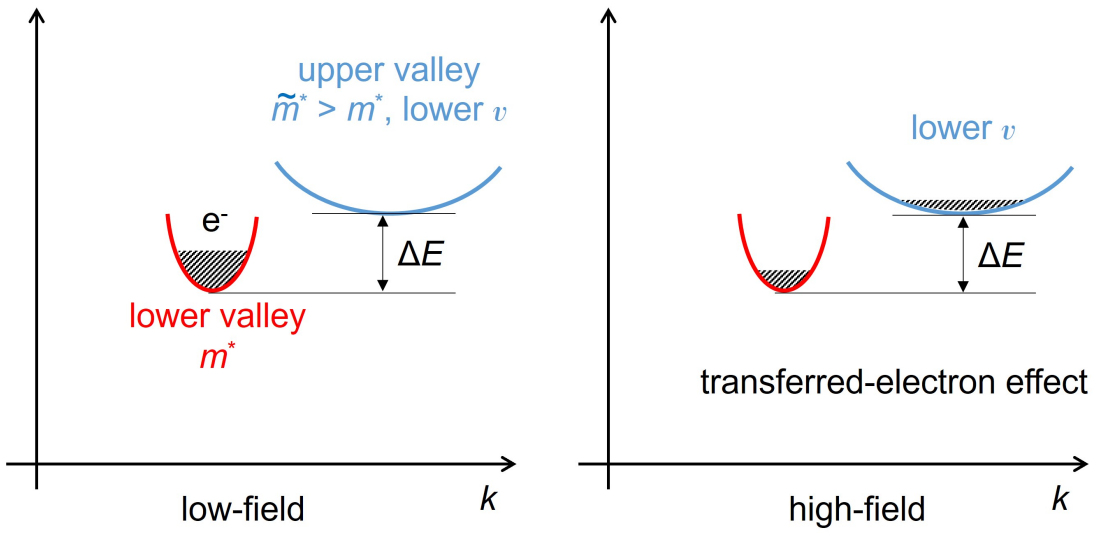

Figure 1.7: The transferred-electron effect.

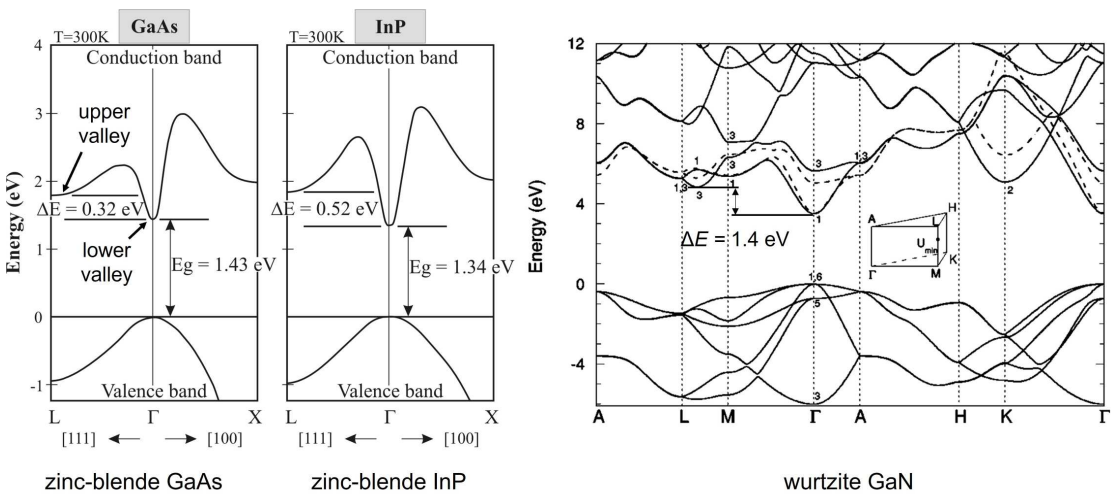

Figure 1.8: The calculated energy band structures of zinc-blende GaAs, InP, and wurtzite GaN [12, 13].

In addition to the electrical properties, thermal conductivity κ is also an important property of semiconductors, especially in the high-power application. When a FET operates with a drain current I_{D} under a drain-to-source voltage V_{DS}, temperature T in the channel of the FET increases owing to the Joule heating $P = I_{\mathrm{D}}V_{\mathrm{DS}}$ as shown in Fig. 1.9(a), known as the self-heating. The increase in T

leads to a reduction in electron velocity, causing a negative drain conductance [14]

$$g_{\mathrm{D}} = \partial I_{\mathrm{D}}/\partial V_{\mathrm{DS}} < 0 \tag{1.7}$$

in the DC output characteristics of the FET shown in Fig. 1.9(b) [15], which is unfavorable in device application. In order to suppress the self-heating, high-κ semiconductor is desirable, where GaN is the case with a κ of $\sim$ 130 $\mathrm{WK^{-1}m^{-1}}$ [16].

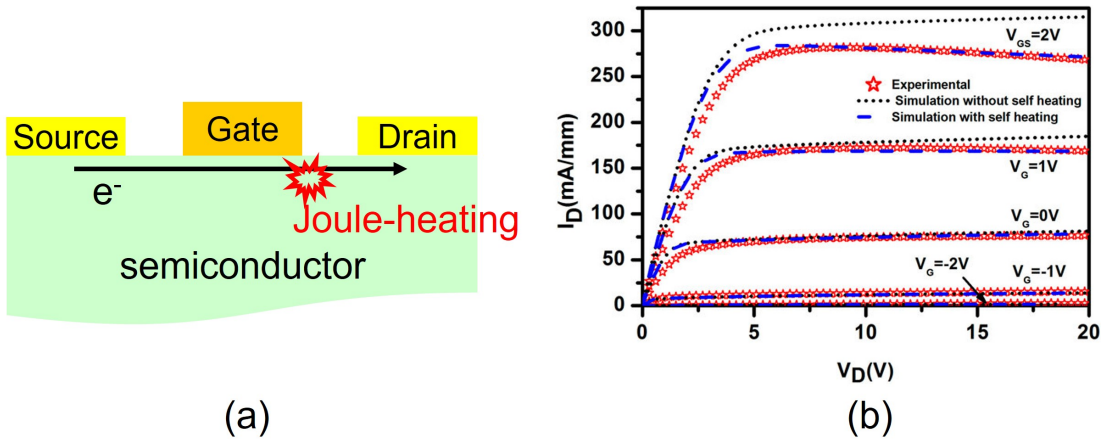

Figure 1.9: (a) Joule-heating in FETs. (b) Output characteristic of a FET considering the self-heating[15].

We summarize the physical properties for several semiconducting materials in Table 1.1, showing that GaN is a promising material owing to its high saturation velocity, wide band gap and relatively high thermal conductivity.

Table 1.1: Comparison of properties between GaN and other semiconductors.

Mater.	E_g [eV]	μ [cm^2/V.s]	v_{sat} velocity [cm/s]	F_{Br} [V/cm]	κ [W/K.m]
Si	1.12	1500	1.0 $\times 10^7$	3.0 $\times 10^5$	$\sim$ 200-400
GaAs	1.42	8500	2.0 $\times 10^7$	4.0 $\times 10^5$	$\sim$ 50
InAs	0.36	33000	$\sim 4.0 \times 10^7$	4.0 $\times 10^4$	$\sim$ 30
SiC	3.33	900	2.0 $\times 10^7$	3.0 $\times 10^6$	$\sim$ 200-300
GaN	**3.39**	**1100**	$\mathbf{2.7 \times 10^7}$	$\mathbf{3.3 \times 10^6}$	$\sim$ **130**

1.2 AlGaN/GaN heterostructures

In addition to the properties discussed above, GaN can form a heterostructure with AlGaN, which is a alloy of GaN and AlN, leading to further applications. In the AlGaN/GaN heterostructure, spontaneous and piezoelectric polarization are critical [17, 18]. The spontaneous polarization P_{sp} comes from an intrinsic asymmetry of the bonding in equilibrium wurtzite crystal structures of GaN or AlN as shown in Fig. 1.10(a). In a geometrically ideal wurtzite structure, the close-packed structure leads to a lattice constant ratio $c/a = 1.633$ as shown in Fig. 1.10(b). However, due to ionicity of Ga and N ions, the c-axis is distorted in the real GaN wurtzite structure, leading to a $\tilde{c}/a = 1.623$ as shown in Fig. 1.10(c). This distortion leads to a net total polarization, so called the spontaneous polarization, which would have been canceled out in the geometrically ideal case.

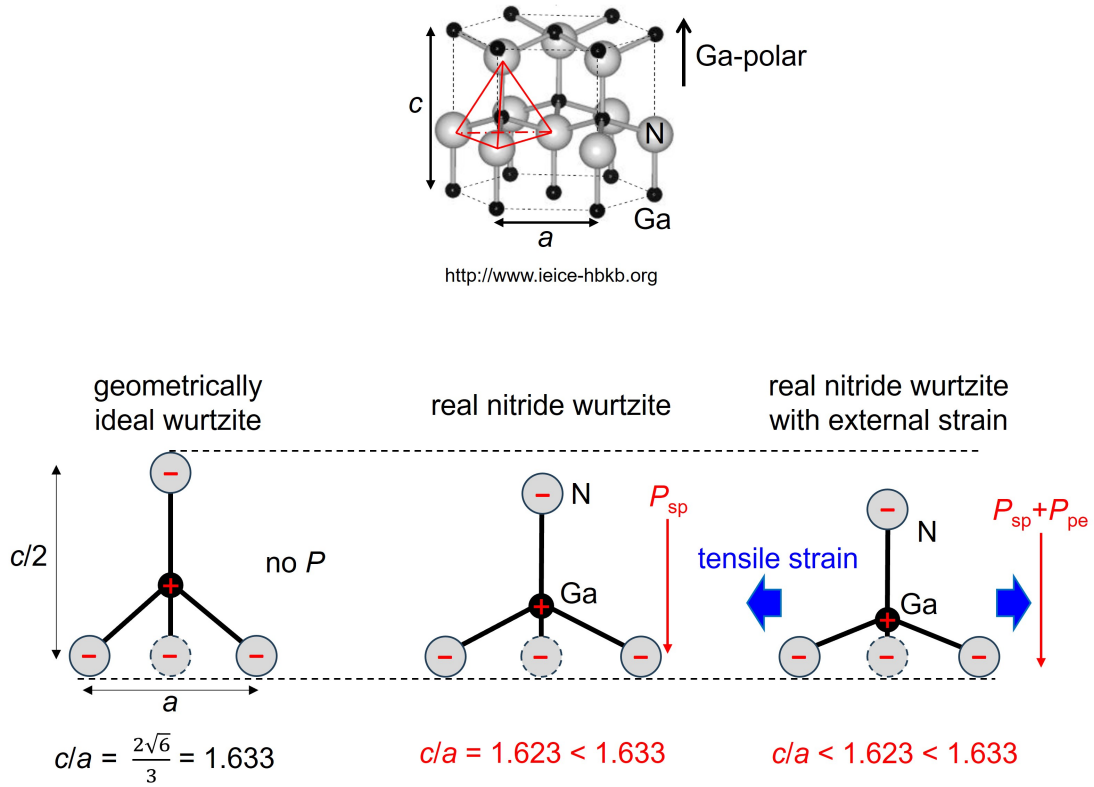

Figure 1.10: The GaN wurtzite structure and its distortion in real case.

On the other hand, the piezoelectric polarization P_{pe} origins from mechanical stress, i.e. tensile or compressive strain of AlGaN and GaN layers, shown in Fig. 1.12 as a consequence of the formation of AlGaN/GaN heterostructure. Al(Ga)N has a smaller lattice constant than GaN as shown Fig. 1.11, leading to a lattice constant mismatch between AlGaN and GaN. In order to compensate this mismatch, the AlGaN layer is compressed, resulting in an extra net polarization, so called the piezoelectric polarization.

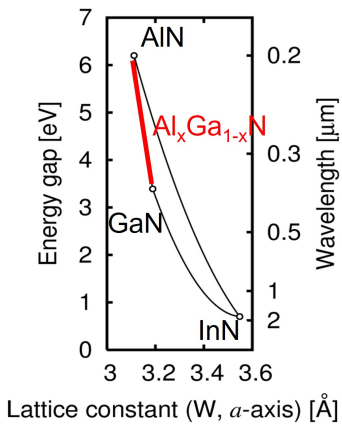

Figure 1.11: The energy gap and corresponding wavelength as functions of the lattice constant for several III-V compound semiconductors [8, 9].

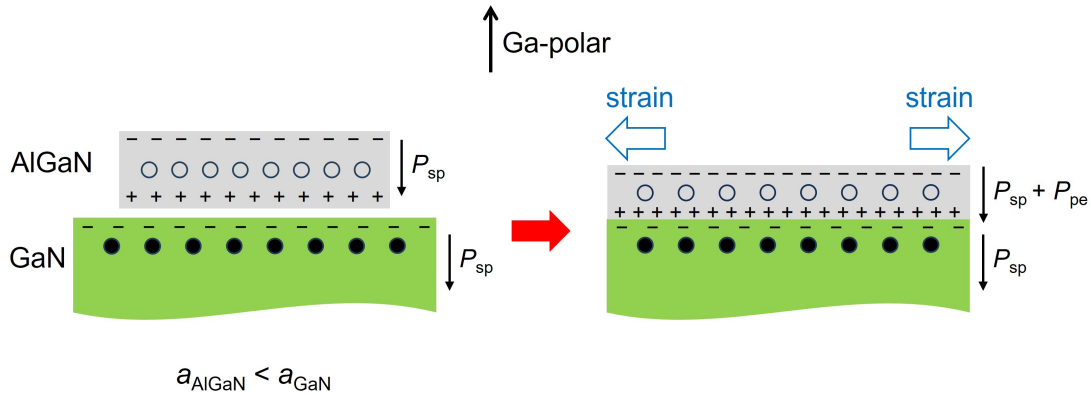

Figure 1.12: The formation of AlGaN/GaN heterostructure, where the AlGaN layer is compressed to compensate the lattice constant mismatch.

These two polarizations lead to a two-dimensional electron gas (2DEG) with high concentration at AlGaN/GaN heterointerface as shown in Fig. 1.13 [18]. Typically, an Al composition of 20-30% gives a 2DEG concentration $\simeq 10^{13}$ cm^{-2}, which can be utilized as the channel of a AlGaN/GaN Schottky FET. Such FETs, namely the AlGaN/GaN high electron mobility transistors (HEMT), whose schematic is shown in Fig. 1.14(a), are widely investigated for high-speed and high-power applications [19]. However, high gate leakage current despite of wide band gap [20–23] and current collapse due to surface electron trapping [24–26] still occur in AlGaN/GaN Schottky FETs. In order to solve these problems, AlGaN/GaN metal-insulator-semiconductor (MIS) FETs, whose schematic is shown

in Fig. 1.14(b), have been investigated according to the advantages of gate leakage reduction [23] and passivation to suppress the current collapse [24–26].

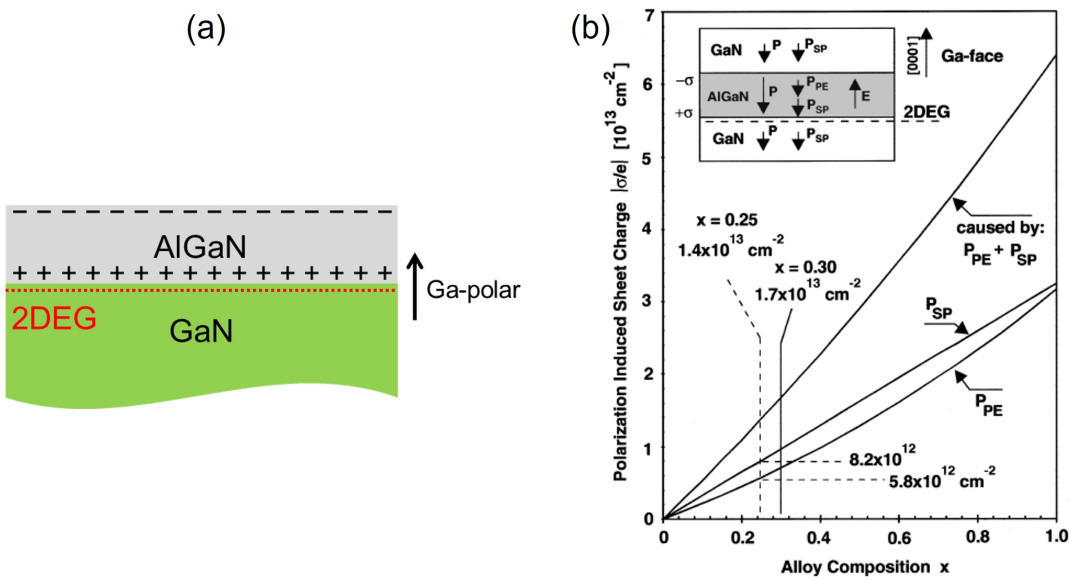

Figure 1.13: (a) The 2DEG at the AlGaN/GaN heterointerface. (b) Calculated sheet charge density caused by spontaneous and piezoelectric polarizations of a GaN-face GaN/AlGaN/GaN heterostructure [18].

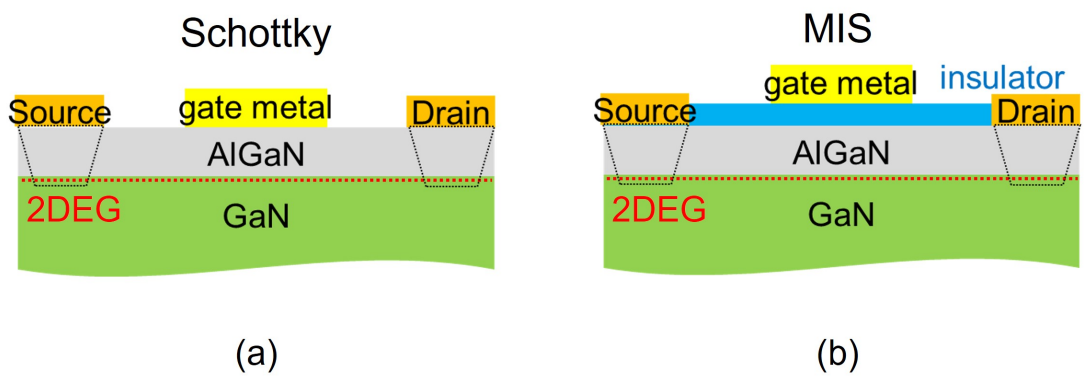

Figure 1.14: (a) A schematic cross section of AlGaN/GaN Schottky FETs. (b) A schematic cross section of AlGaN/GaN MIS FETs.

1.3 Threshold voltage control in AlGaN/GaN devices

The control of threshold voltage V_{th} is one of the most important issues in both Schottky and MIS FETs. Basically, V_{th} of a FET is the minimum gate-to-source voltage V_{G} that is necessary to create a conducting channel between the source and drain electrodes. Drain current I_{D} and carrier density n_{s} in the FET channel are proportional to the difference between V_{G} and V_{th} in GaN-based semiconductor devices:

$$I_{\mathrm{D}} \propto n_{\mathrm{s}} \propto (V_{\mathrm{G}} - V_{\mathrm{th}}), \tag{1.8}$$

shown in Figure 1.15. In this case, V_{th} can be defined as the $I_{\mathrm{D}} = 0$ (n_{s})=0 intercept of the linear extrapolation for $I_{\mathrm{D}} - V_{\mathrm{G}}$ or $n_{\mathrm{s}} - V_{\mathrm{G}}$ relations. For different application, V_{th} with different value, or even different sign are demanded, making the control of V_{th} an important issue.

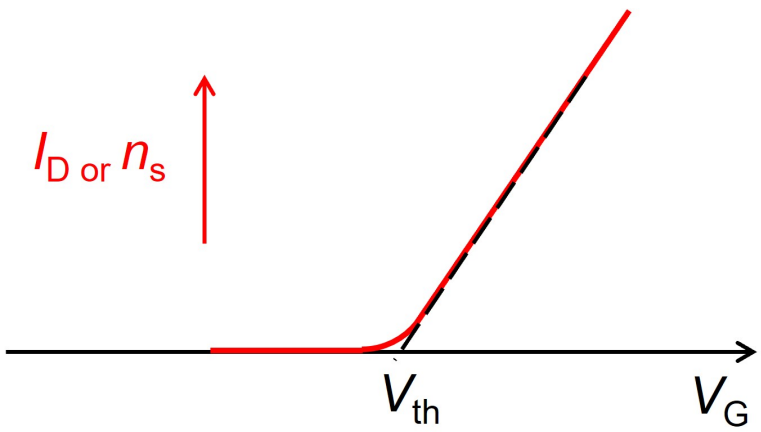

Figure 1.15: Typical I_{D} (n_{s})-V_{G} characteristics of GaN-based FETs.

Owing to the existence of 2DEGs, carrier density n_{s} in the channel of a AlGaN/GaN FET is > 0 at $V_{\mathrm{G}} = 0$, making the FET a normally-on devices with a I_{D}-V_{G} characteristic is shown in Fig. 1.16(a). However, in some applications, normally-off devices, whose I_{D}-V_{G} characteristic is shown in Fig. 1.16(b), are favorable from the viewpoint of fail-safe operations. Although there are several efforts to realize normally-off devices, such as partial gate recess [27], full gate recess

[28], fluoride plasma treatment [29], p-type (Al)GaN capping [30, 31], selective electro-chemical oxidation [32], and fin-structure formation [33], it is still difficult to establish normally-off device technology, in particular for a high positive V_{th}. Thus, the positive V_{th} modulation under gate-region is further important.

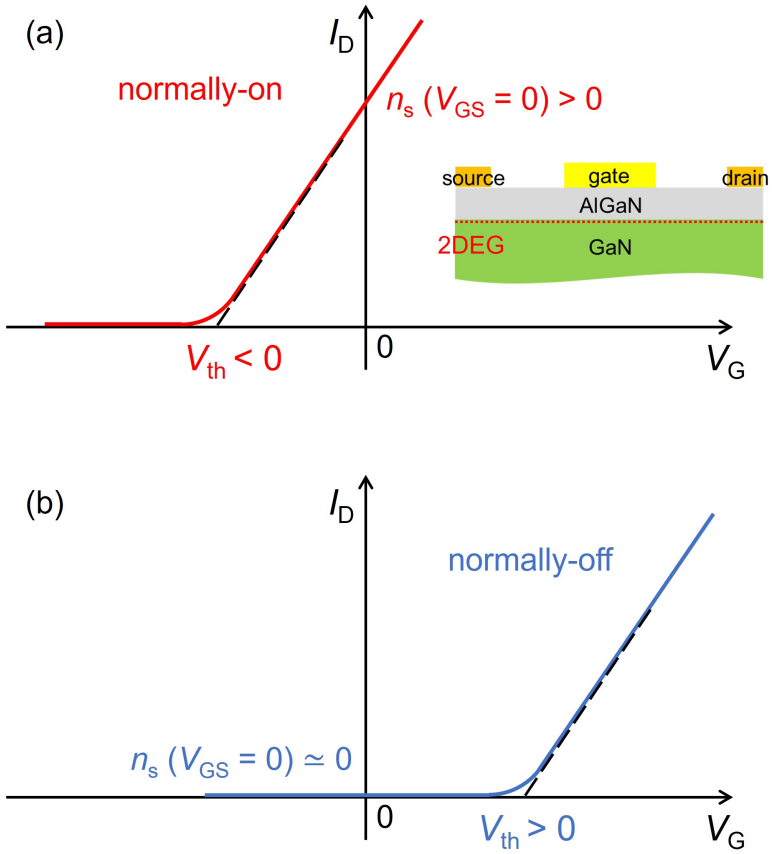

Figure 1.16: Typical I_{D} (n_{s})-V_{G} characteristics for (a)normally-on and (b)normally-off GaN-based devices.

On the other hand, since normally-off devices operates in forward bias region $V_{\mathrm{G}} > 0$, a normally-off AlGaN/GaN Schottky structure will exhibits serious gate leakage I_{G}. Meanwhile, due to the insulator insertion, a MIS structure can lead to effective gate leakage reduction as shown in Fig. 1.17. Figure 1.18 shows the gate leakage reduction by MIS structure. Therefore, for normally-off devices, MIS structure is necessary.

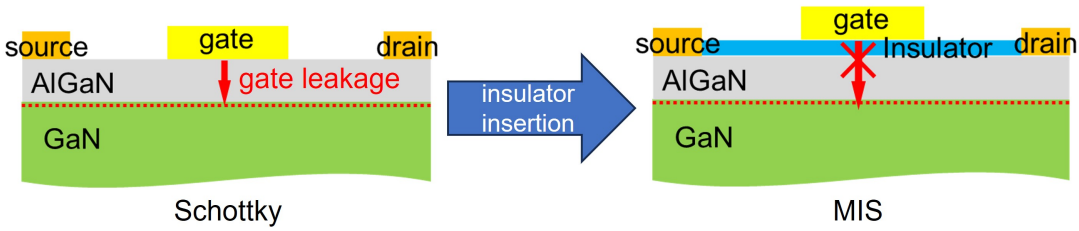

Figure 1.17: Schematic of gate leakage reduction in MIS devices.

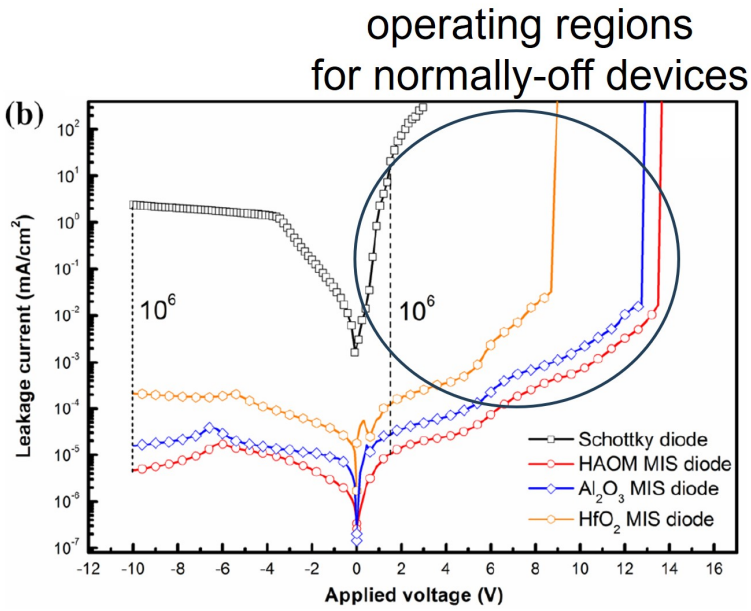

Figure 1.18: Comparison of gate leakage I_G between Shcottky and MIS devices.

1.4 Interfaces in AlGaN/GaN devices affecting the threshold voltage

In the AlGaN/GaN Schottky and MIS devices, the metal-semiconductor and insulator-semiconductor interfaces are important building blocks, affecting the threshold voltage V_{th} of the devices.

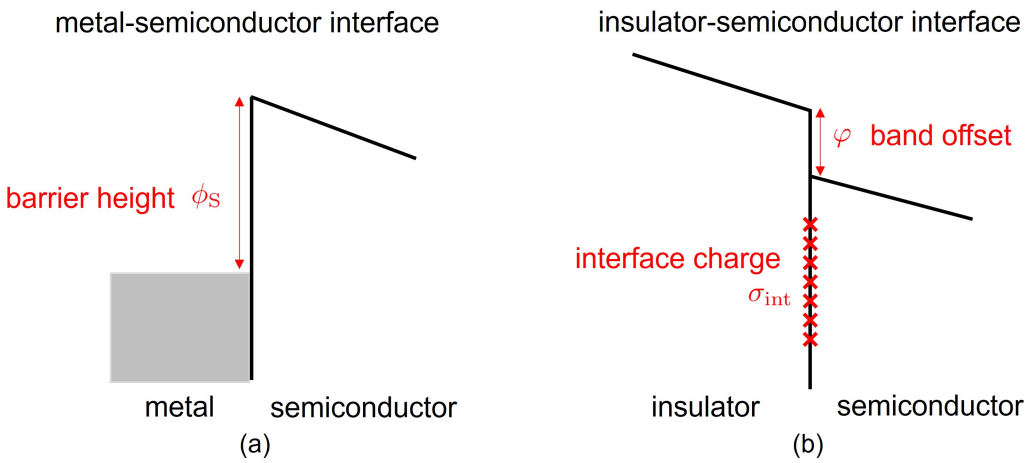

Figure 1.19: (a) The metal-semiconductor interface. (b) The insulator-semiconductor interface.

The metal-semiconductor interface

In the case of the Schottky devices, V_{th} is dominated by the metal-semiconductor barrier height ϕ_S shown in Fig. 1.20(a), which can be modulated by using metals with different work functions [34, 35]. However, in many cases of GaN-based Schottky contacts, the value of ϕ_S is not uniquely determined by the difference between the metal work function and the (Al)GaN electron affinity, and is affected by treatments of the metal-semiconductor interface [36–38]. Figure 1.20(b) shows an example, where treatments using HCl considerably modulated ϕ_S in GaN-based Schottky contacts. This indicates the existence of an unintentional metal-semiconductor interfacial layer, leading to a modulation of ϕ_S by a vacuum level step ΔE_{vac} due to a dipole of the interfacial layer [39].

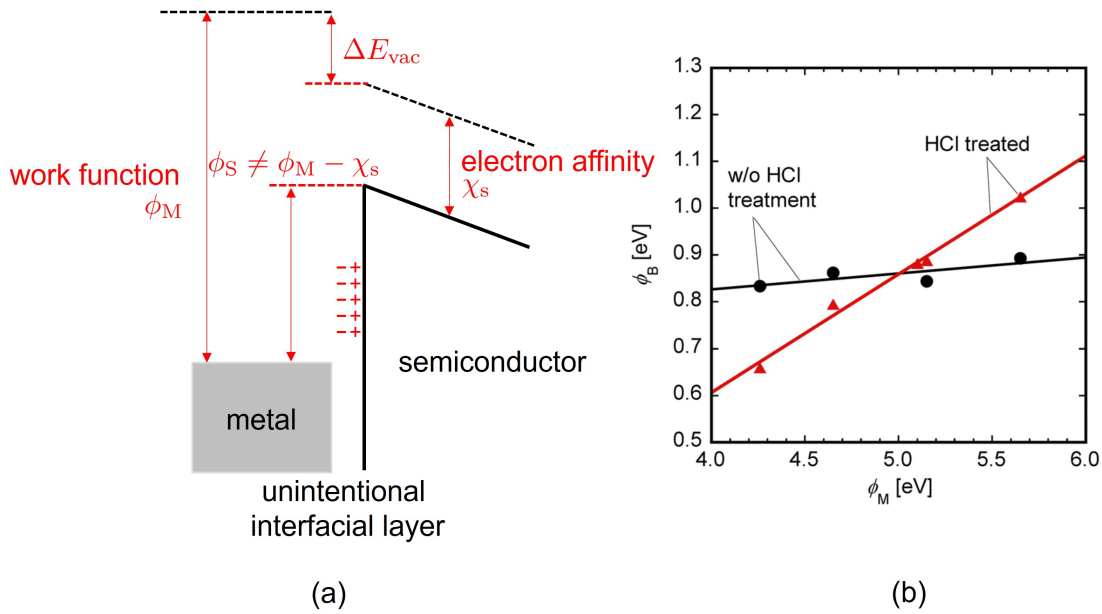

Figure 1.20: (a) The not uniquely determined metal-semiconductor barrier height. (b) Metal-semiconductor barrier height $\phi_{\rm B}$ as functions of metal work functions $\phi_{\rm M}$ for a metal/GaN interface. [38].

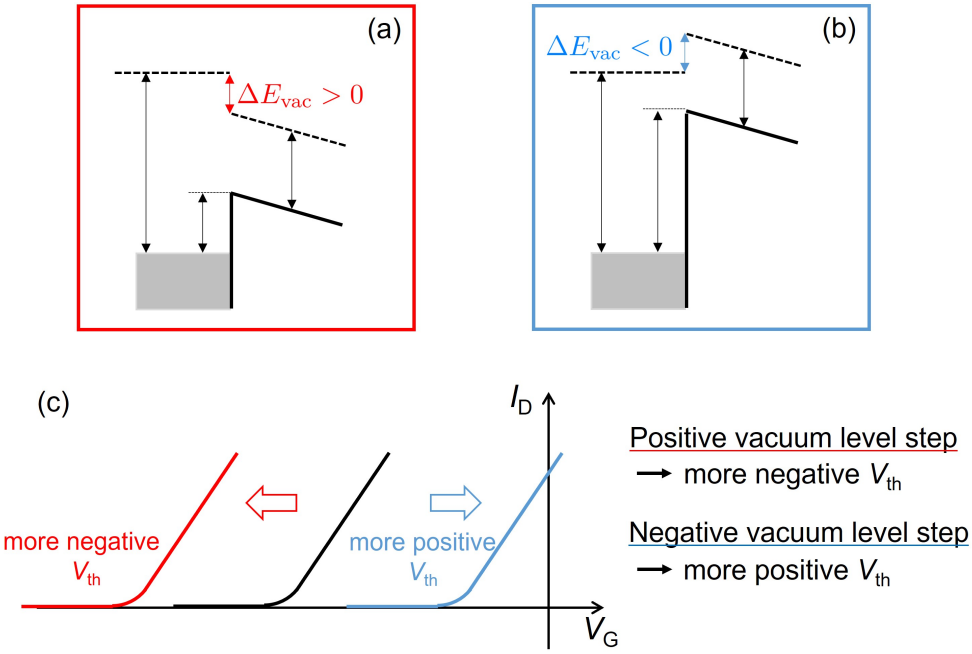

Figure 1.21: (a) A metal-semiconductor interface with a positive $\Delta E_{\rm vac}$. (b) A metal-semiconductor interface with a negative $\Delta E_{\rm vac}$. (c) The $V_{\rm th}$ shifts due to $\Delta E_{\rm vac}$.

Figure 1.21 shows the relation between the vacuum level step $\Delta E_{\rm vac}$ and the

threshold voltage V_{th}. A positive ΔE_{vac} leads to a deeper V_{th}, while a negative one does the opposite. Therefore, from the behavior of V_{th}, we can directly determine ΔE_{vac}.

The insulator-semiconductor interface

On the other hand, in the case of the MIS devices, V_{th} is affected by the insulator-semiconductor conduction band offset φ and the fixed charge density σ_{int} of the insulator-semiconductor interface, which are shown in Fig. 1.22(a). Various insulators such as oxides Al_2O_3 [40], HfO_2 [41, 42], TiO_2 [43], AlSiO [44, 45], AlTiO [46–52], oxynitrides TaON [53], AlON [54], and nitrides BN [55, 56], AlN [57–61] have been employed as a gate insulator for GaN-based devices, where V_{th} can be modulated by both φ and σ_{int}. Similarly to ϕ_{S}, φ is not uniquely determined by the electron affinity difference between the insulator and the semiconductor, and is affected by insulator-semiconductor interface treatments [62]. Figure 1.22(b) shows an example, where chlorine treatments modulated φ in ZnO/AlGaN contacts.

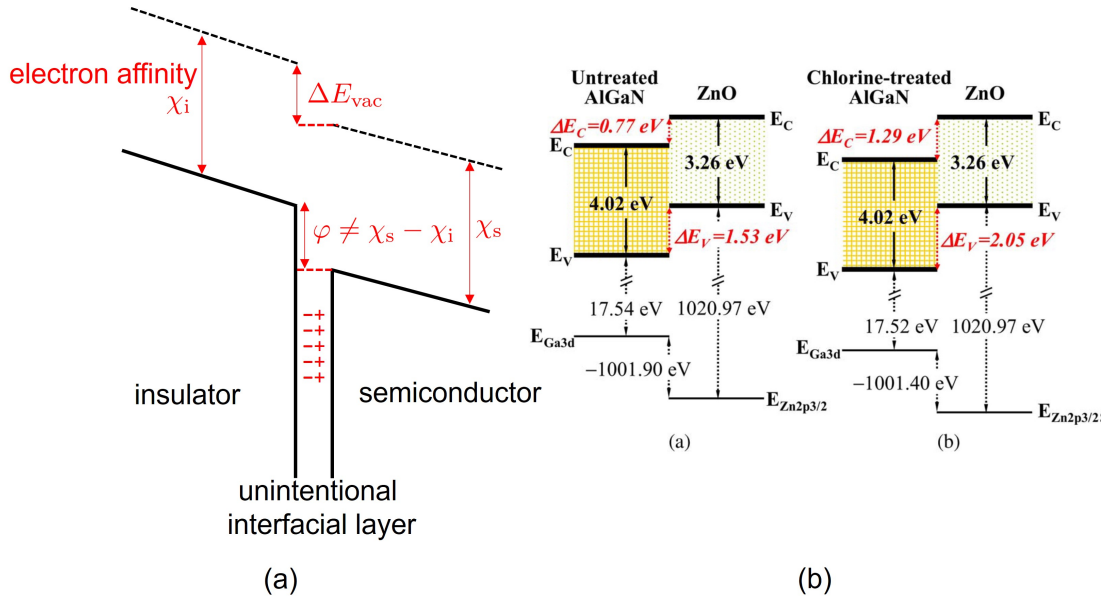

Figure 1.22: (a) The not uniquely determined insulator-semiconductor band offset. (b) ZnO/AlGaN band offset modulated by interface treatments [62].

Meanwhile, as shown in Fig. 1.23, when an insulator such as Al_2O_3 is deposited

on the Ga-polar (Al)GaN surface with a negative surface polarization charge, the fixed charge tends to be positive, neutralizing the polarization charge [63–70], while this is not always the case [51, 71, 72].

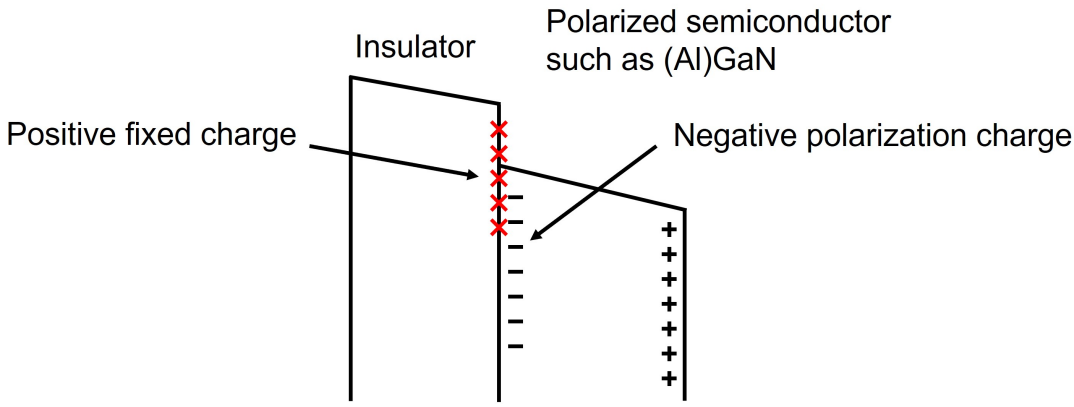

Figure 1.23: The positive fixed charge at insulator-semiconductor interface.

The band offset and positive fixed charge have significant impact on the threshold voltages V_{th}. Assuming no charges inside the insulator, V_{th} is a linear function of the insulator thickness d_{ins}, whose slope depends on the positive fixed charge density, and intercept at the $d_{\mathrm{ins}} = 0$ limit depends on the band offset as shown in Fig. 1.24(a). If the density of the positive fixed charge is high, leading to a band diagram shown in Fig. 1.24(b), V_{th} becomes more negative as d_{ins} increases. Meanwhile, if the density of the positive fixed charge is low, the electric field inside the insulator can be reverted as shown in Fig. 1.24(c), leading to a positive slope in V_{th}-d_{ins} relation. In other words, V_{th} will be more positive when d_{ins} increases. On the other hand, V_{th} intercept at $d_{\mathrm{ins}} = 0$ becomes deeper for larger band offset, and does the opposite for smaller one.

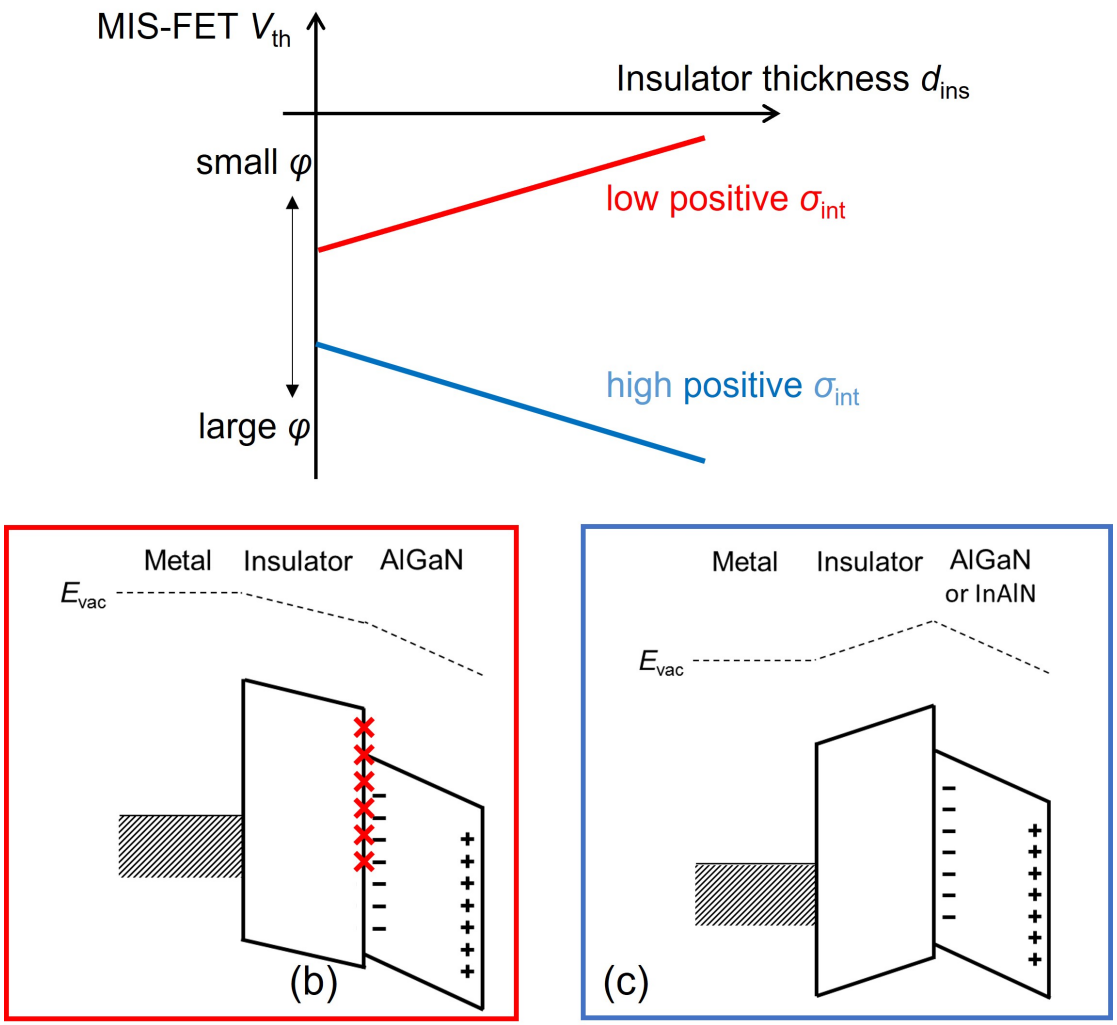

Figure 1.24: (a) V_{th} as functions of d_{ins}. Theoretical band diagram of AlGaN/GaN MIS devices where (b) fixed charge density is high, band offset is large and (c) fixed charge density is low, band offset is small.

Figure 1.25 shows examples where a high-density positive fixed charge of $10^{13}/\mathrm{cm}^2$ order has been observed, and the threshold voltage shifts negatively with increase in the insulator thickness. Even in fully recessed-gate normally-off devices, a high-density positive fixed charge of $10^{13}/\mathrm{cm}^2$ order has been observed, leading to a relatively low threshold voltage as shown in Fig. 1.26. On the other hand, when the positive interface charge is suppressed, positive threshold voltage shifts can be achieved as shown in Fig. 1.27. Changes in intercept due to the band offset changes between different insulator-semiconductor interface can also

be observed.

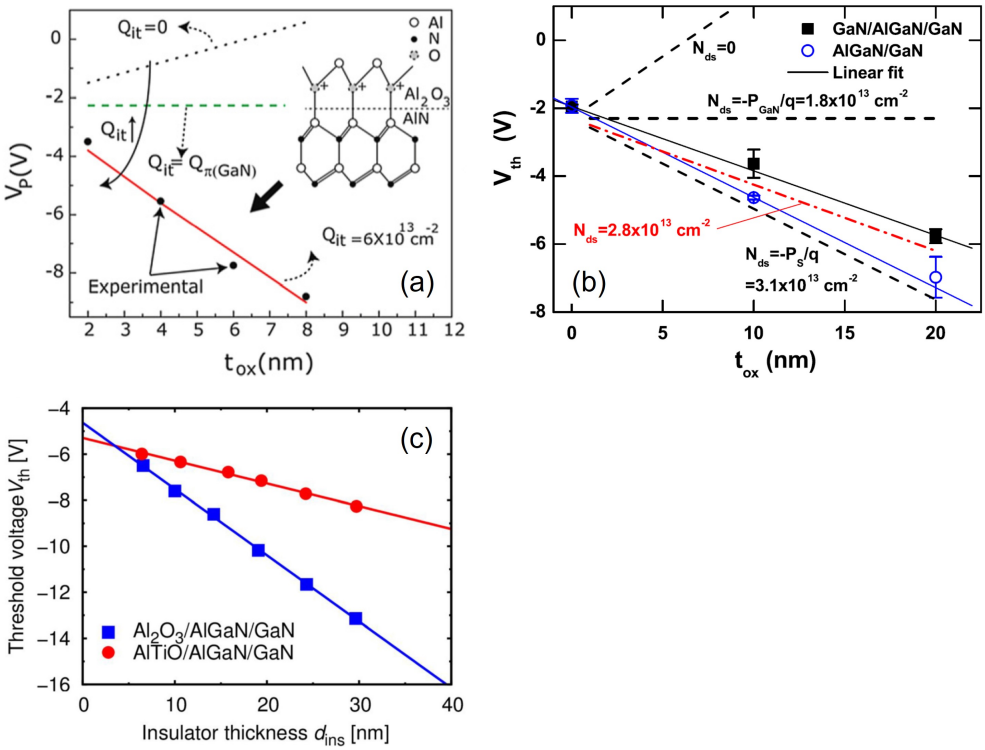

Figure 1.25: Negative threshold voltage shifts in (a) Al_2O_3/AlN/GaN [63], (b) Al_2O_3/AlGaN/GaN, Al_2O_3/GaN/AlGaN/GaN [68], and (c) Al_2O_3/AlGaN/GaN, AlTiO/AlGaN/GaN devices [48].

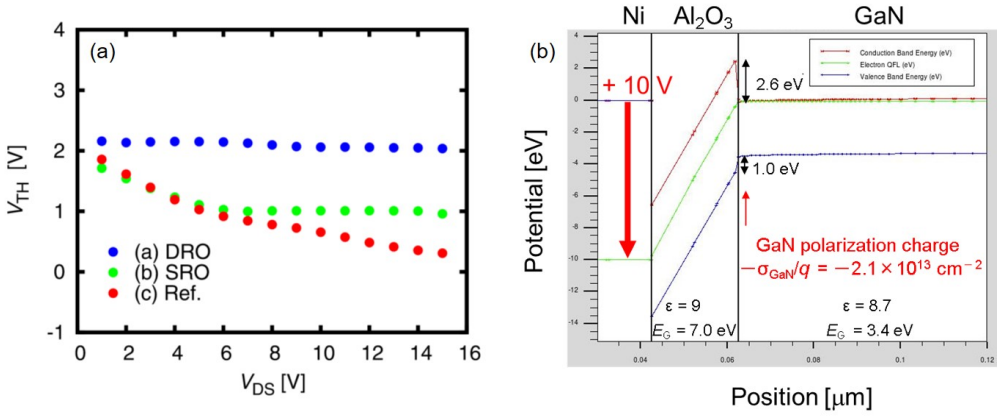

Figure 1.26: (a) Threshold voltages of fully-gate-recessed Al_2O_3/GaN MIS-FETs. (b) Theoretical band diagram of the MIS-FETs, showing a theoretical V_{th} of 10 V [73].

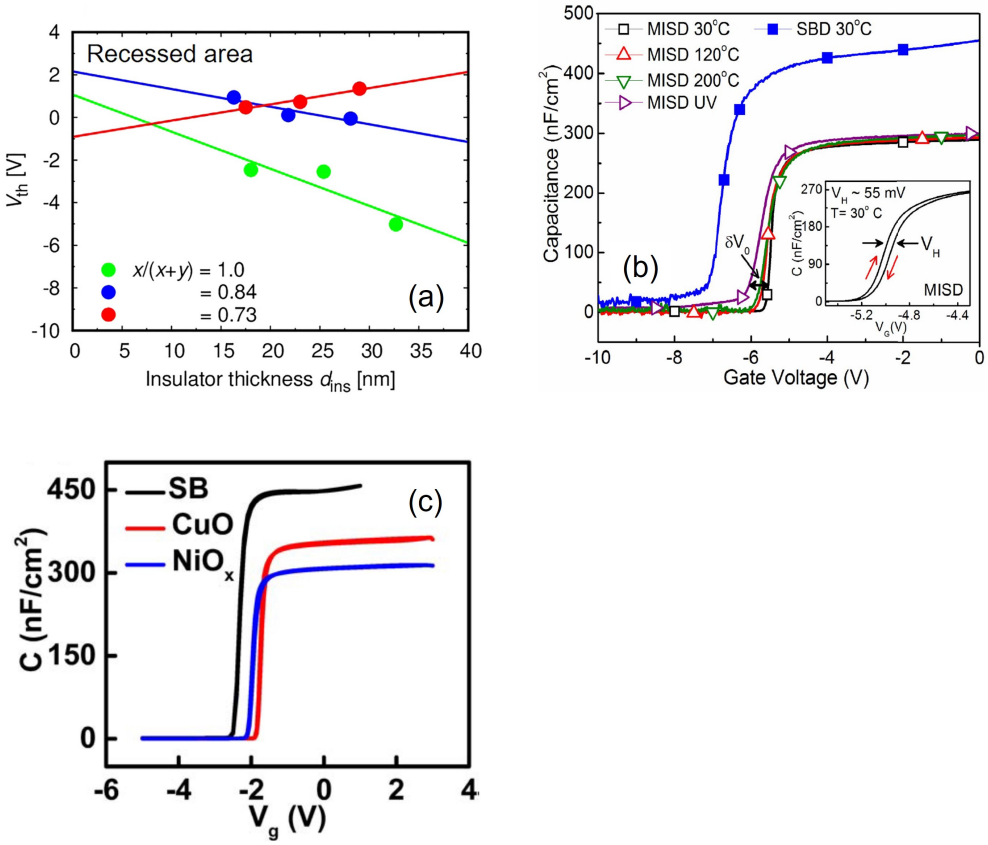

Figure 1.27: Positive threshold voltage shifts in (a) AlTiO/AlGaN/GaN [51], (b) Al_2O_3/AlInN/GaN [71], and (c) CuO/AlGaN/GaN, NiO_x/AlGaN/GaN devices [72].

The behaviors of φ and σ_{int} also can be attributed to the existence of an unintentional insulator-semiconductor interfacial layer with a dipole, where the band offset is modulated by ΔE_{vac} due to the dipole, and the fixed charge density of the metal/interfacial layer/AlGaN interface can be interpreted as a dipole unbalance. In order to control the interface of the AlGaN/GaN devices, an insertion of an intentional metal-AlGaN or insulator-AlGaN interfacial layer should be effective as shown in Fig. 1.28.

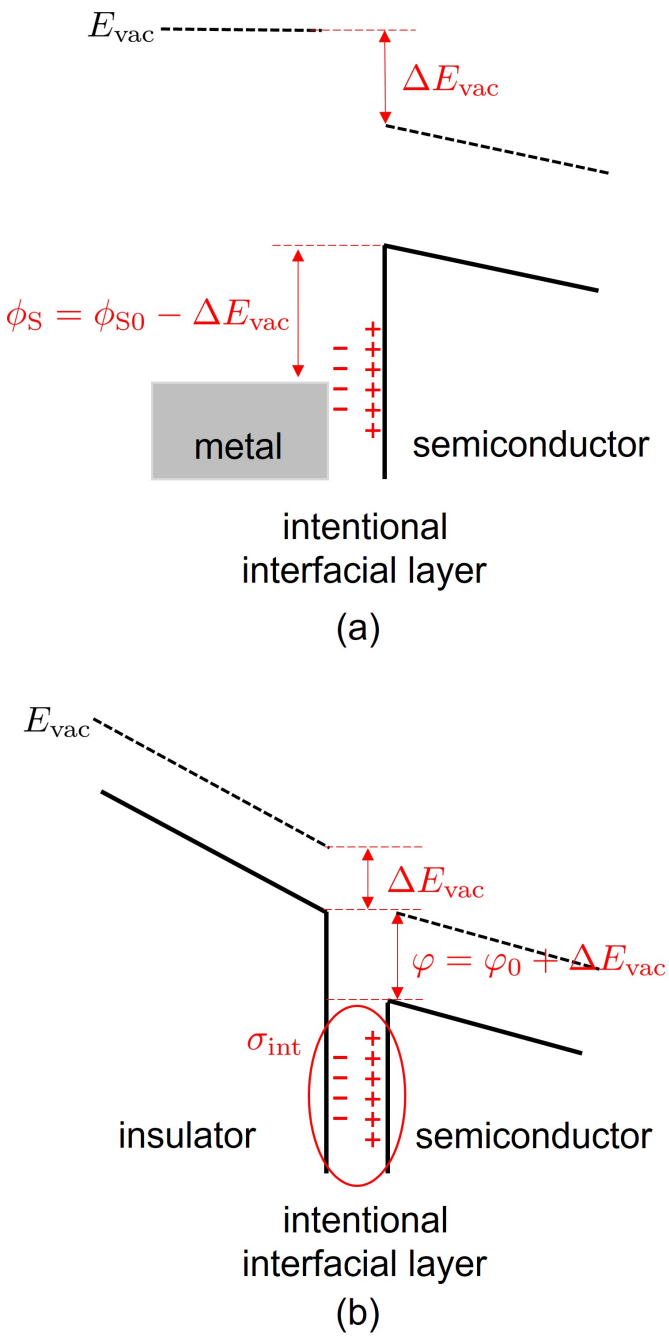

Figure 1.28: (a) The metal-semiconductor and (b) the insulator-semiconductor interface with an intentional interfacial layer.

Previously, intentional metal-(Al)GaN interfacial layers have been studied [74, 75]. An example is shown in Fig. 1.29, where an insertion of insulator interfacial layer modulate the barrier height effectively.

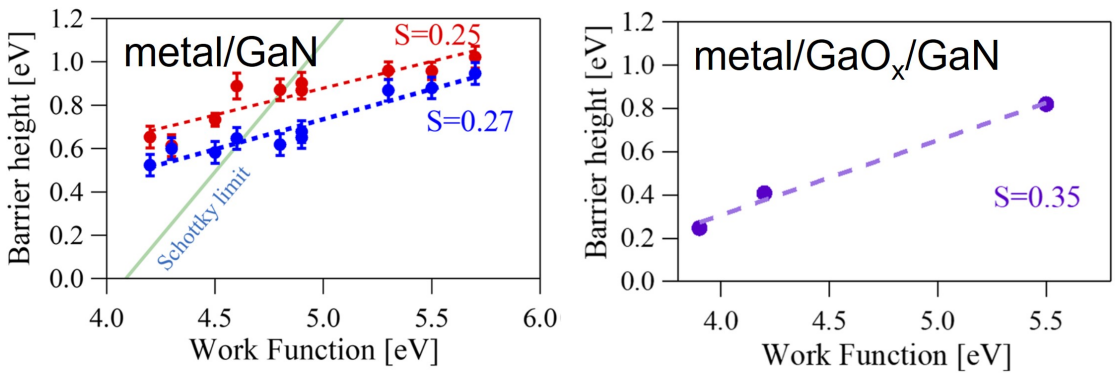

Figure 1.29: Barrier height modulation due to the insertion of a GaO_x interfacial layer.

On the other hand, MIS device performance improvements by an intentional insulator-(Al)GaN interfacial layer have been reported [76–78], where an example is shown in Fig. 1.30. However, the effects of a insulator-(Al)GaN interfacial layer on the fixed charge and band offset have not been elucidated, and systematic comparison between the effects of a metal-(Al)GaN interfacial layer and that of a insulator-(Al)GaN interfacial layer have been lacking.

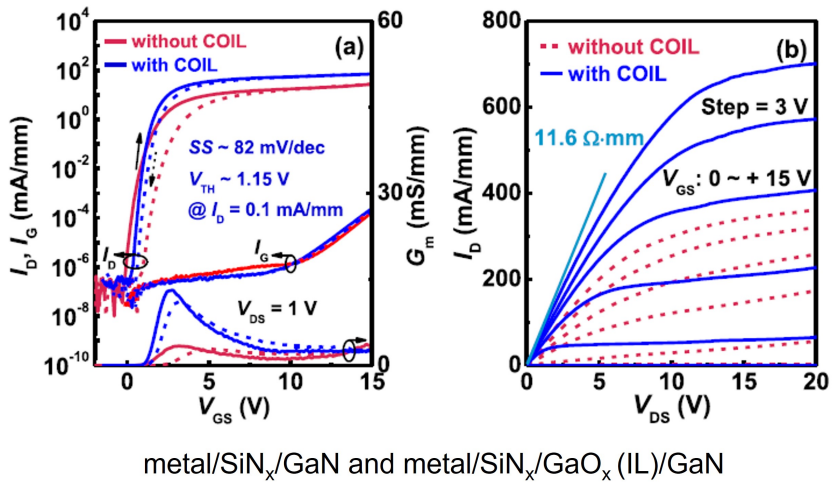

Figure 1.30: Performance improvements in MIS FETs due to the insertion of a GaO_x interfacial layer [78].

1.5 Purpose of this study

Effects of metal-semiconductor or insulator-semiconductor interfacial layers (ILs) in AlGaN/GaN devices were systematically investigated, where AlO_x, TiO_x, or NiO_x obtained by metal layer oxidation are employed as an IL. From this study, useful insights into the controls of threshold voltage for GaN-based devices are expected.

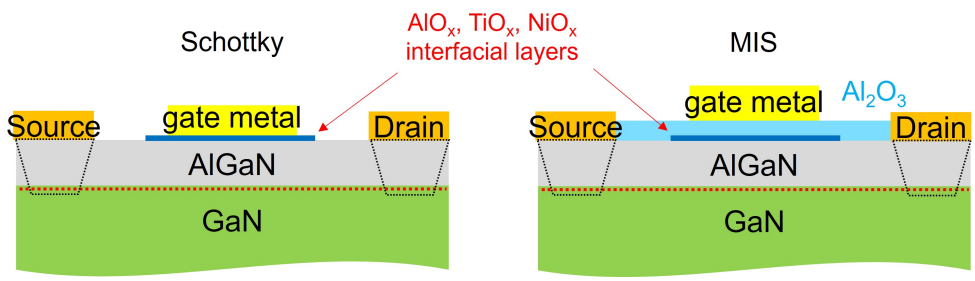

Figure 1.31: Schematic of AlGaN/GaN Schottky and MIS devices utilizing intentional interfacial layers (ILs).

1.6 Organization of the dissertation

This dissertation includes four chapters. The content of each chapter is summarized as follows.

Chapter 1 is the introduction to this research, which introduces the general background on compound semiconductors, the GaN-based semiconductors and related devices, the interfaces in AlGan/GaN devices, and the purpose of this study.

Chapter 2 is the investigation on the effects of metal-semiconductor interfacial layers (ILs) in metal/IL/AlGaN/GaN devices. We fabricated metal/IL/AlGaN/GaN devices and obtained their capacitance-voltage (C-V) characteristics, from which we found a modulation in the threshold voltage V_{th} due to the vacuum level step ΔE_{vac} induced by the dipole of the metal-AlGaN IL. From the vacuum level steps, the IL dipole density is estimated for each IL material. Moreover, using Hall measurements for the metal/IL/AlGaN/GaN devices, it is shown that we found that the 2DEG carrier concentration is also modulated by ΔE_{vac}.

Chapter 3 is the investigation on the effects of insulator-semiconductor interfacial layers (ILs) in metal/Al_2O_3/IL/AlGaN/GaN devices. We fabricated metal/Al_2O_3/IL/AlGaN/GaN devices and obtained their C-V characteristics. From the Al_2O_3 thickness dependence of V_{th}, we found the fixed charge density of the Al_2O_3/IL/AlGaN interface showing a positive correlation with the IL dipole density. Furthermore, we characterized the interface trap density in the metal/Al_2O_3/IL/AlGaN/GaN devices using the conductance method.

Chapter 4 concludes this work and discusses the future perspectives of the work.

Chapter 2

Effects of metal-semiconductor interfacial layers (ILs) in metal/IL/AlGaN/GaN devices

Effects of metal-semiconductor interfacial layers (ILs) in metal/IL/AlGaN/GaN devices were investigated, where AlO_x, TiO_x, or NiO_x obtained by metal layer oxidation are employed as an IL. We fabricated the metal/IL/AlGaN/GaN devices and obtained their capacitance-voltage (C-V) characteristics, from which we found a modulation in the threshold voltage V_{th} due to the vacuum level step ΔE_{vac} induced by the dipole of the metal-AlGaN IL. From the vacuum level steps, the IL dipole density is estimated for each IL material. Using Hall measurements for the metal/IL/AlGaN/GaN devices, it is shown that we found that the 2DEG carrier concentration is also modulated by ΔE_{vac}. By X-ray photoelectron spectroscopy (XPS), we investigated the chemical shifts in the IL/AlGaN interface, where formation of NiGa is suggested in NiO_x/AlGaN interface.

2.1 Metal/IL/AlGaN/GaN device fabrication

Using an $Al_{0.24}Ga_{0.76}N$ (20 nm)/GaN (3 μm) heterostructure grown by metal-organic vapor phase epitaxy on a sapphire (0001) substrate, we fabricated the metal/IL/AlGaN/GaN devices. The heterostructure schematic and basic electrical properties are shown in Fig. 2.1.

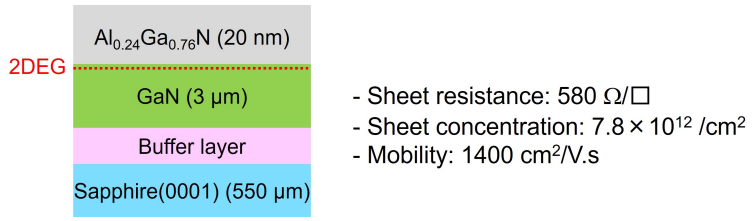

Figure 2.1: The AlGaN/GaN heterostructure schematic and basic electrical properties.

The fabrication main flow is shown in Fig. 2.2, consisting of Ohmic electrode formation, IL metal deposition, IL oxidation and gate electrode formation. After Ti-based Ohmic electrode formation, thin Al, Ti or Ni metal layers with several thicknesses in the nm-range were deposited on AlGaN. Annealing at 350 °C in air was carried out next, to obtain thin oxide ILs of AlO_x, TiO_x, or NiO_x. The fabrication was completed by formation of Ni gate metal covered by Au. Metal/AlGaN/GaN devices with no IL were also fabricated for comparison.

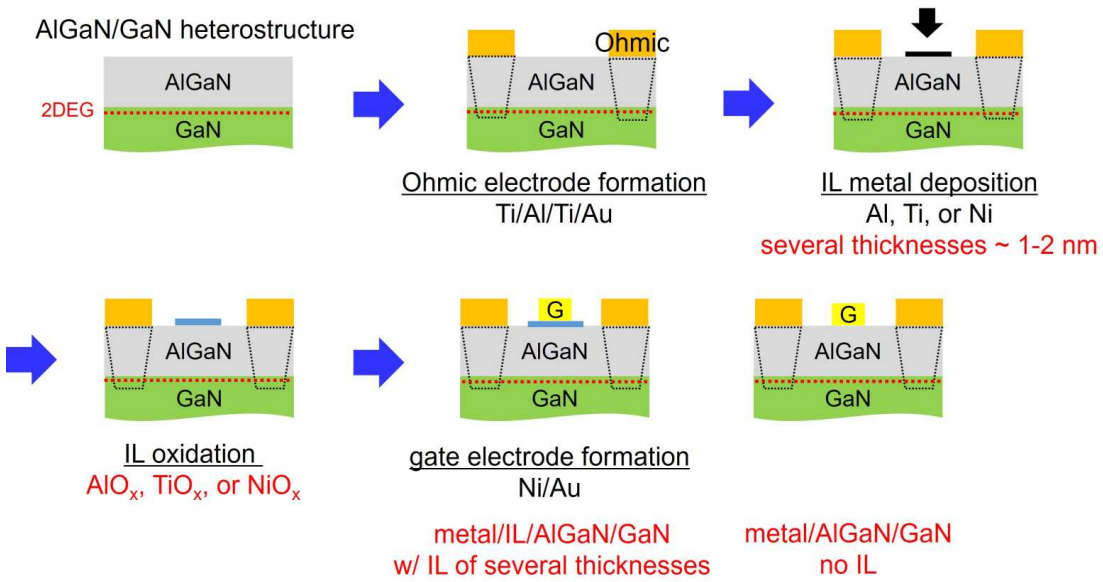

Figure 2.2: Metal/IL/AlGaN/GaN device fabrication main flow.

Ohmic electrode formation

The process flow of the Ohmic electrode formation is shown in Fig. 2.3 with detailed conditions. This process includes 4 parts, surface treatment, patterning, Metal deposition and annealing.

Surface treatment was carried out by using organic solutions such as acetone, methanol, and deionized water (DIW), followed by O_2 plasma ashing to fully remove organic impurities on the sample surface. After that, the samples were put in a semico-clean solution, a dilute solution of tetra-methyl ammonium hydroxide (TMAH) and $N(CH_3)_4OH$ to remove oxide layer at the surface, then washed in DIW.

Patterning by lithographic was carried out next, consisting of resist coating, exposure, and developing. Before resist coating, the samples were baked to remove remaining water. Lift-off resist LOL2000 and positive resist TSMR-8900 were coated using spincoater, followed by baking for resist hardening. Exposure for the coated samples was carried out by mask-less aligner (MLA) using laser light of wavelength 405 nm. Then the development was done by TMAH, followed by washing in DIW, and O_2 plasma ashing to remove remaining resist. Patterning was finished by a semico-clean solution treatment to remove oxide layer, which was formed after long time exposure in the air.

Metal deposition was then carried out by resistance heating evaporator (RHE). After vacuuming until the pressure reached the low of 10^{-4} Pa, Ti/Al/Ti/Au metals were deposited with the thickness of 5/100/200/50 nm. After the deposition, lift-off process was carried out by a resist remover, 1-methyl-2-pyrrolidinone-based solution (commercial name: 1165), follow by necessary wet surface treatment.

Finally, annealing in N_2 atmosphere at 575 °C formed the Ohmic contact between metal and semiconductor.

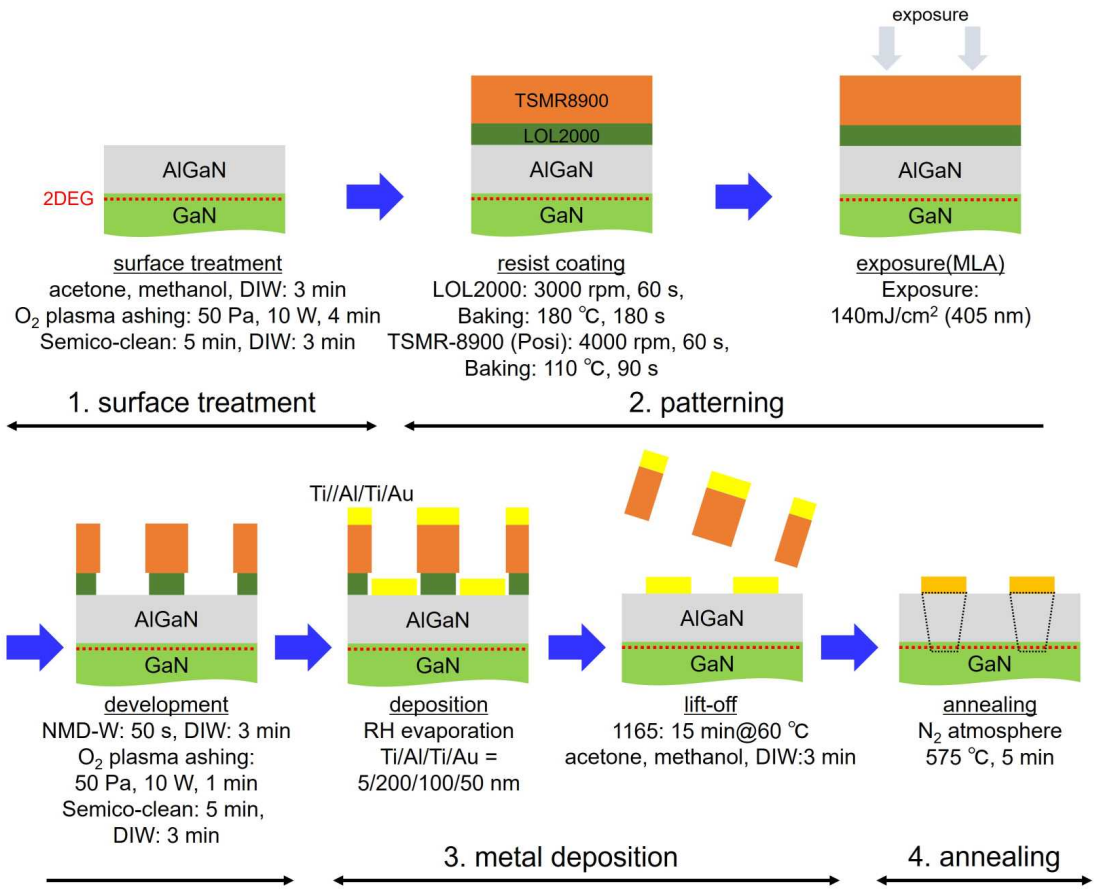

Figure 2.3: Process flow of the Ohmic electrode formation.

IL metal deposition

The process flow of the IL metal deposition is shown in Fig. 2.4 with detailed conditions. This process includes 3 parts, surface treatment, patterning, and metal deposition. Metal deposition was carried out by RHE, where Al. Ti or Ni thin metal layers were deposited with several thicknesses of $\sim$ nm.

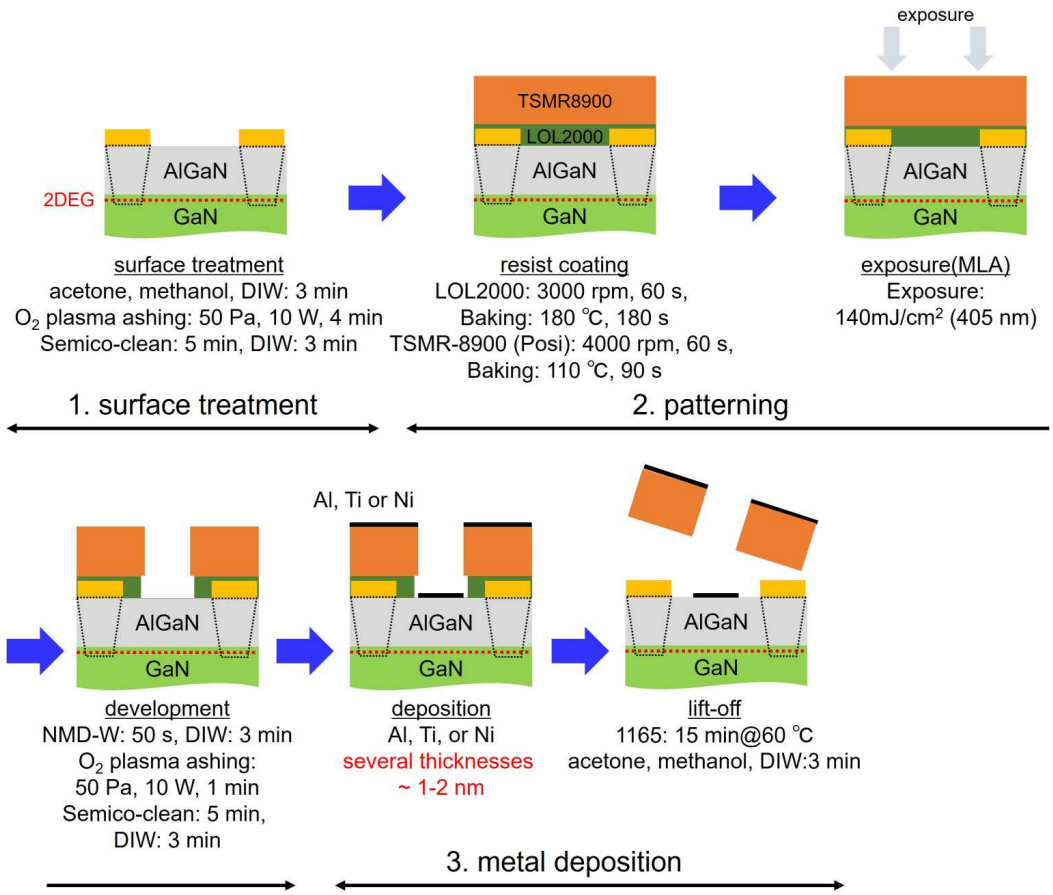

Figure 2.4: Process flow of the IL metal deposition.

IL oxidation

The process flow of the IL oxidation is shown in Fig. 2.5 with detailed conditions. This process includes 2 parts, surface treatment and annealing. The annealing was carried out in air atmosphere at 350 °C, forming the thin metal oxide AlO_x, TiO_x, or NiO_x ILs. The determination of conditions for oxidation annealing will be explained in the next section.

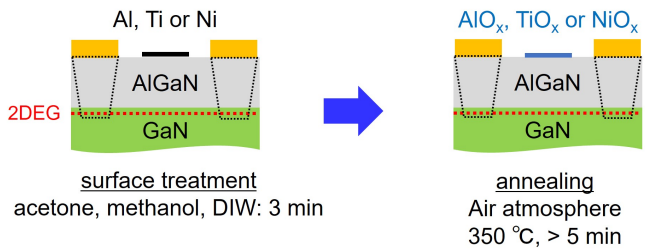

Figure 2.5: Process flow of the IL oxidation.

Gate electrode formation

The process flow of the gate electrode formation is shown in Fig. 2.6 with detailed conditions. This process includes 3 parts, surface treatment, patterning, and metal deposition. Since TMAH is capable to dissolve oxide ILs, semico-clean treatment was omitted. For the resist coating, addition layer is necessary to protect oxide ILs from development process due to the same reason. Thus, we employed an electron beam resist GL2000, which cannot be dissolved by TMAH but removed by O_2 plasma ashing. Metal deposition was carried out by RHE, where Ni/Au metal was deposited with the thicknesses of 5/100 nm. The gate electrode formation finished the fabrication of metal/IL/AlGaN/GaN devices.

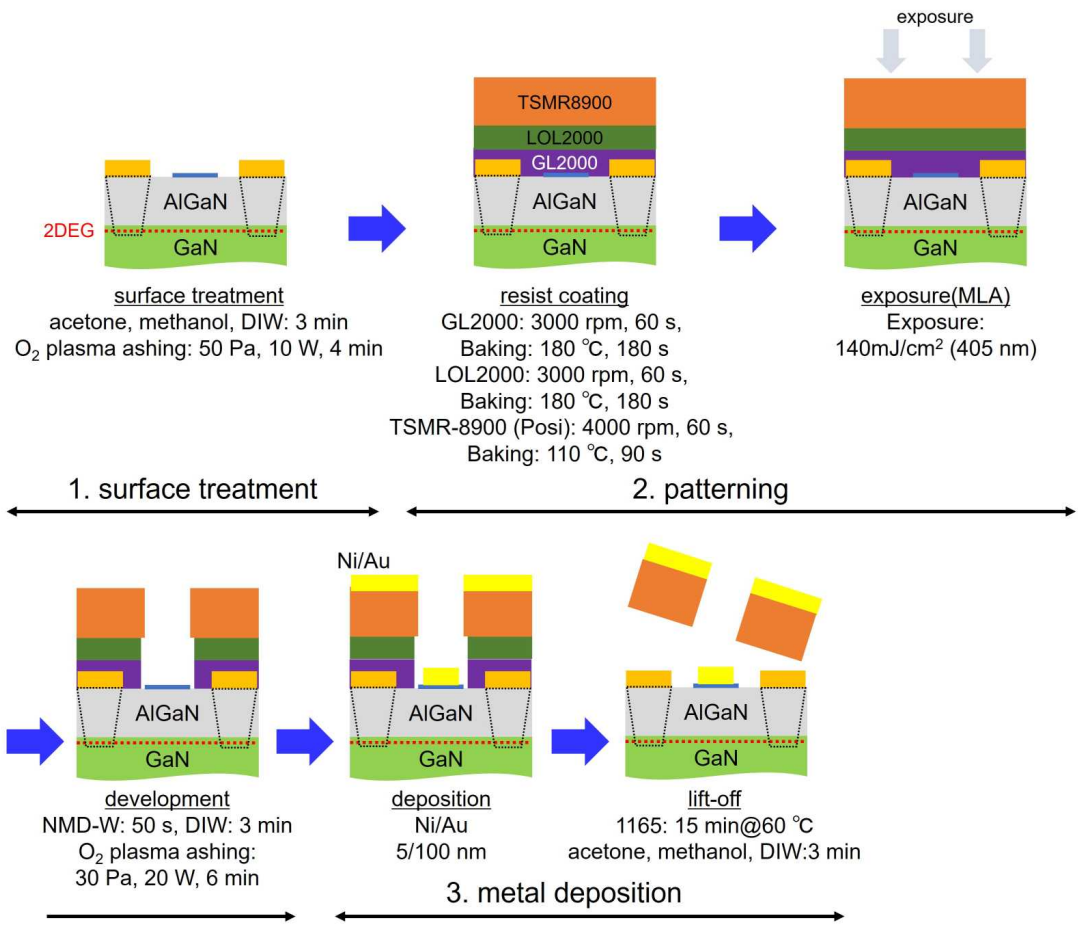

Figure 2.6: Process flow of the gate electrode formation.

2.2 Details in the IL formation

Determination of oxidation conditions

Figure 2.7 shows the schematic of Hall devices for bear AlGaN/GaN structures, and the 2DEG carrier concentrations n_{s0} obtained form them at $V_G = 0$ as a function of the anneal temperature. A serious decrease in n_{s0} is observed for anneal temperature > 350 °C, suggesting an oxidation on the AlGaN surface which should be avoided. Therefore, anneal temperature for IL oxidation is determined to be 350 °C.

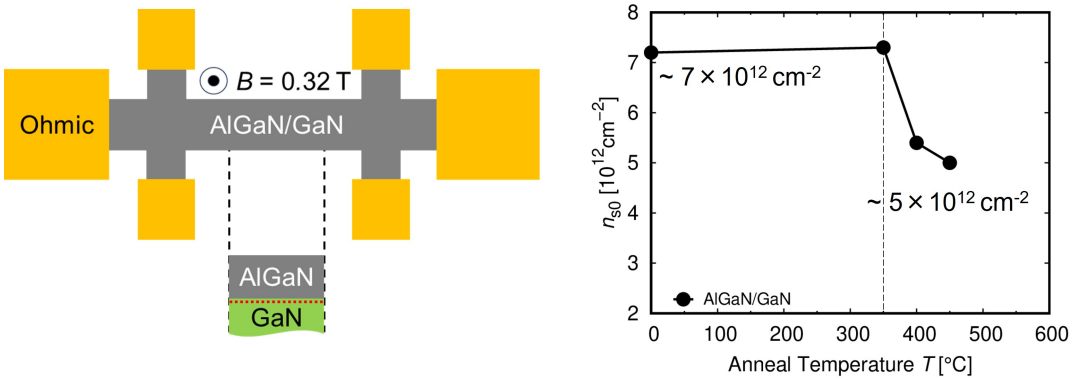

Figure 2.7: Schematic of Hall devices for AlGaN/GaN and the 2DEG carrier concentrations n_{s0} at $V_G = 0$ obtained form them as a function of anneal temperature.

Figure 2.7 shows the schematic of Hall devices for IL/AlGaN/GaN structures, and the 2DEG carrier concentrations n_{s0} obtained form them at $V_G = 0$ as functions of anneal time, in comparison with a AlGaN/GaN structure with no IL. Decreases in n_{s0} are observed right after the IL metal deposition (anneal time = 0) due to possible surface barrier height changes. More importantly, after a 5 minutes anneal, we find further n_{s0} decreases in IL/AlGaN/GaN, indicating the progress of interface reactions between the ILs and AlGaN. n_{s0} remain almost constants for further annealing, indicating a complete reaction in IL/AlGaN interfaces, and a complete oxidation of ILs. Therefore, we determined a over 5 minutes anneal time for the IL oxidation.

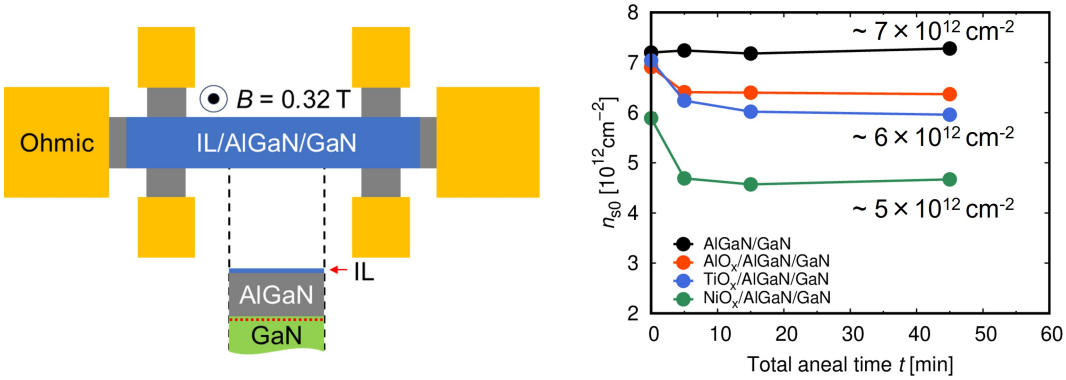

Figure 2.8: Schematic of Hall devices for IL/AlGaN/GaN and the 2DEG carrier concentrations n_{s0} at $V_G = 0$ obtained form them as a function of the anneal time. Anneal temperature is fixed at 350 °C.

Surface morphology of the ILs

Figure 2.9 shows examples of atomic force microscope (AFM) images for the surfaces of the AlO_x, TiO_x, and NiO_x ILs in comparison with the AlGaN surface, indicating that the surface morphology is unchanged after the IL formation. On the other hand, due to the ∼ nm surface roughness, it is difficult to accurately evaluate the thicknesses for ILs of same order. Therefore, the IL thicknesses are confirmed by the capacitance of the ILs shown later.

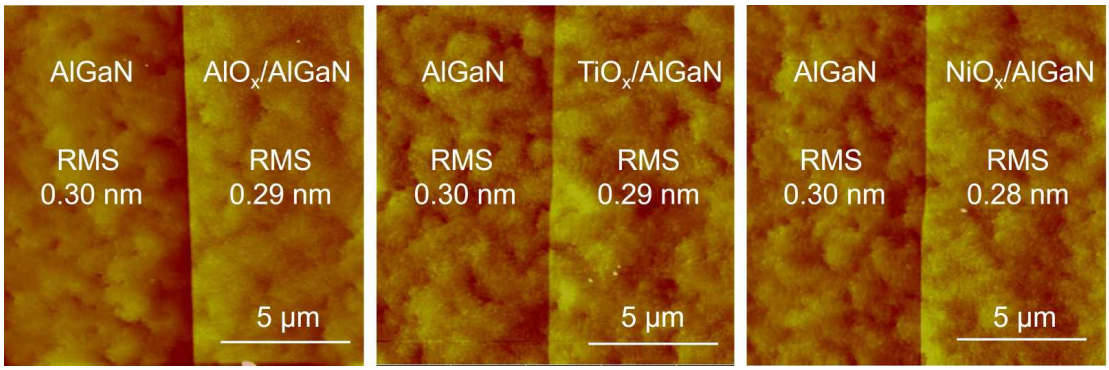

Figure 2.9: Atomic force microscope (AFM) images of the surfaces of AlGaN, AlO_x, TiO_x, and NiO_x.

2.3 Metal/IL/AlGaN/GaN devices characterization

Current-frequency (J-V) characterizations

Figure 3.5 shows the top view of a fabricated capacitor and the configuration of J-V (DC) characterization for the capacitors, using semiconductor parameter analyzer.

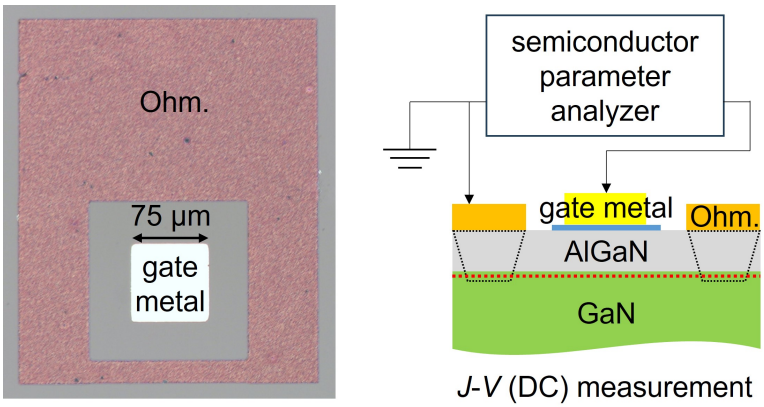

Figure 2.10: Top view of a fabricated capacitor and the configuration of J-V (DC) characterization.

Figure 2.11 shows examples of current-voltage (J-V) characteristics of the capacitors, where one device is picked up for each IL, under application of the gate voltage V_G with respect to the grounded Ohmic electrode. The IL leads to lower leakage, which can be attributed to both the vacuum level steps ΔE_{vac} (equivalently the effective barrier height ϕ_S) and the IL barrier effects. Thus, it is difficult to accurately evaluate ΔE_{vac} (or ϕ_S) from the J-V characteristics.

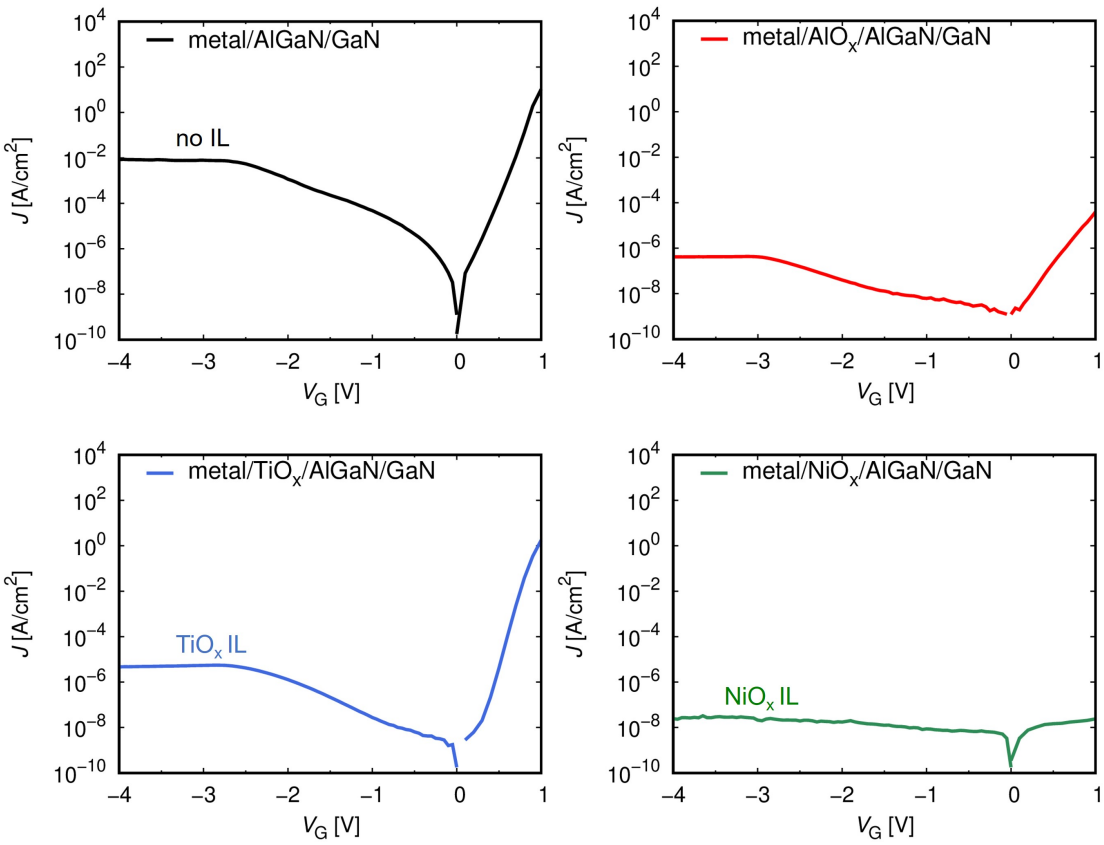

Figure 2.11: J-V characteristics of metal/AlGaN/GaN and metal/IL/AlGaN/GaN devices.

On the other hand, ΔE_{vac} can be evaluated from the capacitance-voltage (C-V) characteristics.

Capacitance-voltage (C-V) characterizations

Figure 2.12 shows the band diagram of a metal/IL/AlGaN/GaN device, where ϕ_{S0} is the barrier height with no vacuum level step, ϕ_{S} is the effective barrier height, ΔE_{c} is the AlGaN-GaN conduction band offset, $\sigma_{\text{GaN}}/q \simeq 2.1 \times 10^{13}$ cm^{-2} and $\sigma_{\text{AlGaN}}/q \simeq 3.2 \times 10^{13}$ cm^{-2} give the polarization charge densities [79–83], and σ_{D} is the IL dipole density. From this band diagram, we obtain the vacuum level step

$$\Delta E_{\text{vac}} = \frac{q(\sigma_{\text{D}} - \sigma_{\text{GaN}})}{C_{\text{IL}}} \tag{2.1}$$

and the threshold voltage

$$V_{\mathrm{th}} = \frac{\phi_{\mathrm{S0}}}{q} - \frac{\Delta E_{\mathrm{vac}}}{q} - \frac{\sigma_{\mathrm{AlGaN}} - \sigma_{\mathrm{GaN}}}{C_{\mathrm{AlGaN}}} - \frac{\Delta E_{\mathrm{C}}}{q} \tag{2.2}$$

using the IL capacitance C_{IL} and the AlGaN capacitance C_{AlGaN}[1]. Since the threshold voltage with no IL is given by

$$V_{\mathrm{th0}} = \frac{\phi_{\mathrm{S0}}}{q} - \frac{\sigma_{\mathrm{AlGaN}} - \sigma_{\mathrm{GaN}}}{C_{\mathrm{AlGaN}}} - \frac{\Delta E_{\mathrm{C}}}{q} \tag{2.3}$$

assuming $\Delta E_{\mathrm{vac}} = 0$, we obtain the threshold voltage shift

$$V_{\mathrm{th}} - V_{\mathrm{th0}} = -\frac{\Delta E_{\mathrm{vac}}}{q}, \tag{2.4}$$

which can be used to evaluate ΔE_{vac}.

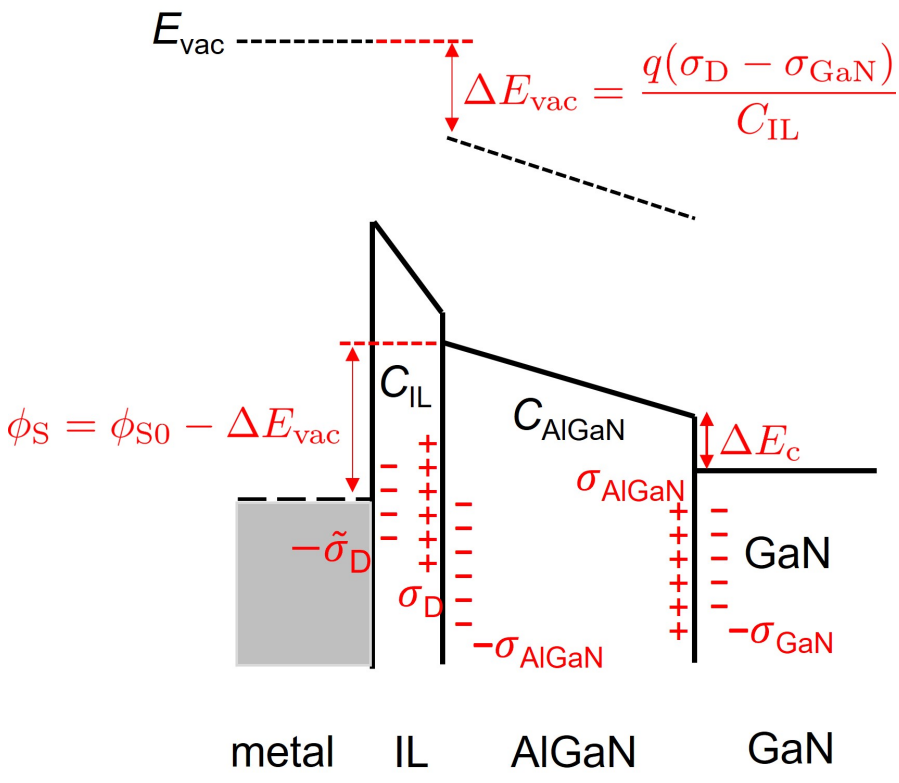

Figure 2.12: The band diagram of the metal/IL/AlGaN/GaN devices.

Figure 3.7 shows the configuration of the C-V (AC) characterization for the capacitors, using LCR meter.

[1]see Appendix A for detailed derivation

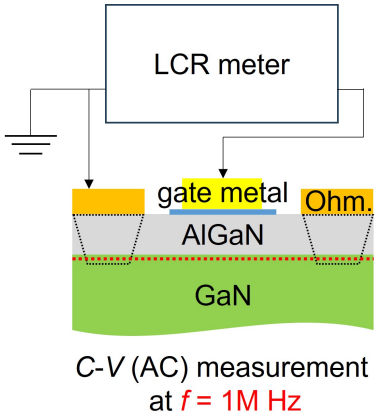

Figure 2.13: The configuration of C-V (AC) characterization at $f = 1$ MHz.

Figure 2.14 shows examples of C-V characteristics at frequency $f = 1$ MHz, where one device is picked up for each IL. The 2DEG concentration n_s obtained by integrating the C-V characteristics is also shown in Fig. 2.14, and can be fitted by $qn_s \simeq C_{tot}(V_G - V_{th})$ using the total capacitance C_{tot} given by $1/C_{tot} = 1/C_{AlGaN} + 1/C_{IL}$. From the fitting, V_{th}, V_{th0}, C_{AlGaN}, and C_{IL} are obtained. For the AlO_x, TiO_x, and NiO_x ILs with several thicknesses, we find $1/C_{IL} \lesssim 0.4$ cm$^2/\mu$F, $\lesssim 0.1$ cm$^2/\mu$F, and $\lesssim 0.4$ cm$^2/\mu$F, corresponding to the IL thicknesses of $\lesssim 3$ nm, $\lesssim 3$ nm, and $\lesssim 4$ nm, respectively, assuming typical dielectric constants ~ 7 of AlO_x, ~ 30 of TiO_x, and ~ 10 of NiO_x.

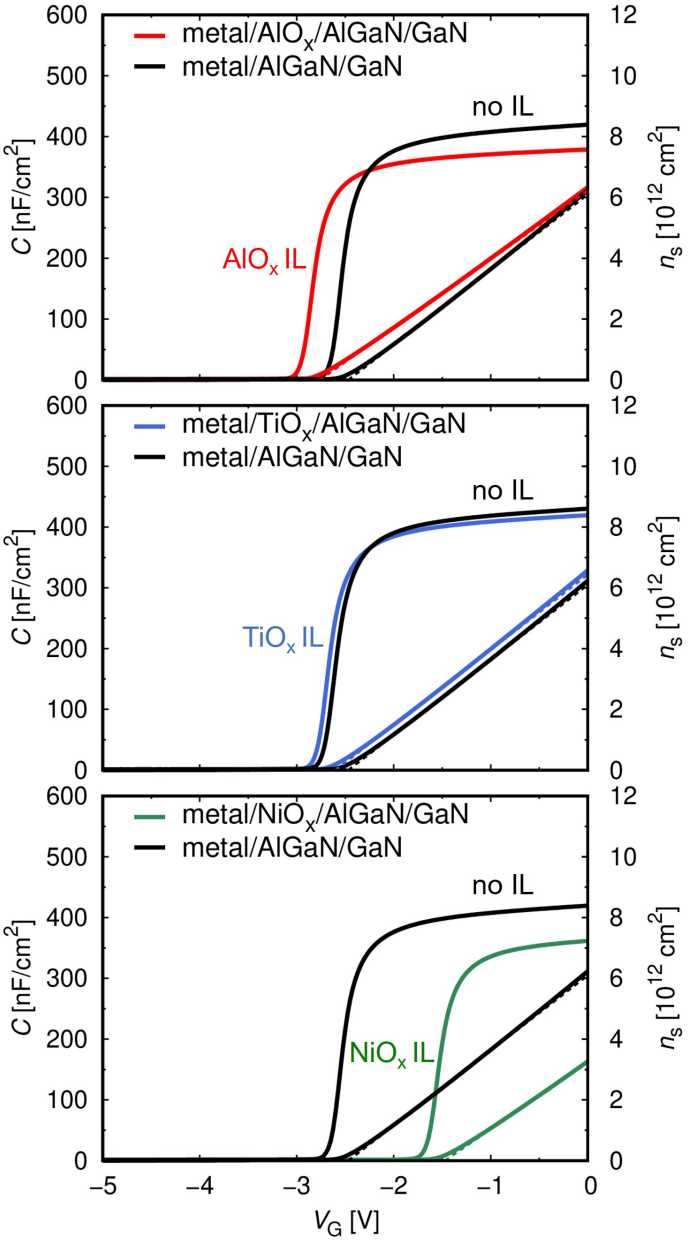

Figure 2.14: C-V and n_s-V characteristics of metal/AlGaN/GaN and metal/IL/AlGaN/GaN devices.

The obtained $V_{th} - V_{th0}$ and ΔE_{vac} of all the devices are shown in Fig. 2.15 as functions of $1/C_{IL}$, where $V_{th} - V_{th0}$ and $-\Delta E_{vac}$ are shown in the left and right vertical axes, respectively. It is shown that $V_{th} - V_{th0} < 0$ for the AlO_x and TiO_x ILs, indicating that the vacuum level step ΔE_{vac} is positive, while for the

NiO_x ILs, $V_{th} - V_{th0} > 0$ indicating that the vacuum level step ΔE_{vac} is negative. Moreover, we find an almost proportional relation between ΔE_{vac} and $1/C_{IL}$ for each IL, indicating that the IL dipole density

$$\sigma_D = \frac{\Delta E_{vac} C_{IL}}{q} + \sigma_{GaN} \tag{2.5}$$

is almost constant for each IL material. Figure 2.16 shows the averaged IL dipole densities in comparison with σ_{AlGaN}, $\sigma_D/q \simeq 2.5 \times 10^{13}$ cm^{-2} of the AlO_x ILs, $\sigma_D/q \simeq 3.5 \times 10^{13}$ cm^{-2} of the TiO_x ILs, and $\sigma_D/q \simeq 0.4 \times 10^{13}$ cm^{-2} of the NiO_x ILs, where the error bars stand for the three-sigma standard deviations. This indicates that the AlO_x/AlGaN and TiO_x/AlGaN interfaces are nearly neutral, while the NiO_x/AlGaN interface is quite negatively charged.

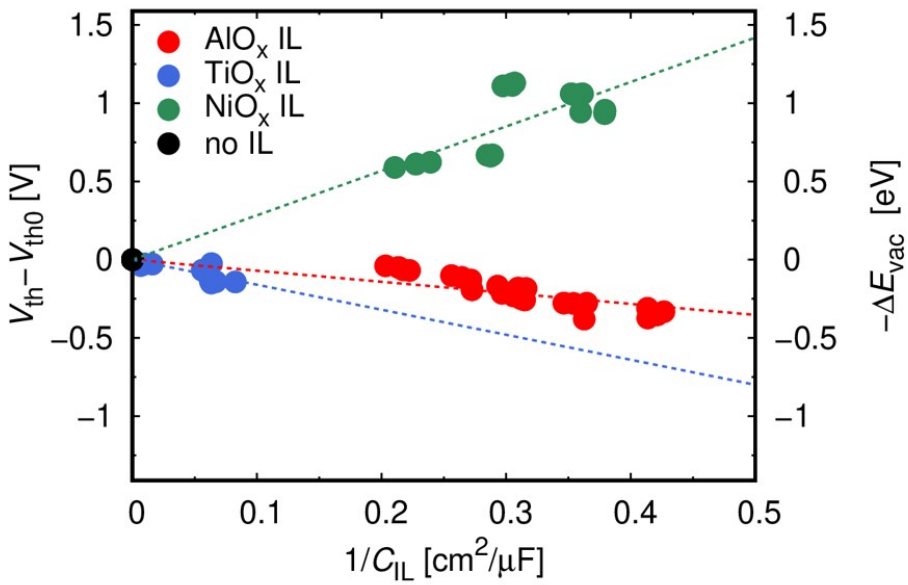

Figure 2.15: The threshold voltage shifts $V_{th} - V_{th0}$ and vacuum level steps ΔE_{vac} of all the devices as functions of $1/C_{IL}$.

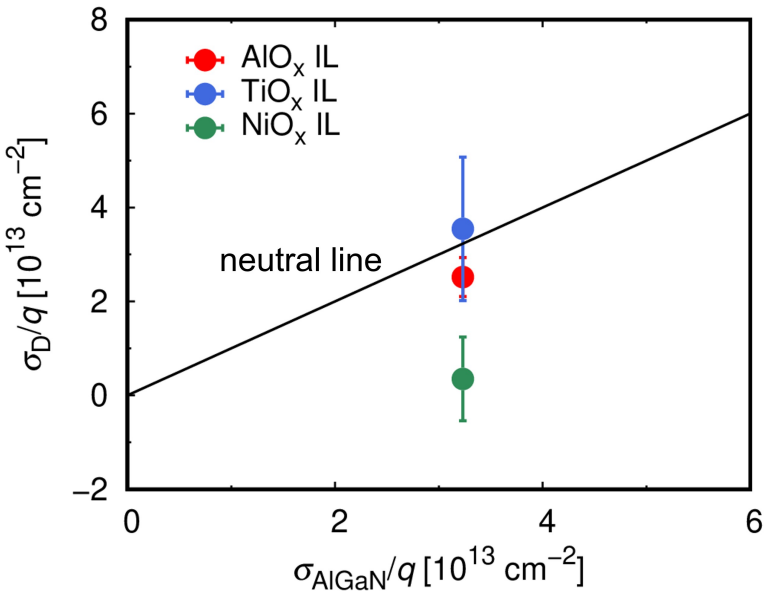

Figure 2.16: The interfacial layer (IL) dipole density σ_{D} in comparison with the AlGaN polarization charge density σ_{AlGaN}.

Based on these obtained results, Figure 2.17 shows the calculated 1D Poisson-Schrödinger band diagrams of the metal/AlGaN/GaN and metal/IL/AlGaN/GaN devices at $V_{\mathrm{G}} = 0$ V, where we assume a 2 nm IL thickness. The AlO$_x$ and TiO$_x$ ILs slightly lower the effective barrier height owing to the almost neutral AlO$_x$/AlGaN, TiO$_x$/AlGaN interfaces and the consequent positive ΔE_{vac}, while NiO$_x$ strongly increase it owing to the quite negatively charged NiO$_x$/AlGaN interface and the consequent negative ΔE_{vac}. Note that the change in effective barrier heights do not equal to the extracted ΔE_{vac} due to the existence of 2DEG.

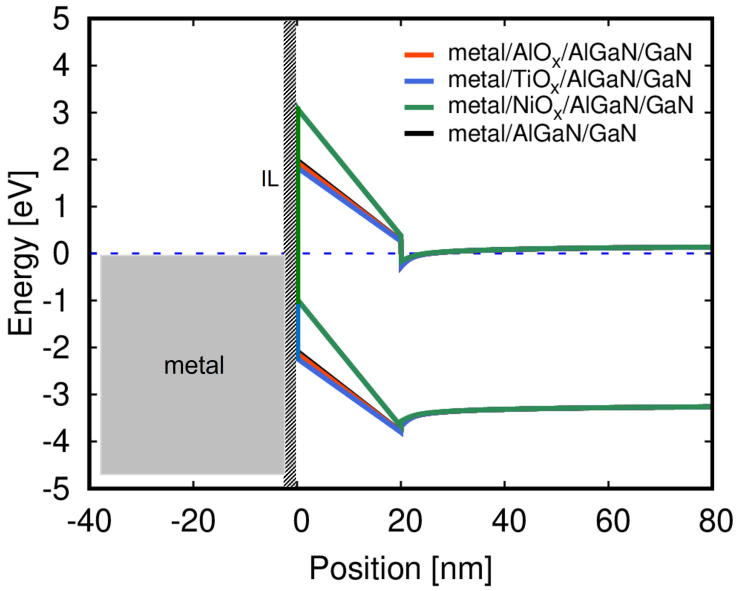

Figure 2.17: Calculated 1D Poisson-Schrödinger band diagrams of the metal/AlGaN/GaN and metal/IL/AlGaN/GaN devices.

Moreover, we fabricated metal/IL/AlGaN/GaN and metal/AlGaN/GaN Hall-bar devices shown in Fig. 2.18. From Hall measurements under a magnetic field $B = 0.32$ T, the 2DEG carrier concentration n_{s0} at $V_G = 0$ was obtained. The relation between qn_{s0}/C_{tot} and ΔE_{vac} is also shown in Fig. 2.18, being consistent with $qn_{s0}/C_{tot} = -V_{th} = \Delta E_{vac}/q + V_{th0}$ shown by the dashed line, indicating that n_{s0} is also modulated by the vacuum level step ΔE_{vac} due to the dipole. In particular, the NiO$_x$ ILs strongly reduce the 2DEG concentration.

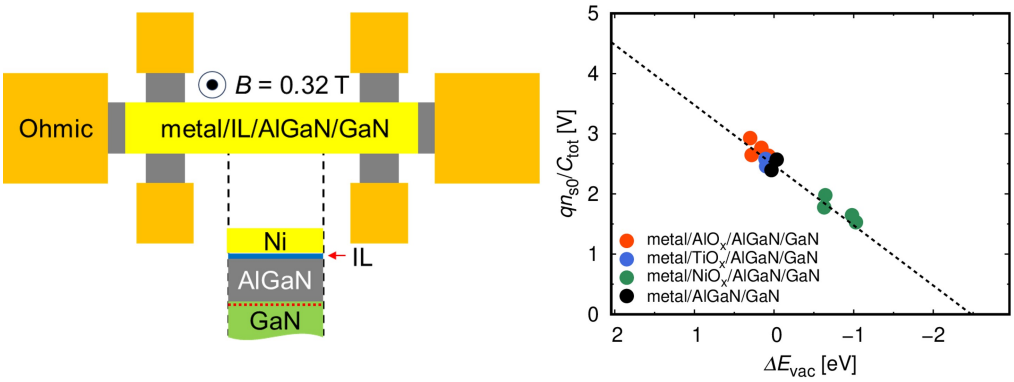

Figure 2.18: Schematic of Hall devices for metal/IL/AlGaN/GaN and the relation between n_{s0} and ΔE_{vac}. The dashed line shows $qn_{s0}/C_{tot} = -V_{th} = \Delta E_{vac}/q + V_{th0}$.

The fact that ΔE_{vac} is either positive or negative can be attributed to the reaction at the IL/AlGaN interface. The tie-line configurations for metal-(Al)Ga-N systems have been studied [84, 85], showing that TiN is stable in a Ti-(Al)Ga-N system, while NiGa is stable in a Ni-(Al)Ga-N system as shown in the Fig. 2.19. Considering that AlN is also stable in a Al-(Al)Ga-N system, due to the formation of TiN or AlN, nitrogen vacancy V_N donors can be generated at the TiO_x/AlGaN or AlO_x/AlGaN interface, and the ionized donors act as positive IL dipole charges leading to the positive ΔE_{vac}. On the other hand, due to the formation of NiGa, gallium vacancy V_{Ga} acceptors can be generated at the NiO_x/AlGaN interface, and the ionized acceptors act as negative IL dipole charges leading to the negative ΔE_{vac}.

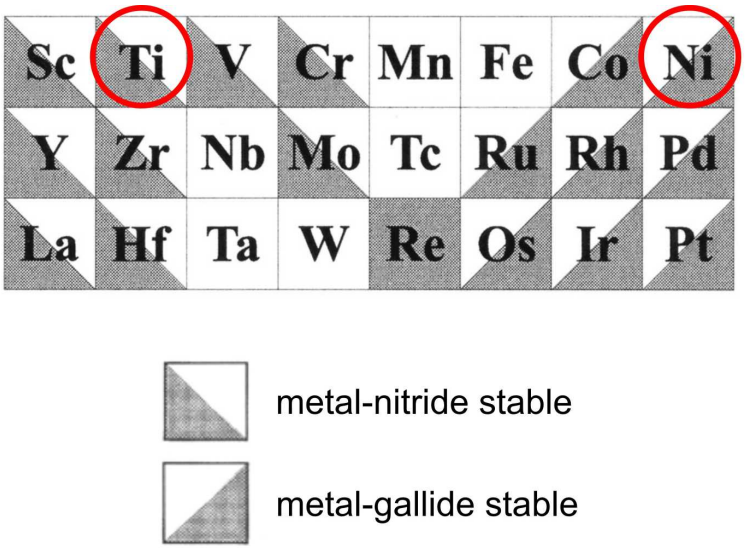

Figure 2.19: Tie-line configurations for metal-Ga-N systems[85].

2.4 X-ray photoelectron spectroscopy (XPS) for the IL/AlGaN interfaces

In order to examine the IL/AlGaN interface reaction, we employed X-ray photoelectron spectroscopy (XPS) to investigate the chemical shifts in the interfaces. Figure 2.20 shows the configuration of the XPS measurement using a photon energy $\simeq$ 1.5k eV and a take-off angle of 35°, leading to a inelastic mean free path of electron $\simeq$ 2 nm [86]. Bear AlGaN, metal/AlGaN (before oxidation), and IL/AlGaN (after oxidation) are investigated, where the thicknesses of metals and ILs were chosen to be $<$ 2 nm in order to study the interface.

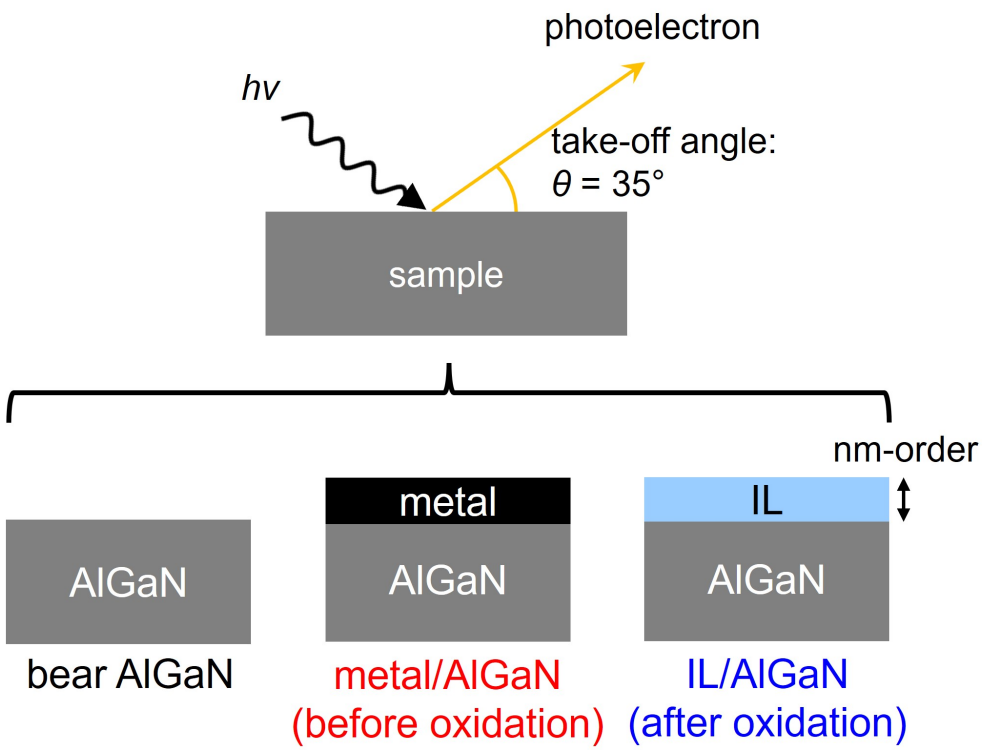

Figure 2.20: Configuration of the XPS measurement and schematics of samples.

Figure 2.21 shows the wide scan spectra for the bear AlGaN and the IL/AlGaN samples, from which we can identify the peak positions of each element.

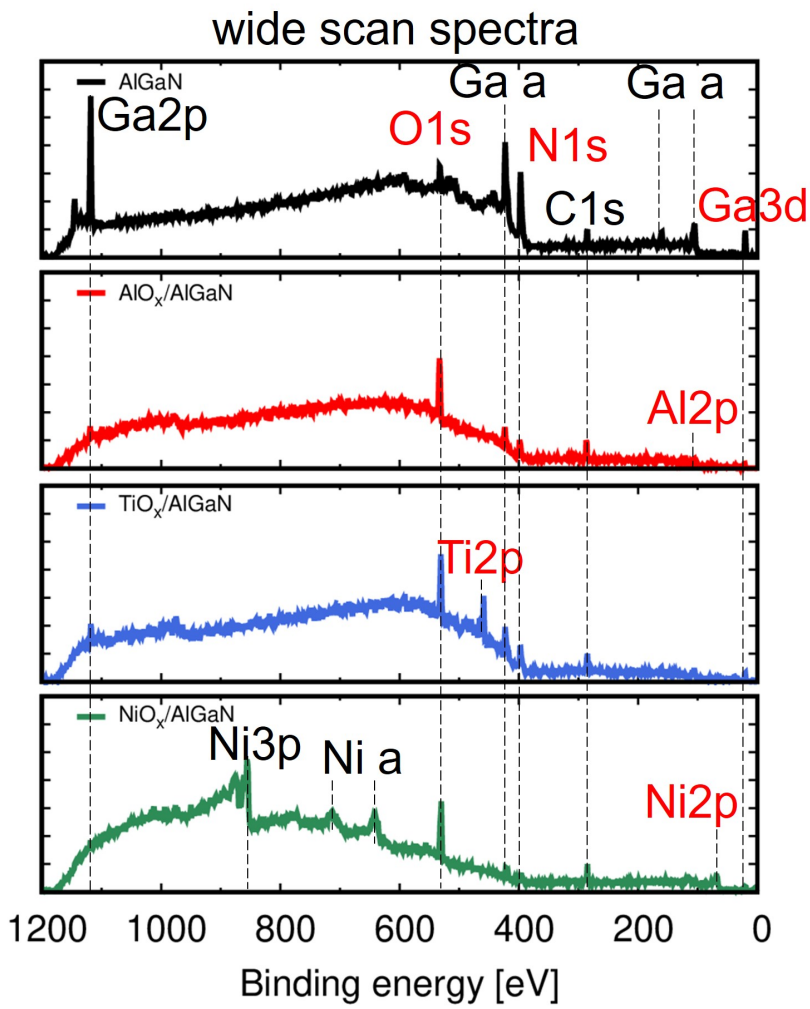

Figure 2.21: Wide scan spectra for the bear AlGaN and the IL/AlGaN.

Afterward, high resolution scan for each highlighted peak was carried out. Before each scan, calibrations to remove the extrinsic chemical shift (equivalently the binding energy peak position shift) due to the potential difference between samples and detector are done by using C-C binding energy from C1s spectra. Figure 2.22 shows the C1s spectra, illustrating different bonding states of carbon (C-C, C-OH, or C=O). The dots are measurement data and the red lines are the fitted curves given by the sum of individual Gaussian peaks for each bonding state. We adjusted the peak positions of C-C for every spectra to 284.8 eV, finishing the calibration of peak positions.

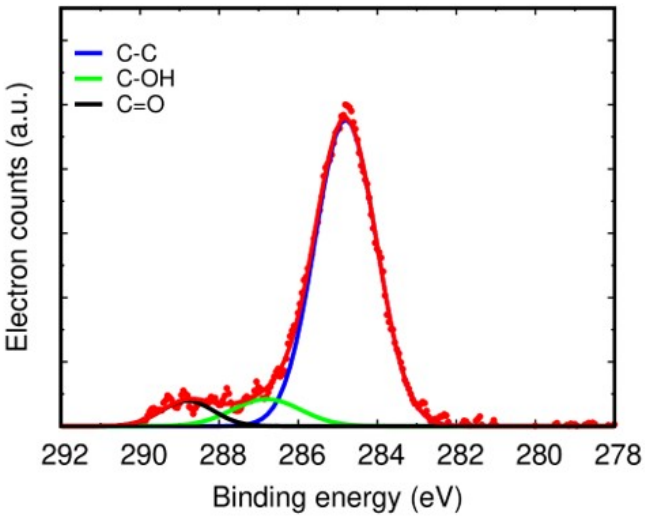

Figure 2.22: C1s spectra with Gaussian peaks fitting.

Figure 2.23 shows the O1s spectra for each samples. For AlO_x, negligible change was observed in the peak positions, while for TiO_x and NiO_x, the peaks shift to high energy side. The XPS binding energy of an element is a measure of the electronic environment (equivalently the bonding state) of that element. When an additional element is introduced, the electronegativity of the additional element determines the shift in binding energy peak position. Table 2.1 shows the electronegativity for the elements involved in the IL/AlGaN interfaces. When bonds with high electronegativity element such as O increase, the electron density around the base element decreases, leading to an increase in binding energy. On the contrary, when bonds with low electronegativity element such as a metal (Al, Ti or Ni) increase, electron density around the base element increases, leading to a decrease in binding energy. Therefore, the unchanged peak positions for AlO_x/AlGaN suggest that the Al metal was almost oxidized completely before the

Table 2.1: Electronegativity for the elements involved in the IL/AlGaN interface[87].

Elements	O	N	Ni	Ga	Al	Ti
Electronegativity	3.44	3.04	1.91	1.81	1.61	1.54

anneal oxidation, while the high energy shifts for TiO_x/AlGaN and NiO_x/AlGaN indicate further oxidation due to the metal deposition and the anneal oxidation. However, since oxygen atoms can exist in both the oxide ILs and the IL/AlGaN interfaces, the O1s spectra is not a strong indicator to the interface reaction.

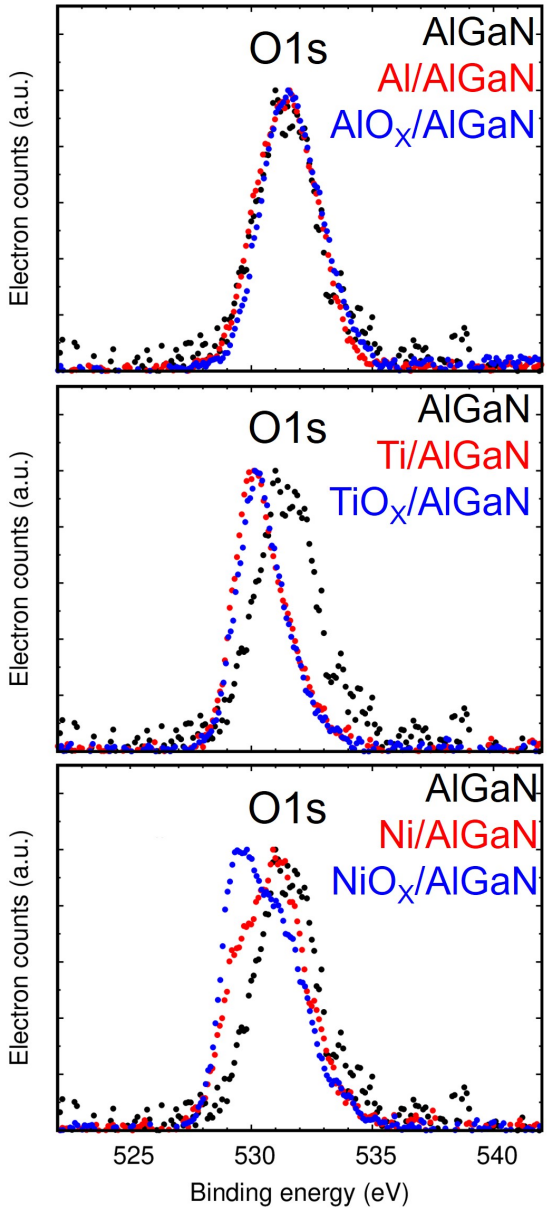

Figure 2.23: O1s spectra for each IL material.

We further focused on N1s and Ga3d spectra, where nitrogen and gallium atoms are considered to mainly exist in the interface. Figure 2.24 shows the N1s spectra for each IL material. For AlO_x/AlGaN and TiO_x/AlGaN, we find negligible peak position change, suggesting that the bonding state of nitrogen merely

changed during the interface reaction. While for NiO_x/AlGaN, peak positions shift to the high energy side, suggesting an increase in N-O bonding.

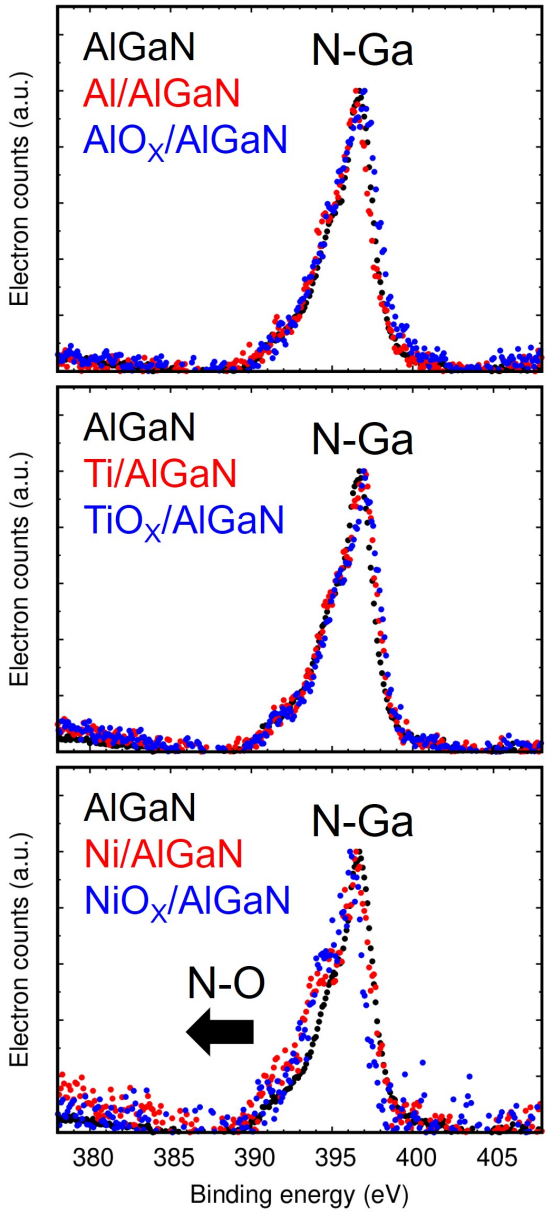

Figure 2.24: N1s spectra for each IL material.

Figure 2.25 shows the Ga3d spectra for each IL material. In the case of AlO_x/AlGaN, negligible peak position change is observed. While for TiO_x/AlGaN, high energy shifts are observed, suggesting an increase in Ga-O bonding. Therefore, it is possible that not only V_N donors, but also oxygen donors exist in the TiO_x/AlGaN interface. Furthermore, low energy shifts are observed for NiO_x/AlGaN, suggesting an increase in Ga-Ni bonding. This result supports the formation

of NiGa and the consequently existence of V_{Ga} acceptors in the NiO_x/AlGaN interface.

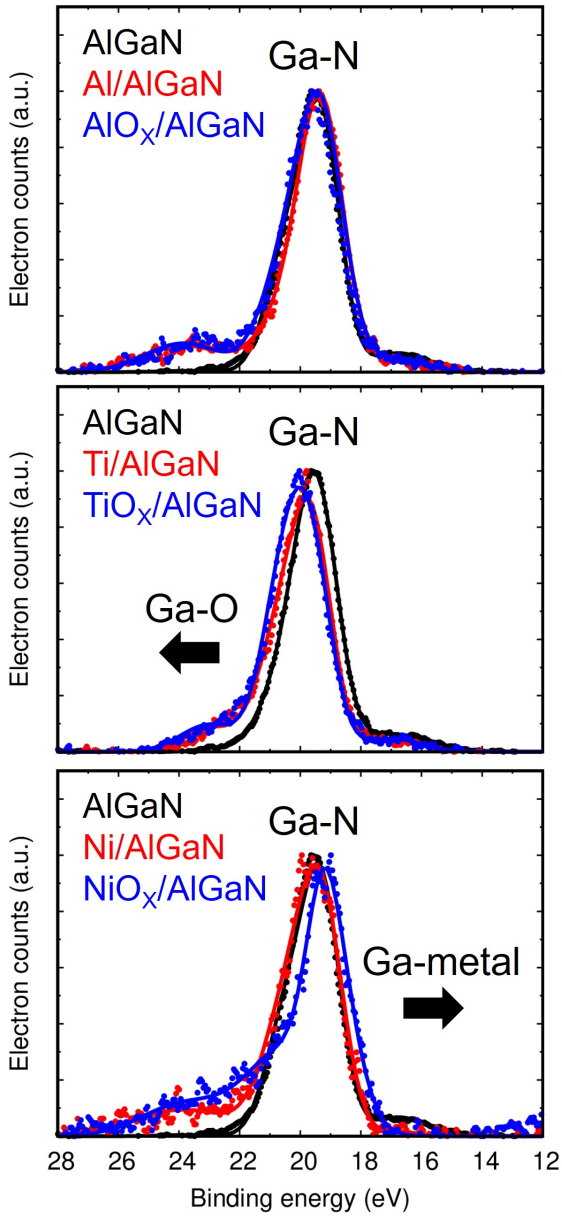

Figure 2.25: Ga3d spectra for each IL material with Gaussian peaks fitting.

Figure 2.26 shows the Al2p, Ti3p, and Ni3p spectra for the AlO_x/AlGaN, TiO_x/AlGaN, and NiO_x/AlGaN respectively. Sightly high energy shifts in AlO_x/AlGaN and TiO_x/AlGaN suggest increases in Al-O (or N), Ti-O (or N) bonding. Meanwhile, low energy shifts are observed for NiO_x/AlGaN, being consistent with the behavior of Ga3d spectra in supporting the formation of NiGa.

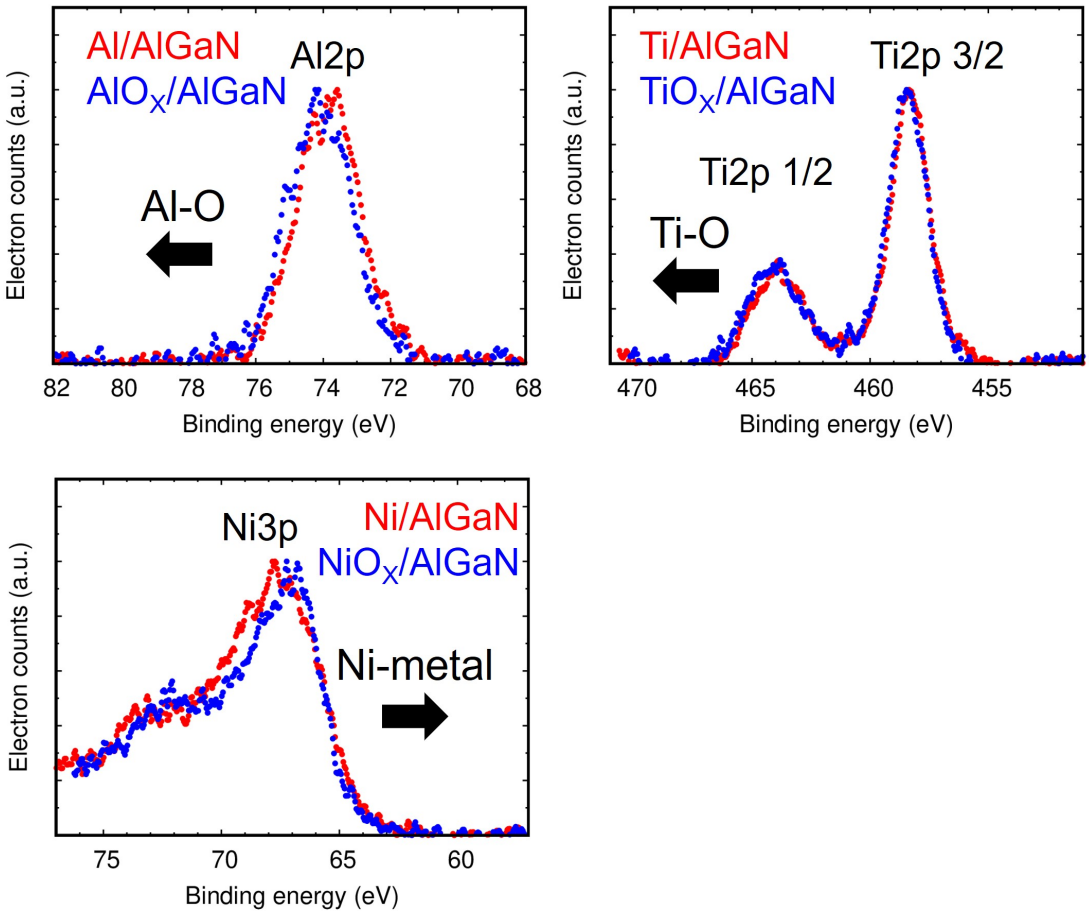

Figure 2.26: Al2p, Ti3p, and Ni3p spectra for each IL material respectively.

According to the XPS results, models of $AlO_x(TiO_x)/AlGaN$, and $NiO_x/AlGaN$ interface are depicted in Figure 2.27, where the oxygen donors and V_{Ga} acceptors are generate at the $AlO_x(TiO_x)/AlGaN$ and $NiO_x/AlGaN$ interface receptively.

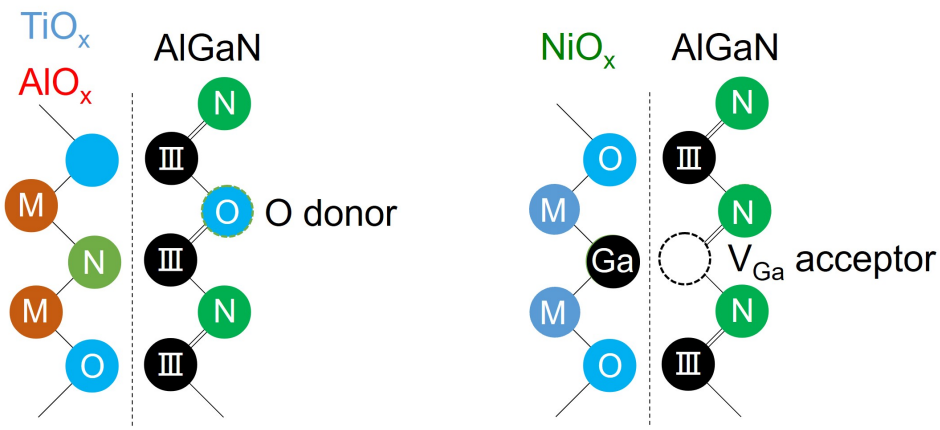

Figure 2.27: Models of $AlO_x(TiO_x)/AlGaN$, and $NiO_x/AlGaN$ interface.

Chapter 3

Effects of insulator-semiconductor interfacial layers (ILs) in metal/Al_2O_3/IL/AlGaN/GaN devices

According to the results in previous chapter, we carried out further investigation on effects of insulator-semiconductor ILs in metal/Al_2O_3/IL/AlGaN/GaN devices using the AlO_x, TiO_x, or NiO_x IL. We fabricated the metal/Al_2O_3/IL/AlGaN/GaN devices and obtained their C-V characteristics. From the Al_2O_3 thickness dependence of V_{th}, we find the fixed charge density of the Al_2O_3/IL/AlGaN interface, showing a positive correlation with the IL dipole density. In addition, by frequency (f)-dependent C-V characteristics, we characterized the interface trap density in the metal/Al_2O_3/IL/AlGaN/GaN devices using the conductance method. Temperature dependence of the f-dependent C-V characteristics is further investigated, where the time constant and the active energy of the interface traps are estimated.

3.1 Metal/Al_2O_3/IL/AlGaN/GaN device fabrication

Using the same AlGaN/GaN heterostructure, we fabricated metal/Al_2O_3/IL/AlGaN/GaN capacitor devices with the AlO_x, TiO_x, or NiO_x ILs, where Al_2O_3 are employed as the gate insulators. The fabrication main flow is shown in Fig. 3.1, consisting of Ohmic electrode formation, IL metal deposition, IL oxidation, insulator deposition, and gate electrode formation. After the IL oxidation, several thickness of Al_2O_3 gate insulators were formed by atomic layer deposition (ALD) using TMA (trimethyl aluminum) and water. The fabrication was completed by formation of Ni gate metal covered by Au. Metal/Al_2O_3/AlGaN/GaN capacitor devices with no IL were also fabricated for comparison.

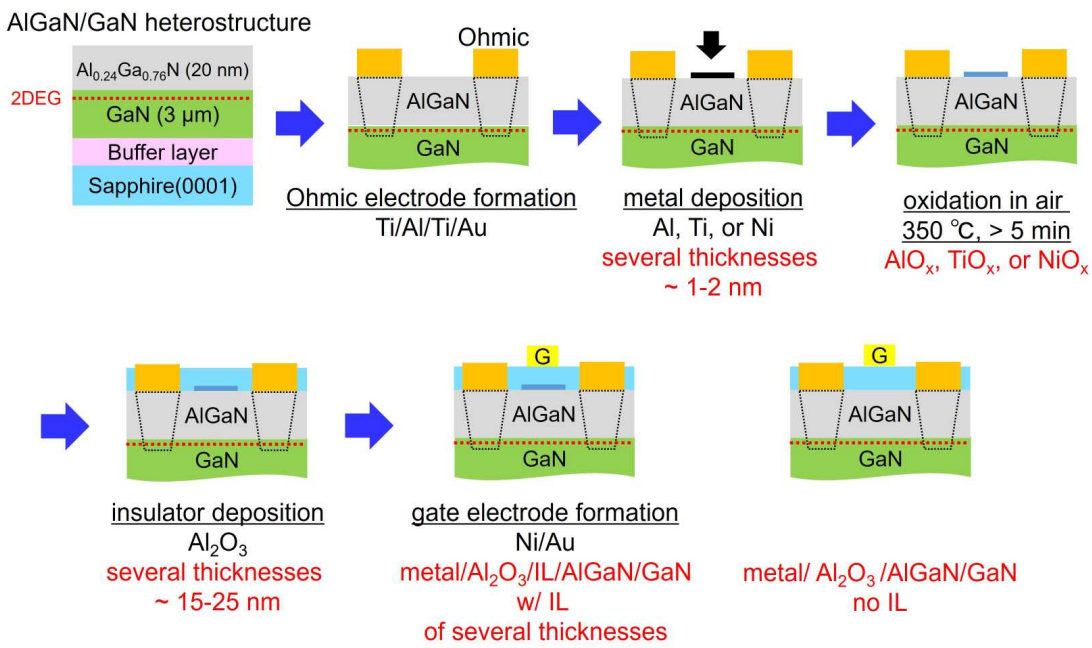

Figure 3.1: Metal/Al_2O_3/IL/AlGaN/GaN device fabrication main flow.

Ohmic electrode formation

The process is the same to the one of previous chapter.

IL metal deposition

The process is the same to the one of previous chapter.

IL oxidation

The process is the same to the one of previous chapter.

Insulator deposition

The process flow of the insulator deposition is shown in Fig. 3.2 with detailed conditions. The surface treatment of the no IL devices includes the TMAH treatment in order to remove surface oxidation, while this is unnecessary for devices with ILs.

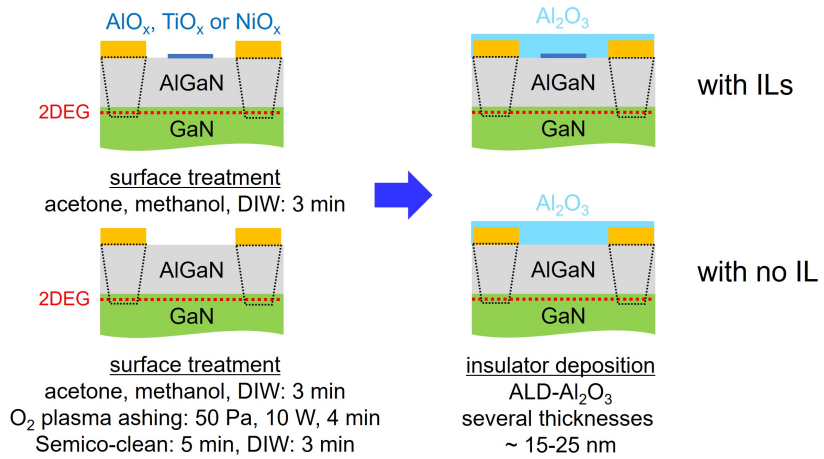

Figure 3.2: Process flow of the insulator deposition.

The Al_2O_3 insulators are obtained by atomic layer deposition (ALD), using trimethyl aluminum $Al(CH_3)_3$ (TMA), and water H_2O as precursors. Figure 3.3 shows the chemical structure of the TMA, which react with water as

$$2Al(CH_3)_3 + 3H_2O \rightarrow Al_2O_3 + 6CH_4,$$

forming the Al_2O_3 insulator layer of one mono-layer. By controlling the the total numbers of the reaction, it is possible to accurately control the thickness of Al_2O_3 as shown in Fig. 3.4.

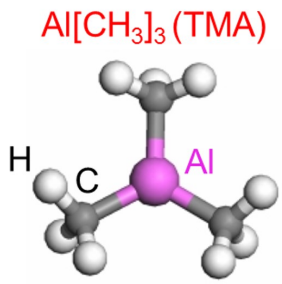

Figure 3.3: Chemical structure of TMA.

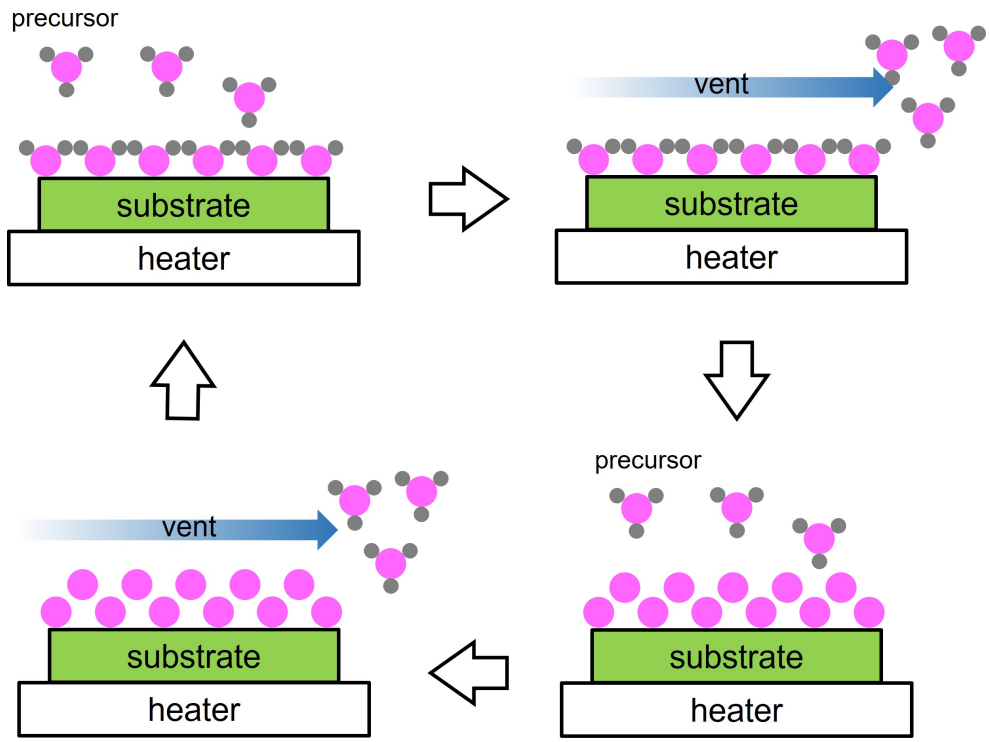

Figure 3.4: ALD deposition sequences.

Gate electrode formation

The process is the same to the one of previous chapter.

3.2 Metal/Al_2O_3/IL/AlGaN/GaN devices characterization

Current-voltage (J-V) characterizations

Figure 3.5 shows the top view of a fabricated capacitor and the configuration of J-V (DC) characterization for the capacitors using semiconductor parameter analyzer.

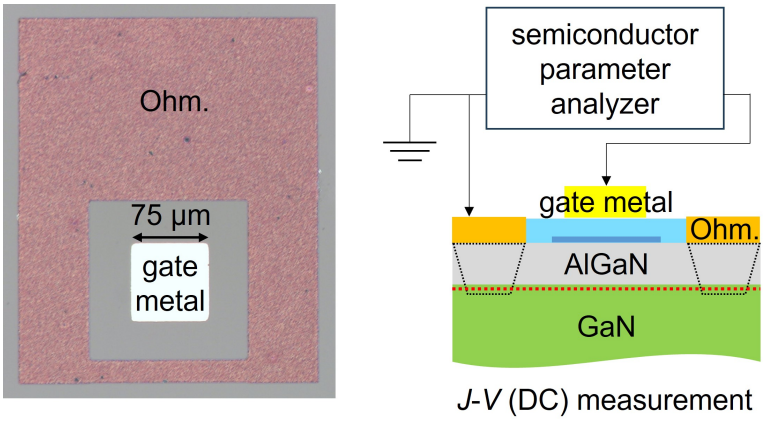

Figure 3.5: Top view of a fabricated capacitor and the configuration of J-V (DC) or C-V (AC) characterization.

Figure 3.6 shows examples of current-voltage (J-V) characteristics of the capacitors, where one device is picked up for each IL and each Al_2O_3 thickness, under application of the gate voltage V_G with respect to the grounded Ohmic electrode. In comparison to the metal/IL/AlGaN/GaN devices, leakage is reduced dramatically due to the Al_2O_3 gate insulator, leading to a negligible contribution from ILs.

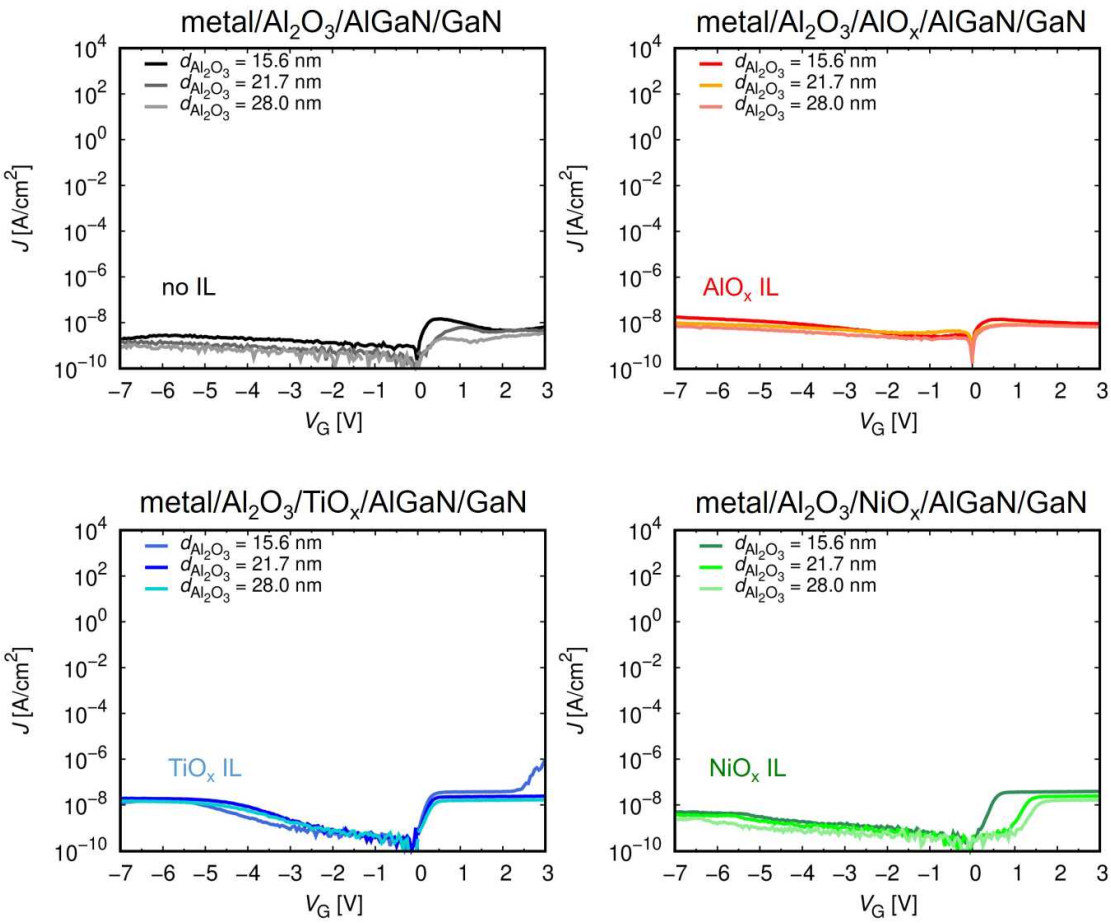

Figure 3.6: J-V characteristics of metal/Al_2O_3/AlGaN/GaN and metal/Al_2O_3/IL/AlGaN/GaN devices.

Capacitance-voltage (C-V) characterizations

Figure 3.7 shows the configuration C-V (AC) characterization for the capacitors using LCR meter.

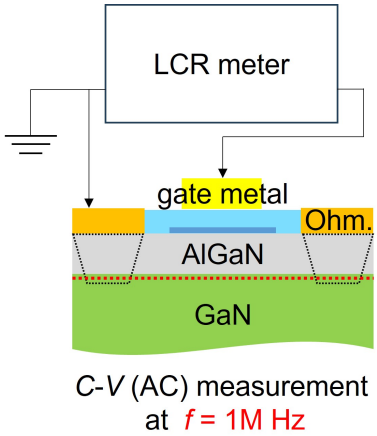

Figure 3.7: The configuration of C-V (AC) characterization at $f = 1$M Hz.

Figure 3.8 shows examples of C-V characteristics at $f = 1$ MHz. The 2DEG concentration n_s obtained by integrating the C-V characteristics is also shown in Fig. 3.8, and fitted by $qn_s \simeq C_{tot}(V_G - V_{th})$ using the total capacitance C_{tot} given by $1/C_{tot} = 1/C_{Al_2O_3} + 1/C_{AlGaN} + 1/C_{IL}$.

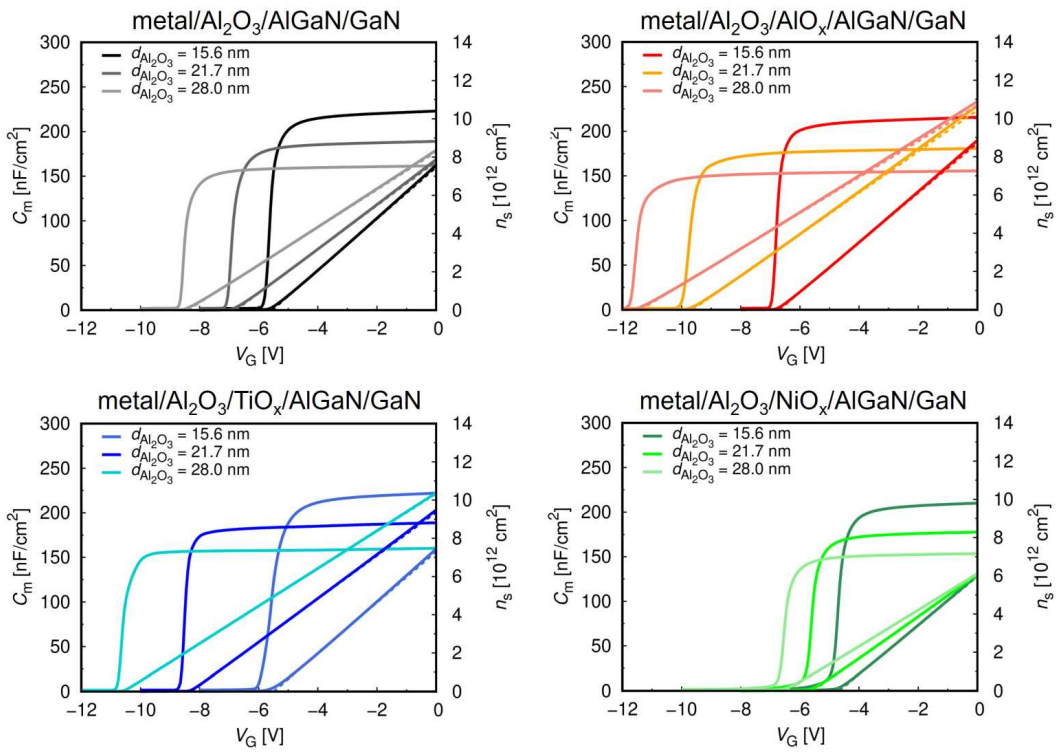

Figure 3.8: C-V characteristics of metal/Al_2O_3/AlGaN/GaN and metal/Al_2O_3/IL/AlGaN/GaN devices.

From the fitting, we obtain V_{th} and C_{tot}. Examples of $1/C_{\mathrm{tot}}$ are shown in Fig. 3.9 as functions of the Al_2O_3 thickness $d_{Al_2O_3}$, which give $C_{Al_2O_3} = k_{\mathrm{ins}}\epsilon_0/d_{Al_2O_3}$ from the slope, and C_{AlGaN} and C_{IL} from the intercept at $d_{Al_2O_3} = 0$. On the other hand, Fig. 3.10 shows examples of V_{th} as functions of the $d_{Al_2O_3}$, where the AlO_x and TiO_x ILs lead to more negative V_{th} shifts, while the NiO_x ILs lead to less negative ones.

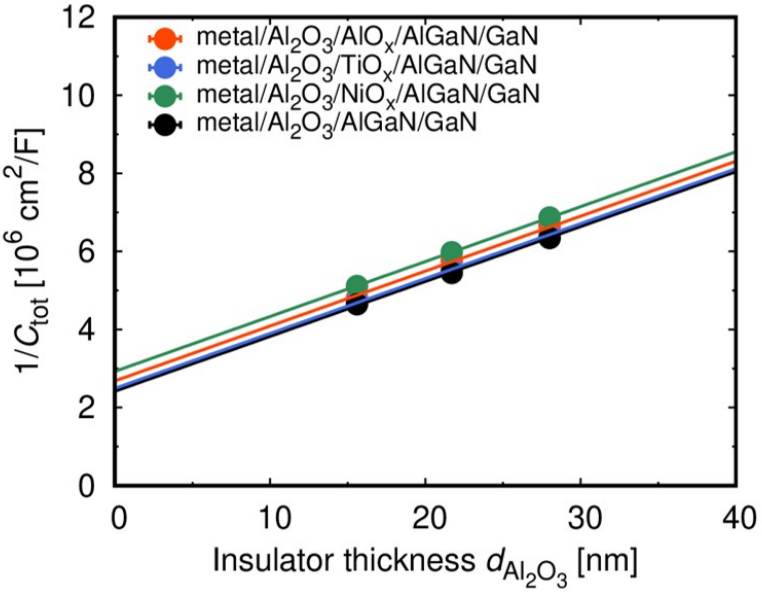

Figure 3.9: The inverse of total capacitances $1/C_{\mathrm{tot}}$.

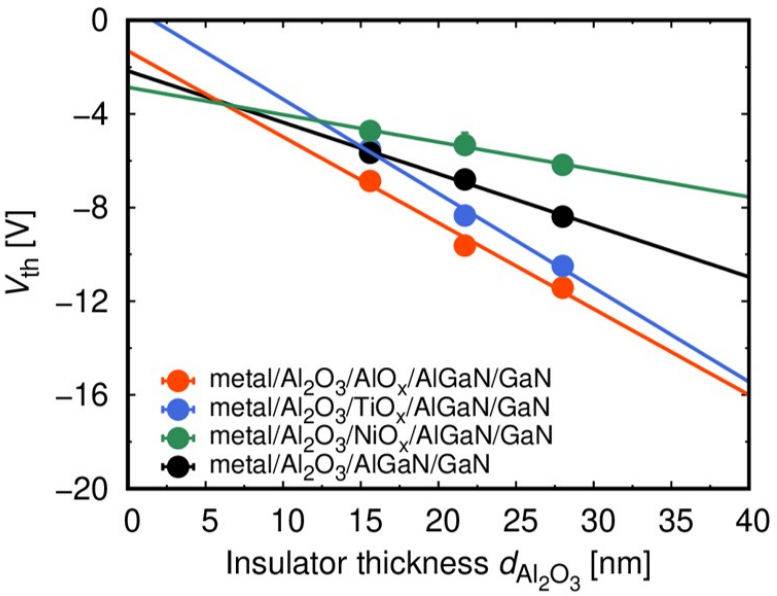

Figure 3.10: The threshold voltages V_{th} depending on the insulator thicknesses $d_{Al_2O_3}$.

Figure 3.11 shows the band diagram of a metal/Al_2O_3/IL/AlGaN/GaN device, from which the threshold voltage V_{th} is given by

$$\begin{aligned} V_{\mathrm{th}} &= \frac{\phi}{q} - \frac{\sigma_{\mathrm{int}} - \sigma_{\mathrm{GaN}}}{C_{\mathrm{Al_2O_3}}} - \frac{\varphi}{q} - \frac{\sigma_{\mathrm{AlGaN}} - \sigma_{\mathrm{GaN}}}{C_{\mathrm{AlGaN}}} - \frac{\Delta E_{\mathrm{C}}}{q} \\ &= \frac{\sigma_{\mathrm{GaN}} - \sigma_{\mathrm{int}}}{k_{\mathrm{Al_2O_3}}\epsilon_0} d_{\mathrm{Al_2O_3}} - \frac{\sigma_{\mathrm{AlGaN}} - \sigma_{\mathrm{GaN}}}{C_{\mathrm{AlGaN}}} + \frac{\phi - \varphi - \Delta E_{\mathrm{C}}}{q}, \end{aligned} \tag{3.1}$$

where $C_{\mathrm{Al_2O_3}} = k_{\mathrm{Al_2O_3}}\varepsilon_0/d_{\mathrm{Al_2O_3}}$ is the the Al_2O_3 capacitance given by the Al_2O_3 dielectric constant $k_{\mathrm{Al_2O_3}}$ and the thickness $d_{\mathrm{Al_2O_3}}$, ϕ is the metal-Al_2O_3 barrier height, φ is the effective Al_2O_3-AlGaN conduction band offset, $\sigma_{\mathrm{int}} = \sigma_{\mathrm{D}} - \tilde{\sigma}_{\mathrm{D}}$ is the fixed charge density of the Al_2O_3/IL/AlGaN interface due to the unbalanced IL dipole[1]. It should be noted that V_{th} is a linear function of $d_{\mathrm{Al_2O_3}}$, where the slope is $(\sigma_{\mathrm{GaN}} - \sigma_{\mathrm{int}})/(k_{\mathrm{Al_2O_3}}\varepsilon_0)$, and the intercept is $-(\sigma_{\mathrm{AlGaN}} - \sigma_{\mathrm{GaN}})/C_{\mathrm{AlGaN}} + (\phi - \varphi - \Delta E_{\mathrm{C}})/q$. From the former, we can evaluate σ_{int} due to the unbalanced IL dipole. Also the latter is determined by $\phi - \varphi$, where φ is affected by the the vacuum level step ΔE_{vac} induced by the dipole of the insulator-AlGaN IL.

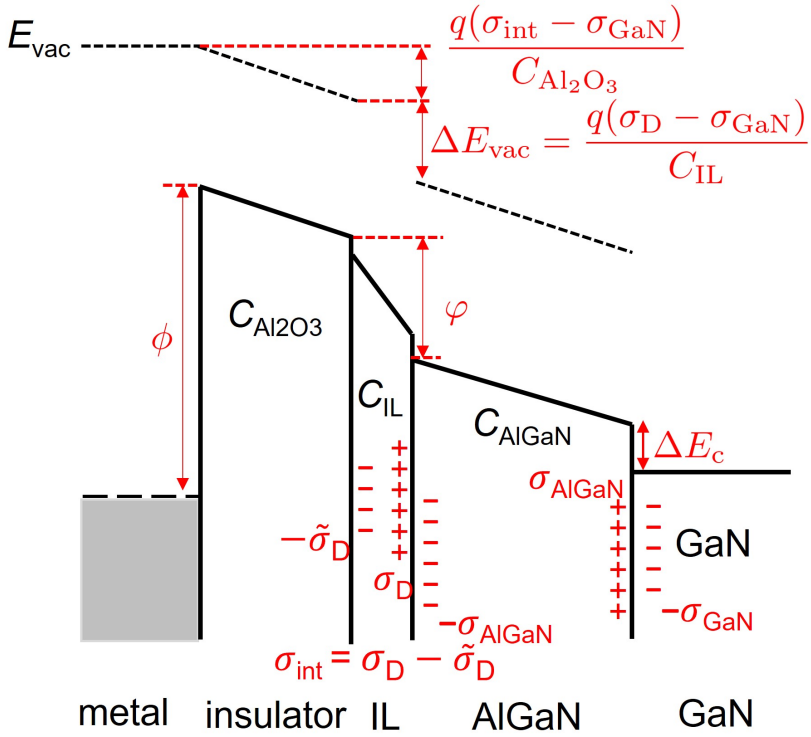

Figure 3.11: The band diagram of the metal/Al_2O_3/IL/AlGaN/GaN devices.

[1]see Appendix A for detailed derivation

Using Eq. (A.8), we evaluate $\sigma_{\rm int}/q$ shown in Fig. 3.12 as functions of $1/C_{\rm IL}$ with error bars standing for the three-sigma asymptotic standard errors of the linear fitting. Although the error bars are slightly large, $\sigma_{\rm int}/q$ is almost independent of $1/C_{\rm IL}$ for each IL, and the averaged $\sigma_{\rm int}/q$ is $\simeq 3.2 \times 10^{13}$ cm^{-2} for no IL, $\simeq 3.6 \times 10^{13}$ cm^{-2} for the AlO_x ILs, $\simeq 3.9 \times 10^{13}$ cm^{-2} for the TiO_x ILs, and $\simeq 2.7 \times 10^{13}$ cm^{-2} for the NiO_x ILs.

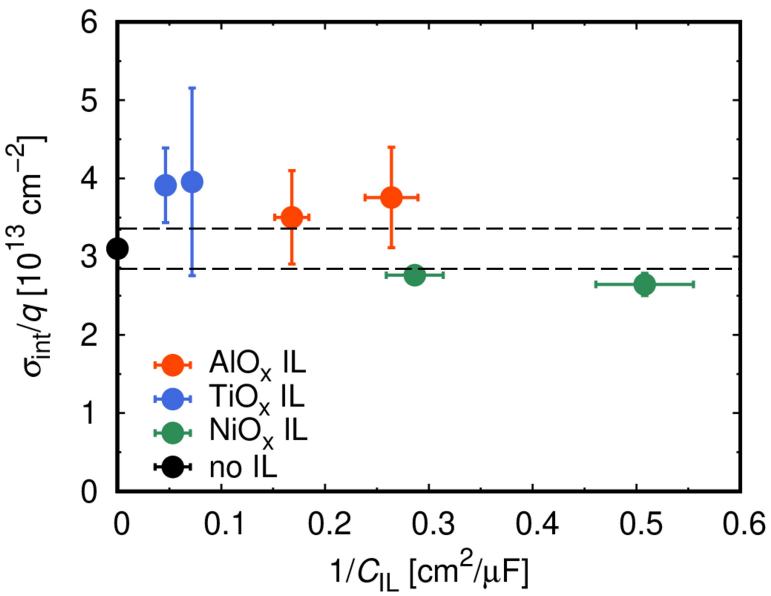

Figure 3.12: The relation between the fixed charge densities $\sigma_{\rm int}$ of all the devices and $1/C_{\rm IL}$.

Using the IL dipole density $\sigma_{\rm D}$ obtained for each IL material in the previous section, the relation between $\sigma_{\rm int}$ and $\sigma_{\rm D}$ is demonstrated in Fig. 3.13, showing a positive correlation. This suggests that the fixed charge is related to the unbalanced IL dipole.

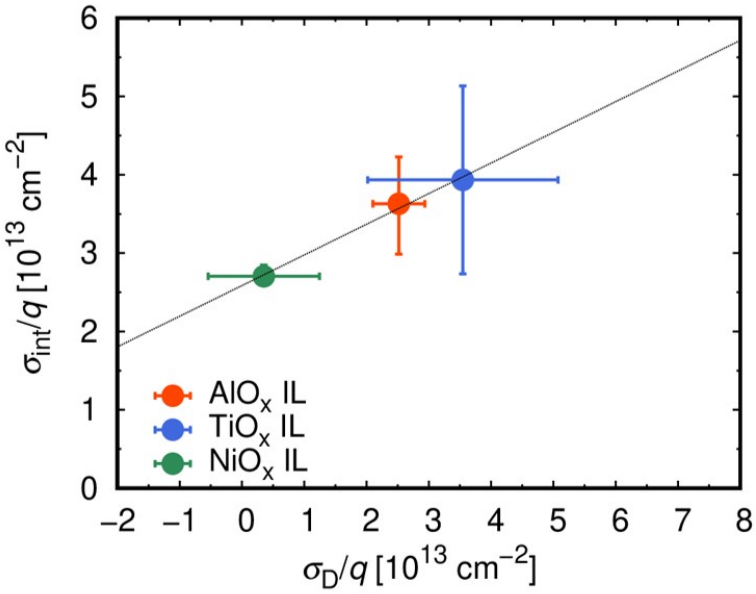

Figure 3.13: The fixed charge density σ_{int} correlated with the IL dipole density σ_{D}.

On the other hand, assuming a metal/Al_2O_3 barrier height $\phi = 4.6$ eV [51], the band offset φ is evaluated to be $\varphi \simeq 2.1 \pm 1$ eV for no IL, $\varphi \simeq 2.5$ eV for the NiO_x ILs, and $\varphi \sim$ 0-5 eV for the AlO_x or TiO_x ILs as shown in Fig. 3.14 where the uncertainty comes from the asymptotic standard errors of the linear fitting. Owing to this large uncertainty, unfortunately it is difficult to discuss φ affected of the vacuum level step ΔE_{vac}.

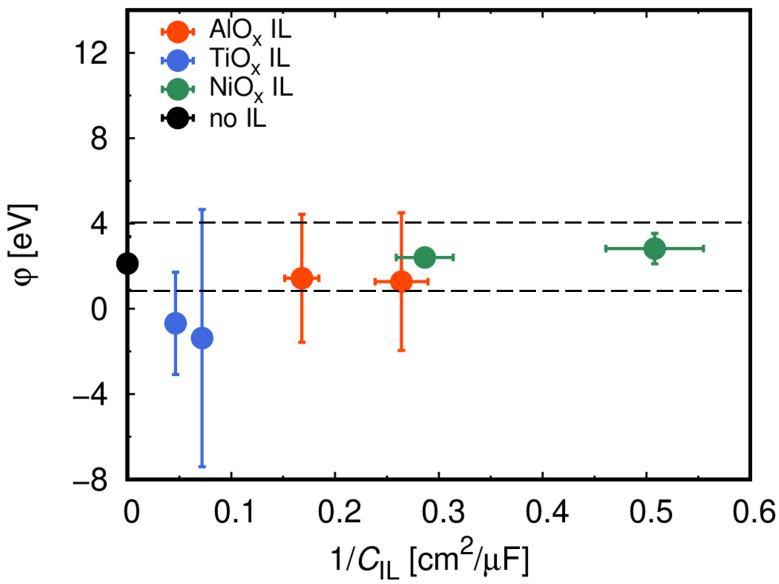

Figure 3.14: The relation between the band offset φ of all the devices and $1/C_{\mathrm{IL}}$.

Figure 3.15 shows the calculated 1D Poisson-Schrödinger band diagrams of the metal/Al_2O_3/AlGaN/GaN and metal/Al_2O_3/IL/AlGaN/GaN devices at V_G = 0 V, where the Al_2O_3 thickness is 22 nm. The Al_2O_3/AlO_x/AlGaN and Al_2O_3/TiO_x/AlGaN interfaces are almost neutral, while the Al_2O_3/NiO_x/AlGaN interface is negatively charged due to a suppression of the positive fixed charge.

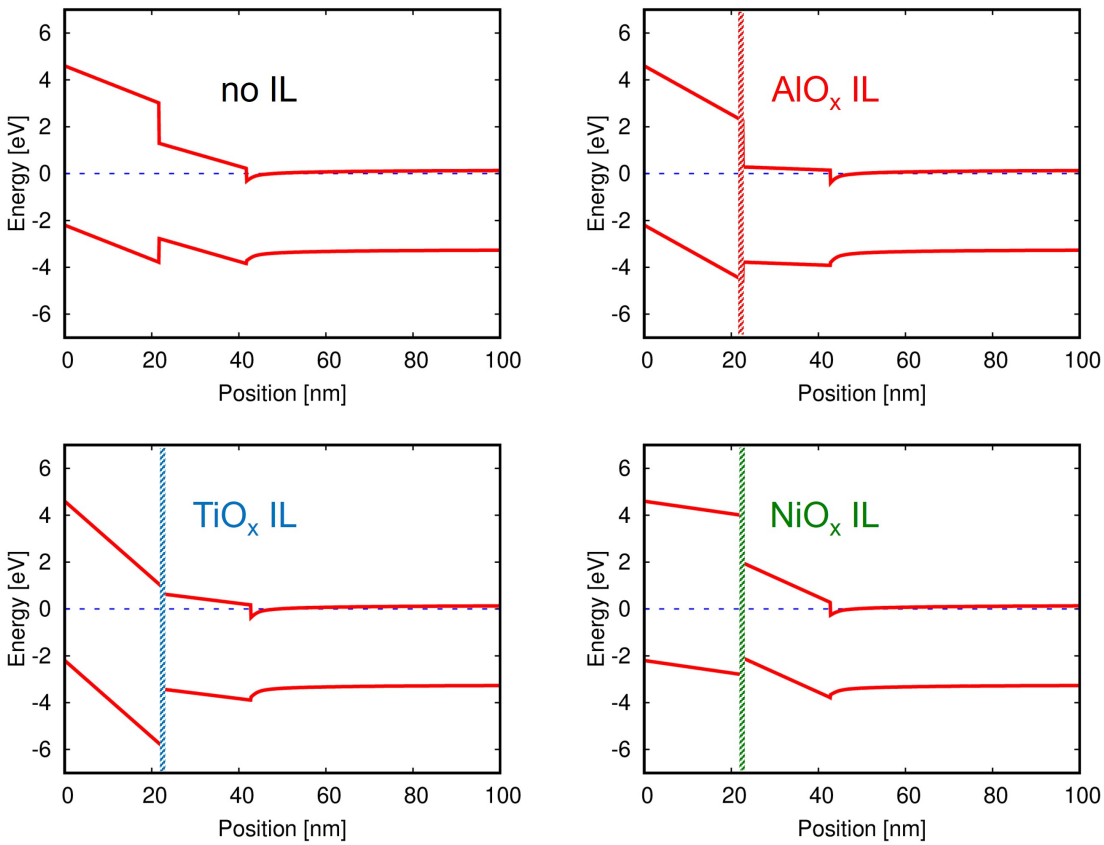

Figure 3.15: The calculated 1D Poisson-Schrödinger band diagrams of the metal/Al_2O_3/AlGaN/GaN and metal/Al_2O_3/IL/AlGaN/GaN devices.

Capacitance-voltage-frequency (C-V-f) characterizations

Due to the insertion of insulator-semiconductor ILs, the number of interface increased as shown in Fig. 3.16. This may lead to an increase of interface traps in the metal/IL/AlGaN interface.

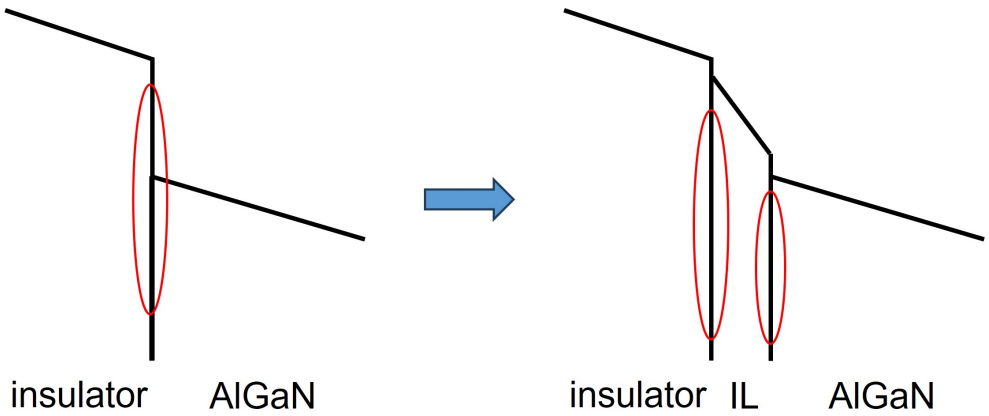

Figure 3.16: The interface increase due to the insertion of an insulator-semiconductor IL.

Thus, we characterized the trap densities of the Al_2O_3/IL/AlGaN interfaces by f-dependent C-V measurements for f = 100-1M Hz, using the configuration shown in Fig. 3.17.

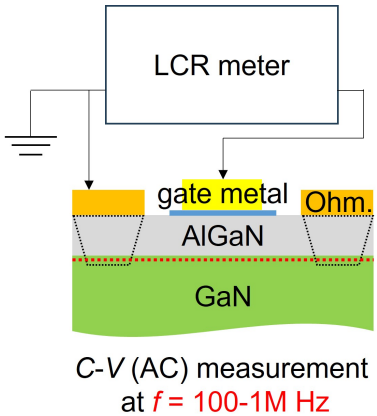

Figure 3.17: The configuration of C-V-f (AC) characterization at f = 100-1M Hz.

Examples of f-dependent C-V characteristics of devices with $d_{Al_2O_3}$ = 22 nm are shown in Fig. 3.18. Negligible frequency dispersion is observed at negative bias region for all devices, showing that the V_{th} determination is not affected by the measurement frequency. On the other hand, frequency dispersions are observed for positive biases except for TiO_x ILs. By using the conductance method [88], which is widely employed for interface characterization [48, 68, 89], the interface trap density was evaluated using the equivalent circuits shown in the inset of

Fig. 3.18[2].

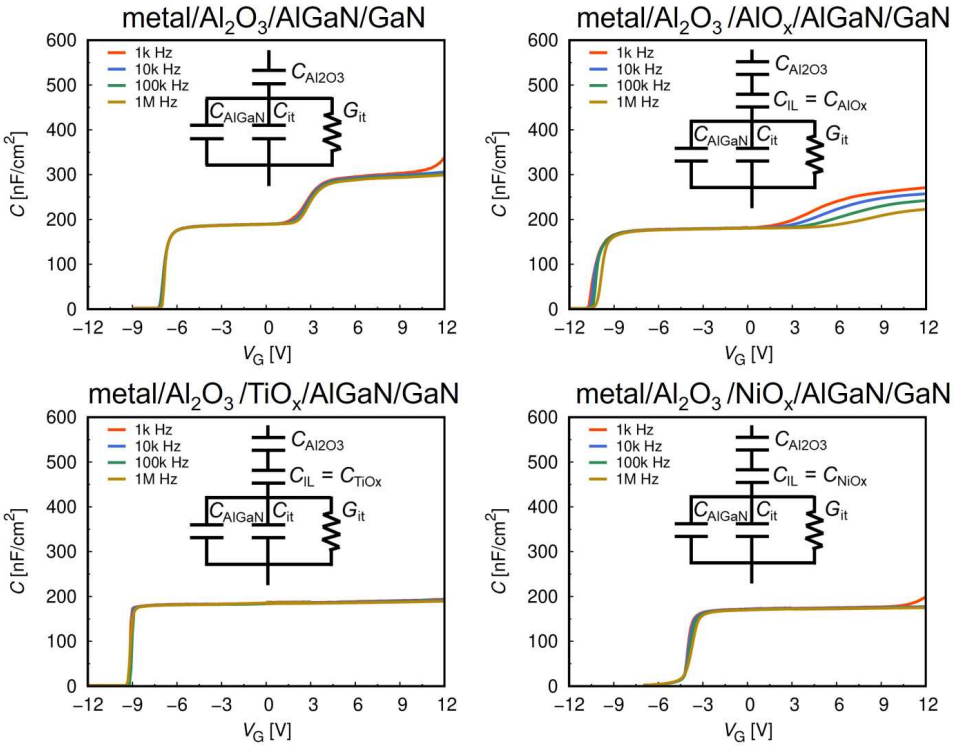

Figure 3.18: C-V-f characteristics of metal/Al_2O_3/AlGaN/GaN and metal/Al_2O_3/IL/AlGaN/GaN devices.

In those equivalent circuits, G_{it} is the interface trap conductance, and C_{it} is the interface trap capacitance. When we carry out C-V measurements, the equivalent circuit will be transform into the measured circuit shown in Fig. 3.19(right), where C_{m} and G_{m} are the measured capacitance and conductance, respectively.

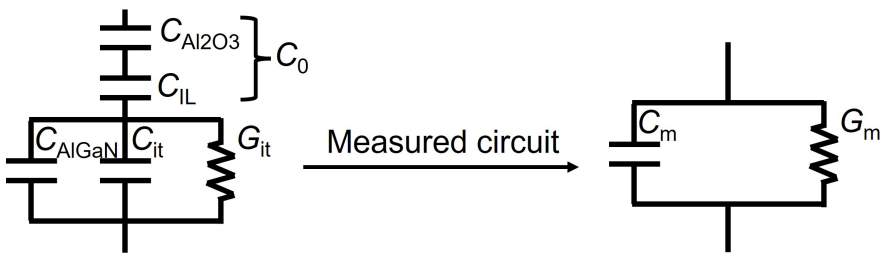

Figure 3.19: The equivalent circuit of the MIS capacitor and the measured circuit.

[2]see Appendix B

Therefore, using $1/C_0$=$(1/C_{\mathrm{Al_2O_3}})$+$(1/C_{\mathrm{IL}})$, we have the total impedance given by

$$\begin{aligned} Z &= \frac{1}{j\omega C_0} + \frac{1}{j\omega C_{\mathrm{AlGaN}} + j\omega C_{\mathrm{it}} + G_{\mathrm{it}}} \text{ (equivalent circuit)} \\ &= \frac{1}{j\omega C_{\mathrm{m}} + G_{\mathrm{m}}} \text{ (measured circuit).} \end{aligned} \tag{3.2}$$

Thus,

$$\begin{aligned} \frac{1}{j\omega(C_{\mathrm{AlGaN}} + C_{\mathrm{it}}) + G_{\mathrm{it}}} &= \frac{1}{j\omega C_{\mathrm{m}} + G_{\mathrm{m}}} - \frac{1}{j\omega C_0} \\ &= \frac{j\omega(C_0 - C_{\mathrm{m}}) - G_{\mathrm{m}}}{(j\omega C_{\mathrm{m}} + G_{\mathrm{m}})j\omega C_0}. \end{aligned} \tag{3.3}$$

As a result,

$$\begin{aligned} j\omega(C_{\mathrm{AlGaN}} + C_{\mathrm{it}}) + G_{\mathrm{it}} &= \frac{(j\omega C_{\mathrm{m}} + G_{\mathrm{m}})j\omega C_0}{j\omega(C_0 - C_{\mathrm{m}}) - G_{\mathrm{m}}} \\ &= -\frac{(-\omega^2 C_0 C_{\mathrm{m}} + j\omega C_0 G_{\mathrm{m}})[j\omega(C_0 - C_{\mathrm{m}}) + G_{\mathrm{m}}]}{\omega^2(C_0 - C_{\mathrm{m}})^2 + {G_{\mathrm{m}}}^2} \\ &= \frac{\omega^2(C_0 - C_{\mathrm{m}})C_0 G_{\mathrm{m}} + \omega^2 C_0 C_{\mathrm{m}} G_{\mathrm{m}}}{\omega^2(C_0 - C_{\mathrm{m}})^2 + {G_{\mathrm{m}}}^2} + j \times ... \end{aligned} \tag{3.4}$$

Equating two sides for Eq. 3.4 and extracting the real part, we obtain

$$\frac{G_{\mathrm{it}}}{\omega} = \frac{\omega {C_0}^2 G_{\mathrm{m}}}{\omega^2(C_0 - C_{\mathrm{m}})^2 + {G_{\mathrm{m}}}^2}, \tag{3.5}$$

from which we can calculate the interface trap conductance from the measurement data.

Figure 3.20 shows examples of G_{it}/ω ($\omega = 2\pi f$) as functions of frequency f, exhibiting single-peaked behaviors except for the TiO_x ILs.

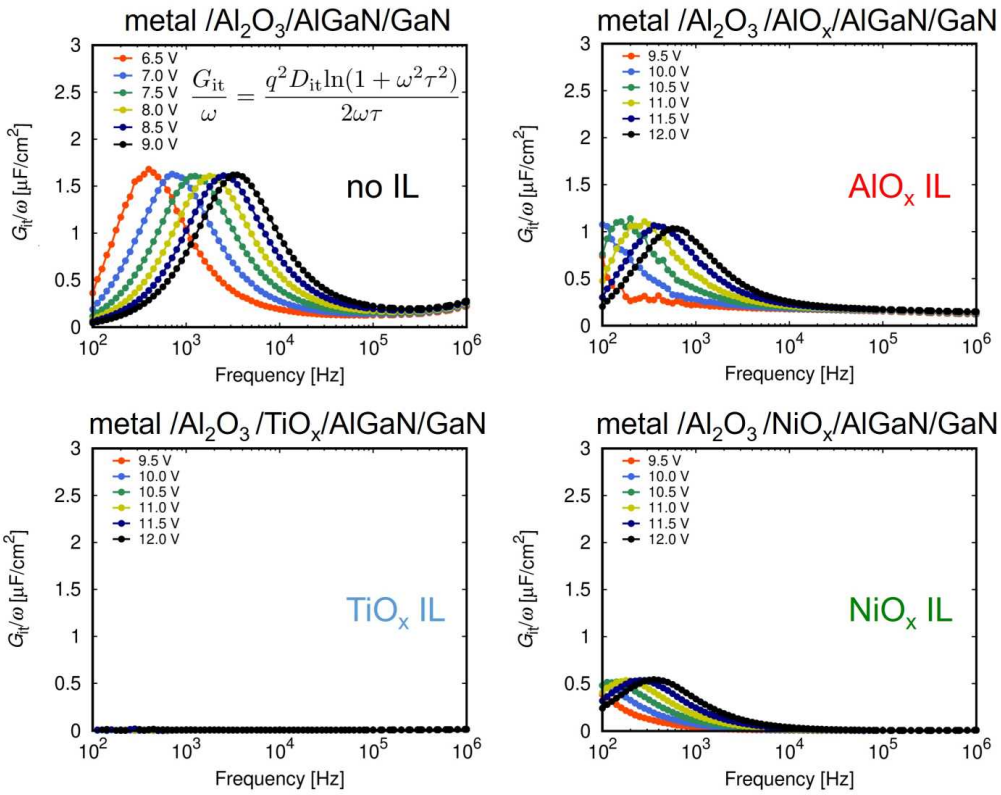

Figure 3.20: G_{it}/ω as functions of frequency with fitting curves for metal/Al_2O_3/AlGaN/GaN and metal/Al_2O_3/IL/AlGaN/GaN devices.

These single-peaked behavior is described by

$$\frac{G_{\mathrm{it}}}{\omega} = \frac{q^2 D_{\mathrm{it}} \ln(1+\omega^2\tau^2)}{2\omega\tau}, \tag{3.6}$$

where the electron trapping time constant τ is given by the peak frequency $f_{\mathrm{p}} = 1/(\pi\tau)$ and the interface trap density D_{it} by the peak value $G_{\mathrm{it}}/\omega \simeq 0.4q^2 D_{\mathrm{int}}$ as shown in Figure 3.21[3].

[3]see Appendix B

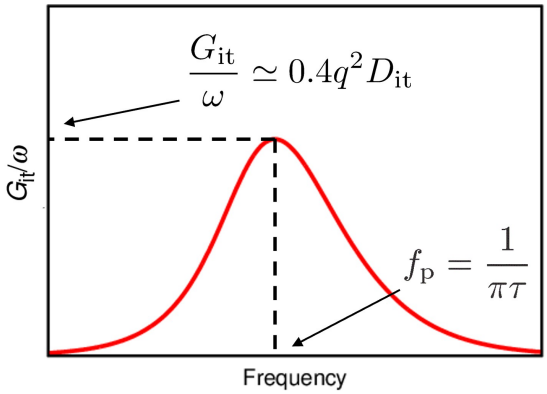

Figure 3.21: The interface trap density $D_{\rm it}$ and the electron trapping time constant τ extractions form $G_{\rm it}/\omega$ as a function of measured frequency f.

The absence of single-peaked behavior for the TiO_x ILs suggests that the interface trap have a very long trapping time constant. The peak values of $G_{\rm it}/\omega$ for all the devices are shown Fig. 3.22 as functions of frequency, from which we extract the $D_{\rm it}$ and τ shown in Fig. 3.23. For an interface trap at the energy E, the time constant τ at temperature T is given by

$$\tau = {\rm e}^{(E_{\rm C}-E)/k_{\rm B}T}/(v_{\rm th}\sigma_{\rm e}N_{\rm C}) = \tau_0 {\rm e}^{(E_{\rm C}-E)/k_{\rm B}T}, \tag{3.7}$$

using the conduction band bottom energy $E_{\rm C}$, the electron thermal velocity $v_{\rm th}$, the capture cross section of the trap $\sigma_{\rm e}$, and the conduction band effective density of states $N_{\rm C}$, where $\tau_0 = 1/(v_{\rm th}\sigma_{\rm e}N_{\rm C})$. Even though the τ_0 is ambiguous due to the uncertain $\sigma_{\rm e}$, by assuming a wide range of $\tau_0 \sim 0.1\text{-}10^3$ ps, $D_{\rm it}$ as functions of $E_{\rm C} - E$ are evaluated and shown in Fig. 3.24, where the error bars correspond to the widely assumed τ_0.

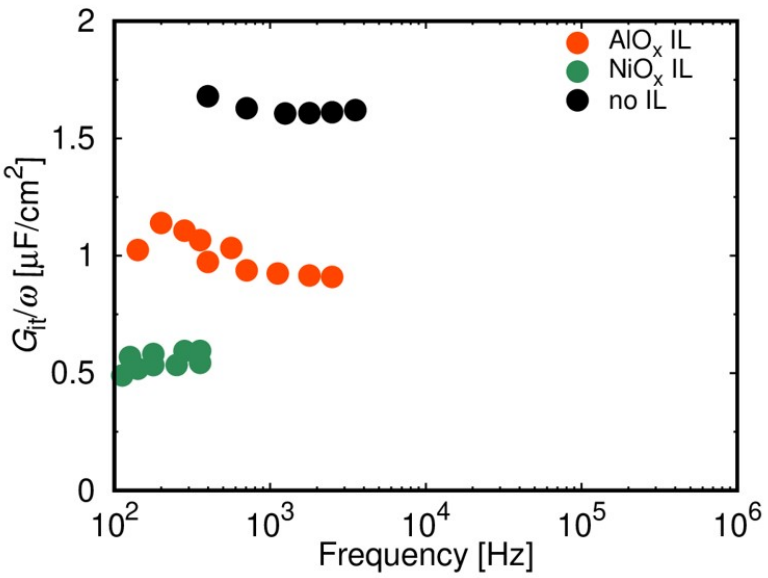

Figure 3.22: Peak values of G_{it}/ω as functions of measured frequency f.

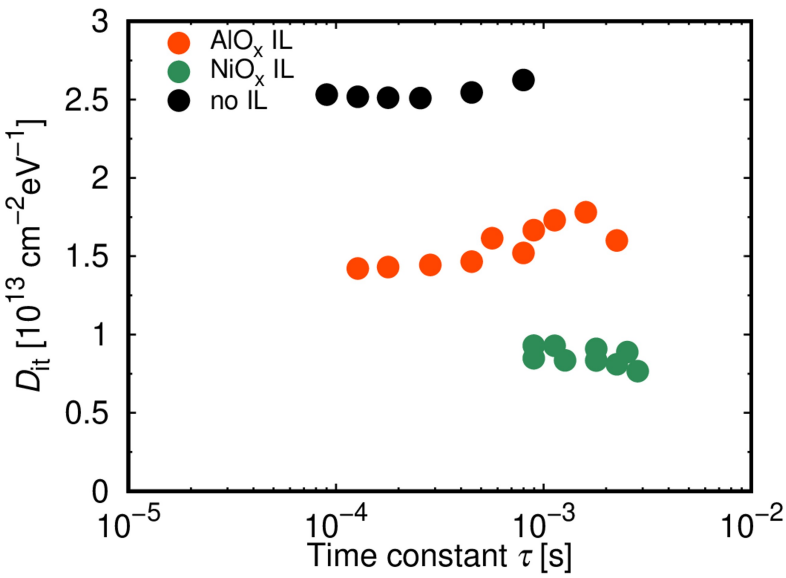

Figure 3.23: D_{it} as functions of τ.

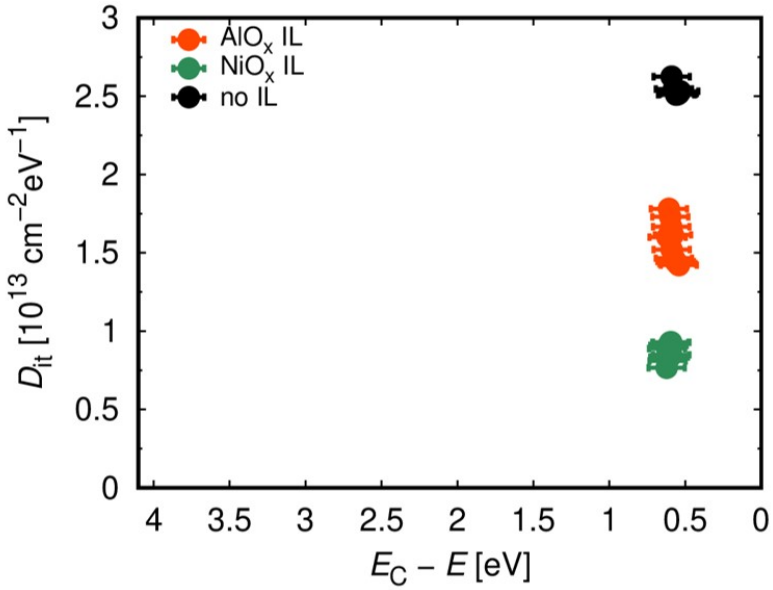

Figure 3.24: The interface trap density $D_{\rm it}$ as functions of the energy $E_{\rm C} - E$.

The shallow interface trap densities are $D_{\rm it} \simeq 2.5$ cm^{-2}eV^{-1} for no IL, $D_{\rm it} \simeq 1.6$ cm^{-2}eV^{-1} for the AlO$_x$ ILs, and $D_{\rm it} \simeq 0.6$ cm^{-2}eV^{-1} for the NiO$_x$ ILs. This means that $D_{\rm it}$ for no IL is higher than those for the AlO$_x$ and NiO$_x$ ILs, despite of the apparently weak frequency dispersion in the C-V characteristics for no IL shown in Fig. 13. We consider that this behavior can be explained as follows. In Fig. 14 for no IL, in addition to the observed peak, we find the tail of another next peak of $G_{\rm it}/\omega$ at $\lesssim 1$ MHz for forward biases, with a peak frequency rather higher ($\gg 1$ MHz) than the measurement frequency range, and a peak value comparable to the observed peak at $\sim$ kHz. When there is such another next peak, $C_{\rm it}$ in the equivalent circuit becomes quite large in the measurement frequency range, and thus we will obtain the measured capacitance $C_{\rm m} \simeq C_{\rm Al_2O_3}$, which hardly shows frequency dispersion.

While the equivalent circuit is usually described by Eq. 3.6 and

$$C_{\rm it} = \frac{q^2 D_{\rm it} {\rm atan}(\omega\tau)}{\omega\tau}, \tag{3.8}$$

where $D_{\rm it}$ is the trap density and τ is the trapping time constant, for the equivalent circuit with such another kind of traps, we should use

$$\frac{G_{\rm it}}{\omega} = \frac{q^2 D_{\rm it} \ln(1+\omega^2\tau^2)}{2\omega\tau} + \frac{q^2 \tilde{D}_{\rm it} \ln(1+\omega^2\tilde{\tau}^2)}{2\omega\tilde{\tau}} \tag{3.9}$$

and

$$C_{\mathrm{it}} = \frac{q^2 D_{\mathrm{it}} \mathrm{atan}(\omega\tau)}{\omega\tau} + \frac{q^2 \tilde{D}_{\mathrm{it}} \mathrm{atan}(\omega\tilde{\tau})}{\omega\tilde{\tau}} \tag{3.10}$$

with the density $\tilde{D}_{\mathrm{it}}$ and the time constant $\tilde{\tau}$ of the another kind of traps. By assuming $C_{\mathrm{Al_2O_3}} = 300$ nF/cm^2, $C_{\mathrm{AlGaN}} = 400$ nF/cm^2, $D_{\mathrm{it}} = 2.5 \times 10^{13}$ cm^{-2}eV^{-1}, $\tau = 10^{-4}$ s, $\tilde{D}_{\mathrm{it}} = 3.0 \times 10^{13}$ cm^{-2}eV^{-1}, and $\tilde{\tau} = 10^{-8}$ s, which are realistic for the experiments, we carried out a model calculation to illustrate this modification. G_{it}/ω, C_{it}, and C_{m} were calculated as shown in Figs. 3.25, 3.26, and 3.27 respectively for the cases without (blue curves) and with (red curves) the next peak. In the measurement frequency range, we observe similar G_{it}/ω for the cases without and with the next peak, except that the tail of the next peak can be found at $\lesssim 1$ MHz as in the measured results. Moreover, in the measurement frequency range, while the variation of C_{it} is 0 - μF/cm^2 for the case without the next peak, C_{it} remain at μF/cm^2 order for the case with the next peak. As the results, frequency dispersion can be observed in the case without the next peak. In the case with the next peak, however, due to the high $C_{\mathrm{it}} \sim \mu$F/cm^2, the measured capacitance becomes $C_{\mathrm{m}} \simeq C_{\mathrm{Al_2O_3}}$, which hardly shows frequency dispersion. This explains the observed weak frequency dispersion for no IL, and implies that it is difficult to discuss the trap density only by apparent C-V characteristics.

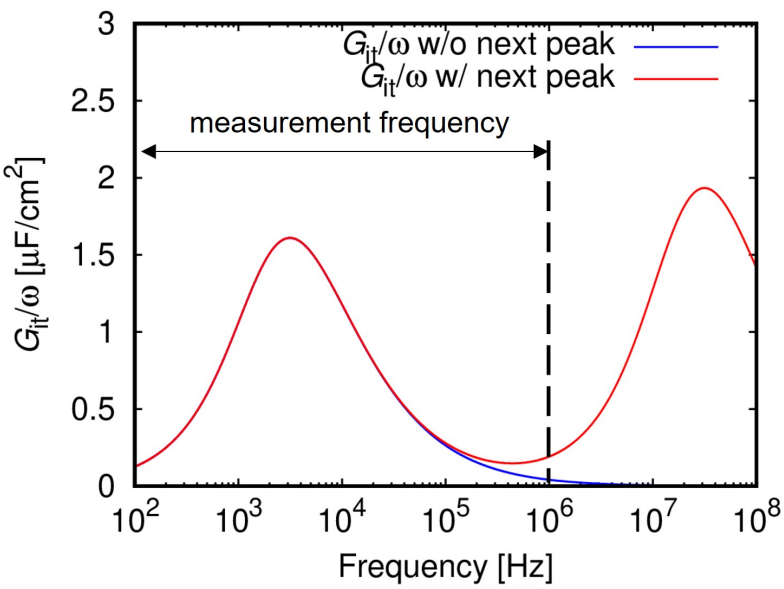

Figure 3.25: The calculated G_{it}/ω as functions of the frequency.

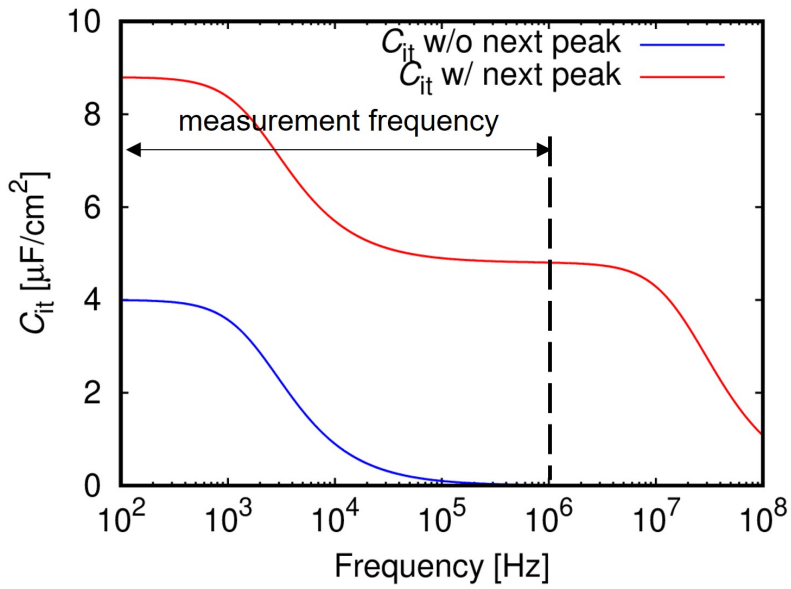

Figure 3.26: The calculated C_{it} as functions of the frequency.

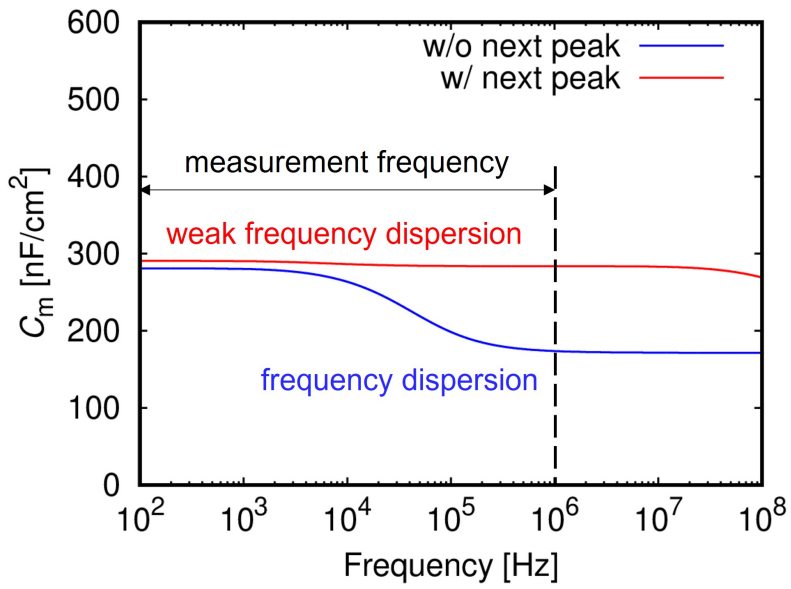

Figure 3.27: The calculated C_{m} as functions of the frequency.

On the other hand, we do not observe the second step of the C-V characteristics for the NiO_x IL shown in Fig. 3.18, indicating that electron trapping at the interface traps does not take place. This is owing to weak effects of G_{it} and D_{it} in the measurement frequency range, because of the peak frequency of G_{it}/ω in the

100 Hz range and the small peak value due to the low D_{it}. Thus, it is possible to conclude that the AlO_x and NiO_x ILs suppress the interface trap density.

Chapter 4

Conclusion and future perspectives

4.1 Conclusion of this work

In this work, we systematically investigated effects of metal-semiconductor or insulator-semiconductor interfacial layers (ILs) in AlGaN/GaN devices, where AlO_x, TiO_x, or NiO_x is employed as an IL. From capacitance-voltage characteristics of metal/IL/AlGaN/GaN devices, it is shown that the metal-AlGaN IL leads to modulation of the threshold voltage V_{th}, attributed to the vacuum level step induced by the IL dipole. We find negative vacuum level steps for AlO_x and TiO_x, and positive for NiO_x, from which the IL dipole density is estimated, indicating that the AlO_x/AlGaN and TiO_x/AlGaN interfaces are nearly neutral, while the NiO_x/AlGaN interface is negatively charged. From Hall measurements, we find that the 2DEG carrier concentration in the metal/IL/AlGaN/GaN devices is also modulated by the vacuum level step. In addition the these results, we also carried out X-ray photoelectron spectroscopy (XPS) to examine the reaction at the IL/AlGaN interface. we find an increase in Ni-Ga bonding at the NiOx/AlGaN interface, suggesting the existence of ionized VGa acceptors, which lead to the negatively charged NiOx/AlGaN interface. On the other hand, from capacitance-voltage characteristics of metal/Al_2O_3/IL/AlGaN/GaN devices, the

fixed charge density of the Al_2O_3/IL/AlGaN interface is evaluated. For AlO_x and TiO_x, the fixed charge density is increased in comparison with no IL, while decreased for NiO_x. The fixed charge density shows a positive correlation with the IL dipole density, suggesting that the fixed charge is related to the unbalanced IL dipole. Furthermore, using the conductance method, we show that it is possible to obtain small trap densities of metal/Al_2O_3/IL/AlGaN interfaces, comparing to the interface with no IL.

4.2 Future perspectives of this work

Although we find a correlation between the IL dipole density and fixed charge density, the relation between the dipole density and the insulator- semiconductor band offset remains unclear due to the large uncertainty in the intercept of the Al_2O_3 thickness dependence of V_{th}. Experiments using very small insulator thickness are necessary to improve the accuracy in the intercept extraction. Moreover, utilizing the V_{th} modulation by ILs, we should be able to carry out a normally-off operation for AlGaN/GaN MIS-FETs, where ILs such as TiO_x can be employed for access region to reduce series resistance, while ILs such as NiO_x can be employed for gate region to shift V_{th} positively in order to achieve normally-off.

Appendix A

Band diagram calculation

A.1 metal/IL/AlGaN/GaN band diagram

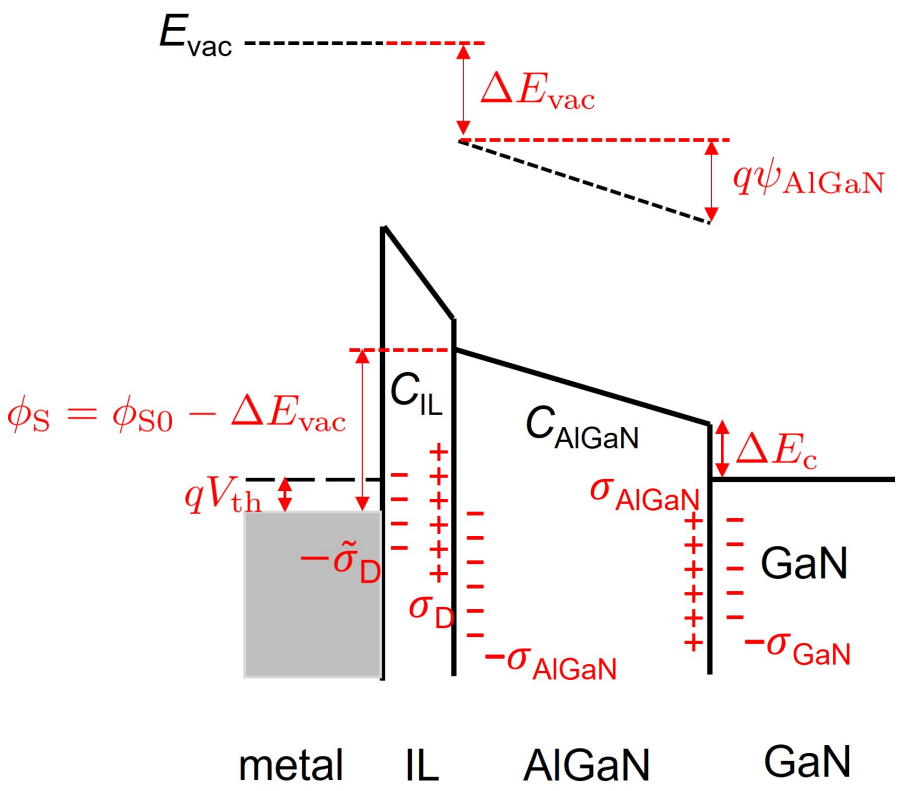

Figure A.1: Theoretical band diagram of the metal/IL/AlGaN/GaN devices under $V_{\text{G}} = V_{\text{th}}$.

Figure A.1 shows the theoretical band diagram of the metal/IL/AlGaN/GaN devices at gate voltage $V_G = V_{th}$, where ϕ_{S0} is the barrier height with no vacuum level step, ϕ_S is the effective barrier height, ΔE_c is the AlGaN-GaN conduction band offset, ψ_{AlGaN} is the total potential change through the AlGaN layer, $\sigma_{GaN}/q \simeq 2.1 \times 10^{13}$ cm^{-2} and $\sigma_{AlGaN}/q \simeq 3.2 \times 10^{13}$ cm^{-2} give the polarization charge densities [79–83], and σ_D is the IL dipole density.

Based on the 1-dimension Poisson equation, the potential ψ inside the IL or AlGaN is given by

$$\frac{\partial^2 \psi}{\partial x^2} = -\frac{\rho}{\varepsilon}. \tag{A.1}$$

Taking the integral of Eq. A.1, we have

$$\frac{\partial \psi}{\partial x} = F, \tag{A.2}$$

where F is the electric field strength inside the IL or AlGaN. We assume that the IL dipole and the polarization charge are at and/or near the interface, thereby we can apply Gauss law. Figure A.2 shows a Gauss box covering both AlGaN and GaN, determining the electric field inside the AlGaN F_{AlGaN}, and the electric field inside the GaN F_{GaN},

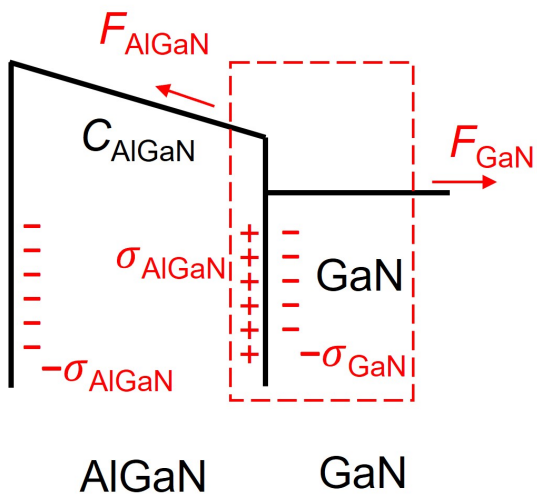

Figure A.2: Applying Gauss box in band diagram for AlGaN/GaN.

with a total charge inside the box $\rho = \sigma_{AlGaN} - \sigma_{GaN}$. Based on the Gauss

equation, we have

$$F_{\mathrm{AlGaN}} - F_{\mathrm{GaN}} = \frac{\rho}{\varepsilon} = \frac{\sigma_{\mathrm{AlGaN}} - \sigma_{\mathrm{GaN}}}{\varepsilon} = \frac{\sigma_{\mathrm{AlGaN}} - \sigma_{\mathrm{GaN}}}{k_{\mathrm{AlGaN}}\varepsilon_0}, \tag{A.3}$$

where k_{AlGaN} is the dielectric constant of AlGaN. For GaN part, since $V_{\mathrm{G}} = V_{\mathrm{th}}$, the 2DEG is completely depleted, lead to a flat band in GaN where $F_{\mathrm{GaN}} = 0$ Therefore, we have the total potential change through the AlGaN layer

$$\psi_{\mathrm{AlGaN}} = F_{\mathrm{AlGaN}} d_{\mathrm{AlGaN}} = \frac{\sigma_{\mathrm{AlGaN}} - \sigma_{\mathrm{GaN}}}{k_{\mathrm{AlGaN}}\varepsilon_0} d_{\mathrm{AlGaN}} = \frac{\sigma_{\mathrm{AlGaN}} - \sigma_{\mathrm{GaN}}}{C_{\mathrm{AlGaN}}}. \tag{A.4}$$

The same analysis can be applied for the IL/AlGaN/GaN as shown in Fig. A.3. Assuming no bulk charge inside the ILs. the total charge inside the box is $\rho = \sigma_{\mathrm{D}} - \sigma_{\mathrm{AlGaN}} + \sigma_{\mathrm{AlGaN}} - \sigma_{\mathrm{GaN}} = \sigma_{\mathrm{D}} - \sigma_{\mathrm{GaN}}$, where the polarization in the AlGaN cancels out. Therefore, we obtain the total potential change through the ILs, namely the vacuum level step

$$\Delta E_{\mathrm{vac}}/q = \frac{\sigma_{\mathrm{D}} - \sigma_{\mathrm{GaN}}}{C_{\mathrm{IL}}}. \tag{A.5}$$

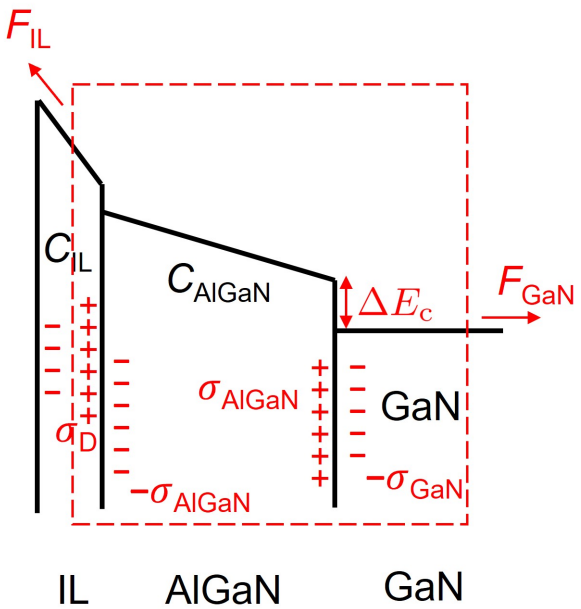

Figure A.3: Applying Gauss box in band diagram for IL/AlGaN/GaN.

Using these results and Figure A.1, we obtain

$$\begin{aligned} V_{\mathrm{th}} &= \frac{\phi_{\mathrm{S0}}}{q} - \frac{\Delta E_{\mathrm{vac}}}{q} - \psi_{\mathrm{AlGaN}} - \frac{\Delta E_{\mathrm{C}}}{q} \\ &= \frac{\phi_{\mathrm{S0}}}{q} - \frac{\sigma_{\mathrm{D}} - \sigma_{\mathrm{GaN}}}{C_{\mathrm{IL}}} - \frac{\sigma_{\mathrm{AlGaN}} - \sigma_{\mathrm{GaN}}}{C_{\mathrm{AlGaN}}} - \frac{\Delta E_{\mathrm{C}}}{q} \end{aligned} \tag{A.6}$$

for the metal/IL/AlGaN/GaN devices.

A.2 metal/Al_2O_3/IL/AlGaN/GaN band diagram

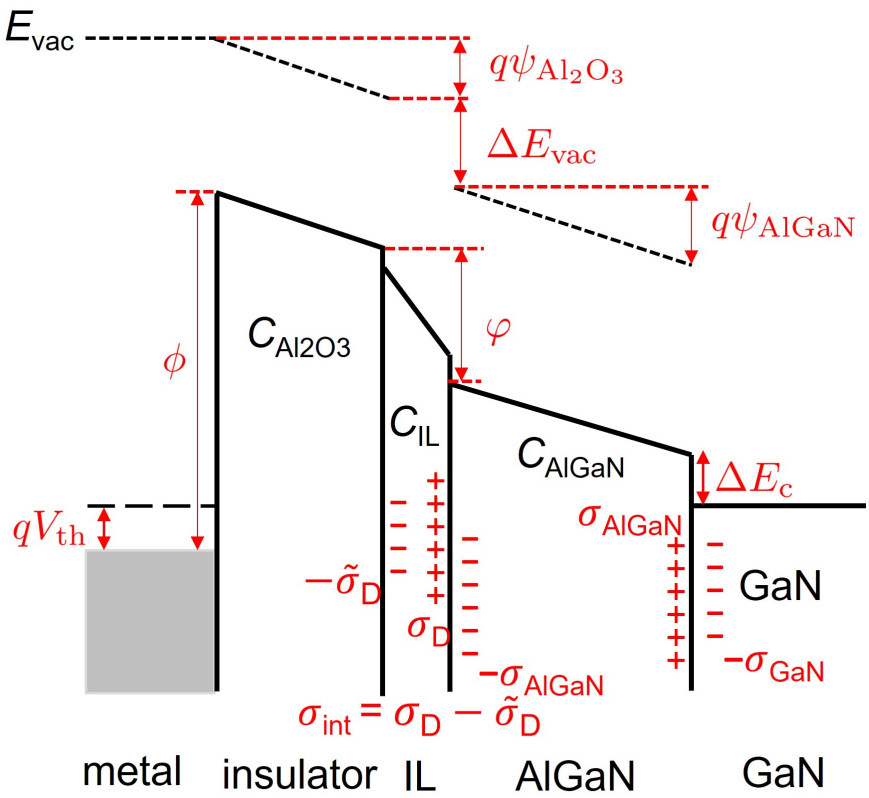

Figure A.4: Theoretical band diagram of the metal/Al_2O_3/IL/AlGaN/GaN devices under $V_{\mathrm{G}} = V_{\mathrm{th}}$.

Figure A.4 shows the theoretical band diagram of the metal/Al_2O_3/IL/AlGaN/GaN devices at gate voltage $V_{\mathrm{G}} = V_{\mathrm{th}}$, where where $C_{\mathrm{Al_2O_3}} = k_{\mathrm{Al_2O_3}}\varepsilon_0/d_{\mathrm{Al_2O_3}}$ is the Al_2O_3 capacitance given by the Al_2O_3 dielectric constant $k_{\mathrm{Al_2O_3}}$ and the thickness $d_{\mathrm{Al_2O_3}}$, ϕ is the metal-Al_2O_3 barrier height, φ is the effective Al_2O_3-AlGaN

conduction band offset, ψ_{AlGaN} is the total potential change through the AlGaN layer, $\psi_{\mathrm{Al_2O_3}}$ is the total potential change through the Al_2O_3 layer, $\sigma_{\mathrm{int}} = \sigma_{\mathrm{D}} - \widetilde{\sigma}_{\mathrm{D}}$ is the fixed charge density of the Al_2O_3/IL/AlGaN interface due to the unbalanced IL dipole. A similar analysis in the previous section can be allied toAl_2O_3/IL/AlGaN/GaN assuming no bulk charge inside the Al_2O_3 as shown in Fig. A.5. The total charge inside the box is now $\rho = \sigma_{\mathrm{D}} - \widetilde{\sigma}_{\mathrm{D}} - \sigma_{\mathrm{GaN}} = \sigma_{\mathrm{int}} - \sigma_{\mathrm{GaN}}$, where the polarization in the AlGaN cancels out while the IL dipole does not due to the unbalance. Therefore, we obtain the total potential change through the Al_2O_3

$$\psi_{\mathrm{Al_2O_3}} = F_{\mathrm{Al_2O_3}} d_{\mathrm{Al_2O_3}} = \frac{\sigma_{\mathrm{int}} - \sigma_{\mathrm{GaN}}}{k_{\mathrm{Al_2O_3}} \varepsilon_0} d_{\mathrm{Al_2O_3}}. \tag{A.7}$$

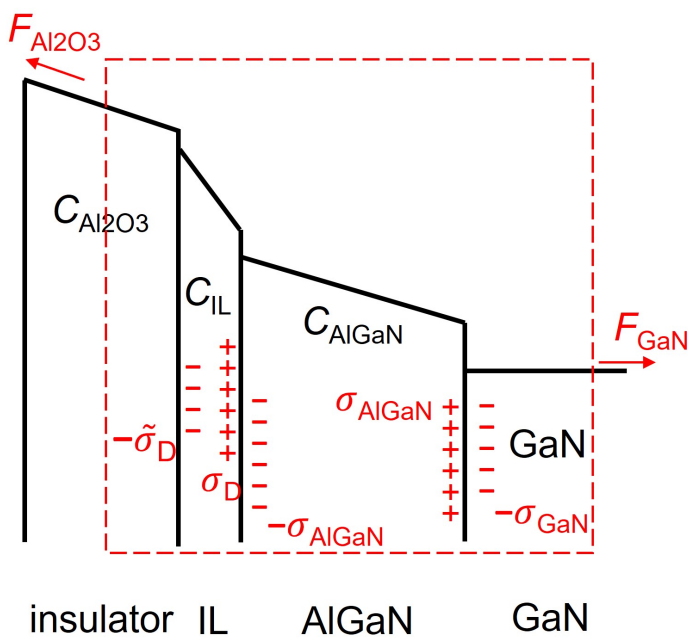

Figure A.5: Applying Gauss box in band diagram for Al_2O_3/IL/AlGaN/GaN.

Using these results and Figure A.4, we obtain

$$\begin{aligned} V_{\mathrm{th}} &= \frac{\phi}{q} - \psi_{\mathrm{Al_2O_3}} - \frac{\varphi}{q} - \psi_{\mathrm{AlGaN}} - \frac{\Delta E_{\mathrm{C}}}{q} \\ &= \frac{\sigma_{\mathrm{GaN}} - \sigma_{\mathrm{int}}}{k_{\mathrm{Al_2O_3}} \epsilon_0} d_{\mathrm{Al_2O_3}} - \frac{\sigma_{\mathrm{AlGaN}} - \sigma_{\mathrm{GaN}}}{C_{\mathrm{AlGaN}}} + \frac{\phi - \varphi - \Delta E_{\mathrm{C}}}{q}, \end{aligned} \tag{A.8}$$

for the metal/Al_2O_3/IL/AlGaN/GaN devices.

Appendix B

Conductance method

B.1 AC admittance affected by interface traps

At an insulator-semiconductor interface, an interface trap with a electron occupation probability P at energy E, as shown in Fig. B.1, is given by a time-dependent rate equation

$$\frac{\partial P}{\partial t} = \gamma(1-P)n - \alpha P, \tag{B.1}$$

where n is the semiconductor electron density at the interface, and γ and α are proportional constants. In Eq. B.1, the first term is related to the electron trapping, while the second term is related to the detrapping. The constant γ is given by

$$\gamma = v_{\mathrm{th}}\sigma \tag{B.2}$$

where v_{th} is the electron thermal velocity and σ is the electron capture cross-section.

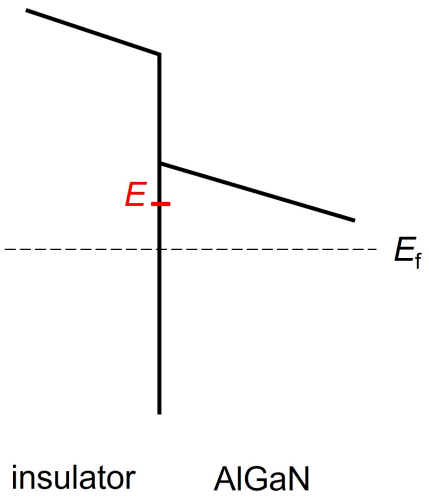

Figure B.1: A trapped electron at energy E at the insulator-semiconductor interface.

If we separate P, n and surface potential V into two contributions, form direct current (DC) parts and alternative current (AC) parts receptively, we obtain

$$\begin{aligned} P &= P_0 + \widetilde{P}\exp(j\omega t) \\ n &= n_0 + \widetilde{n}\exp(j\omega t) \\ V &= V_0 + \widetilde{V}\exp(j\omega t). \end{aligned} \tag{B.3}$$

The P_0 component at energy E is given by Fermi-Dirac distribution

$$P_0(E) = \frac{1}{1+\exp[(E-E_\mathrm{f})/k_\mathrm{B}T]}. \tag{B.4}$$

Thus, we have

$$\begin{aligned} \frac{dP_0}{dE} &= -\frac{\exp[(E-E_\mathrm{f})/k_\mathrm{B}T]/k_\mathrm{B}T}{(1+\exp[(E-E_\mathrm{f})/k_\mathrm{B}T])^2} \\ &= -\frac{P_0(1-P_0)}{k_\mathrm{B}T}. \end{aligned} \tag{B.5}$$

Substitute the DC components into Eq. B.1, we obtain

$$\alpha = \gamma n_0(1-P_0)/P_0 = \frac{1-P_0}{\tau P_0}, \quad \text{with } \tau = \frac{1}{\gamma n_0}. \tag{B.6}$$

In the range of small AC signal modulation, α is approximated to Eq. B.6. From Eq. B.1, we can obtain

$$j\omega\widetilde{P}\exp(j\omega t) = \gamma(1-P)n - \frac{(1-P_0)P}{\tau P_0}. \tag{B.7}$$

The right hand side of Eq. B.7 equals to

$$\begin{aligned}
&\gamma(1-P)n - \frac{(1-P_0)P}{\tau P_0} = \frac{\gamma(1-P)n\tau P_0 - (1-P_0)P}{\tau P_0} \\
&= \frac{[1-P_0-\widetilde{P}\exp(j\omega t)][n_0+\widetilde{n}\exp(j\omega t)]P_0/n_0 - (1-P_0)(P_0+\widetilde{P}\exp(j\omega t))}{\tau P_0} \\
&= \frac{\widetilde{n}P_0/n_0 - P_0^2\widetilde{n}/n_0 - \widetilde{P} - \widetilde{P}\widetilde{n}P_0\exp(j\omega t)/n_0}{\tau P_0}\exp(j\omega t) \\
&= \frac{P_0(1-P_0)\widetilde{n}/n_0 - \widetilde{P}[\widetilde{n}P_0\exp(j\omega t)/n_0+1]}{\tau P_0}\exp(j\omega t).
\end{aligned} \tag{B.8}$$

In case of small AC signal modulation, we have $\widetilde{n} \ll n_0$, thus $\widetilde{n}P_0\exp(j\omega t/n_0) \ll 1$. With this approximation, Eq. B.7 turns into

$$j\omega\widetilde{P}\exp(j\omega t) \simeq \frac{P_0(1-P_0)\widetilde{n}/n_0 - \widetilde{P}}{\tau P_0}\exp(j\omega t). \tag{B.9}$$

We can rewrite Eq. B.9 as

$$\widetilde{P} \simeq \frac{P_0(1-P_0)}{1+j\omega\tau P_0}\frac{\widetilde{n}}{n_0} = \frac{P_0(1-P_0)}{1+j\omega\tau P_0}\frac{q\widetilde{V}}{k_\mathrm{B}T}, \tag{B.10}$$

at temperature T where k_B is Boltzmann constant. The total small signal AC admittance Y_i is calculated by taking sum over all interface traps, i.e.

$$\begin{aligned}
Y_\mathrm{i} &= G_\mathrm{it} + jC_\mathrm{it}\omega \\
&= \frac{j\omega q}{\widetilde{V}}\int D_\mathrm{it}(E)\widetilde{P}dE \\
&= \frac{j\omega q^2}{k_\mathrm{B}T}\int \frac{D_\mathrm{it}(E)P_0(1-P_0)}{1+j\omega\tau P_0}dE \\
&= j\omega q^2\int \frac{D_\mathrm{it}(E)}{1+j\omega\tau P_0}\left(-\frac{dP_0}{dE}\right)dE,
\end{aligned} \tag{B.11}$$

with interface trap density D_it.

AC admittance for the low temperature limit

For low temperature, we have the approximation

$$-\frac{dP_0}{dE} \simeq \delta(E-E_\mathrm{f}). \tag{B.12}$$

Substitute into Eq. B.11, we have

$$\begin{aligned} G_{\mathrm{it}} + jC_{\mathrm{it}}\omega &= j\omega q^2 \int \frac{D_{\mathrm{it}}(E)}{1 + j\omega\tau P_0} \left(-\frac{dP_0}{dE}\right) dE \\ &\simeq \frac{j\omega q^2 D_{\mathrm{it}}(E_{\mathrm{f}})}{1 + j\omega\tau/2} \end{aligned} \tag{B.13}$$

Extract G_{it} and C_{it}, we obtain

$$\begin{aligned} \frac{G_{\mathrm{it}}}{\omega} &= \frac{\omega\tau q^2 D_{\mathrm{it}}}{2(1 + \omega^2\tau^2/4)} \\ C_{\mathrm{it}} &= \frac{q^2 D_{\mathrm{it}}}{1 + \omega^2\tau^2/4}. \end{aligned} \tag{B.14}$$

AC admittance for a discrete interface trap

For a discrete interface trap, the interface trap density D_{it} becomes the delta function of the energy, i.e.

$$D_{\mathrm{it}}(E) = D_0\ \delta(E - E_0). \tag{B.15}$$

Substitute into Eq. B.11, we have

$$\begin{aligned} G_{\mathrm{it}} + jC_{\mathrm{it}}\omega &= j\omega q^2 \int \frac{D_{\mathrm{it}}(E)}{1 + j\omega\tau P_0} \left(-\frac{dP_0}{dE}\right) dE \\ &= \frac{j\omega q^2 D_0}{1 + j\omega\tau P_0(E_0)} \frac{\exp[(E_0 - E_{\mathrm{f}})/k_{\mathrm{B}}T]}{k_{\mathrm{B}}T(1 + \exp[(E_0 - E_{\mathrm{f}})/k_{\mathrm{B}}T])^2} \\ &= \frac{j\omega q^2 D_0}{4k_{\mathrm{B}}T(1 + j\omega\tau/2)}. \quad (\text{for } E_{\mathrm{f}} = E_0) \end{aligned} \tag{B.16}$$

Extract G_{it} and C_{it}, we obtain

$$\begin{aligned} \frac{G_{\mathrm{it}}}{\omega} &= \frac{\omega\tau q^2 D_0}{8k_{\mathrm{B}}T(1 + \omega^2\tau^2/4)} \\ C_{\mathrm{it}} &= \frac{q^2 D_0}{4k_{\mathrm{B}}T(1 + \omega^2\tau^2/4)}. \end{aligned} \tag{B.17}$$

AC admittance for general continuous interface traps

For general continuous interface traps, the interface trap density D_{it} becomes a constant, not dependent of the energy. Equation B.11 now is

$$\begin{aligned} G_{\mathrm{it}} + jC_{\mathrm{it}}\omega &= j\omega q^2 \int \frac{D_{\mathrm{it}}(E)}{1+j\omega\tau P_0}\left(-\frac{dP_0}{dE}\right) dE \\ &\simeq j\omega q^2 D_{\mathrm{it}} \int \frac{1}{1+j\omega\tau P_0}\left(-\frac{dP_0}{dE}\right) dE \\ &= j\omega q^2 D_{\mathrm{it}} \int_0^1 \frac{dP_0}{1+j\omega\tau P_0} \\ &= \frac{q^2 D_{\mathrm{it}} \ln\left(1+j\omega\tau\right)}{\tau} \end{aligned} \tag{B.18}$$

Extract G_{it} and C_{it}, we obtain

$$\frac{G_{\mathrm{it}}}{\omega} = \frac{q^2 D_{\mathrm{it}} \ln(1+\omega^2\tau^2)}{2\omega\tau} \tag{B.19}$$

$$C_{\mathrm{it}} = \frac{q^2 D_{\mathrm{it}} \mathrm{atan}(\omega\tau)}{\omega\tau} \tag{B.20}$$

which we employed in Chapter 3. The time constant τ is

$$\tau(E_{\mathrm{f}}) = \frac{1}{\gamma n_0(E_{\mathrm{f}})} = \frac{\exp\left[(E_{\mathrm{c}} - E_{\mathrm{f}})/k_{\mathrm{B}}T\right]}{v_{\mathrm{th}}\sigma N_{\mathrm{c}}} \propto \exp\left(\frac{E_{\mathrm{c}} - E_{\mathrm{f}}}{k_{\mathrm{B}}T}\right). \tag{B.21}$$

B.2 AC admittance in equivalent circuits for MIS devices

Without considering the interface traps, Fig. B.2 shows the equivalent circuit of a metal/Al_2O_3/IL/AlGaN/GaN device, where we have

$$V_{\mathrm{G}} = \frac{qn_{\mathrm{s}}}{C_{\mathrm{tot}}} = qn_{\mathrm{s}}\left(\frac{1}{C_{\mathrm{Al_2O_3}}} + \frac{1}{C_{\mathrm{IL}}} + \frac{1}{C_{\mathrm{AlGaN}}}\right) \tag{B.22}$$

by assuming a linear relation between qn_{s} and V_{G}.

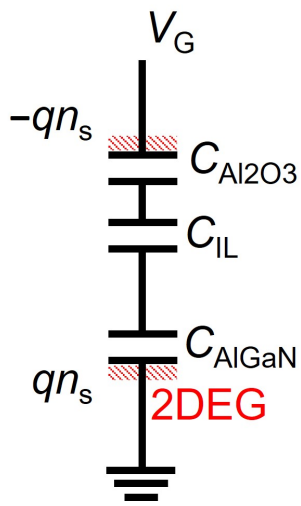

Figure B.2: The equivalent circuit of a metal/Al_2O_3/IL/AlGaN/GaN device without considering the interface traps.

On the other hand, by assuming an additional trapped electron density n_{it} at the IL/AlGaN interface due to the insulator-semiconductor interface traps, the equivalent circuit of a metal/Al_2O_3/IL/AlGaN/GaN device is reconstructed as shown in Fig. B.3. V_{G} is now given by

$$V_{\mathrm{G}} = \frac{q(n_{\mathrm{s}} + n_{\mathrm{it}})}{\widetilde{C}_{\mathrm{tot}}} = q(n_{\mathrm{s}} + n_{\mathrm{it}}) \left(\frac{1}{C_{\mathrm{Al_2O_3}}} + \frac{1}{C_{\mathrm{IL}}} \right) + \frac{qn_{\mathrm{s}}}{C_{\mathrm{AlGaN}}}. \tag{B.23}$$

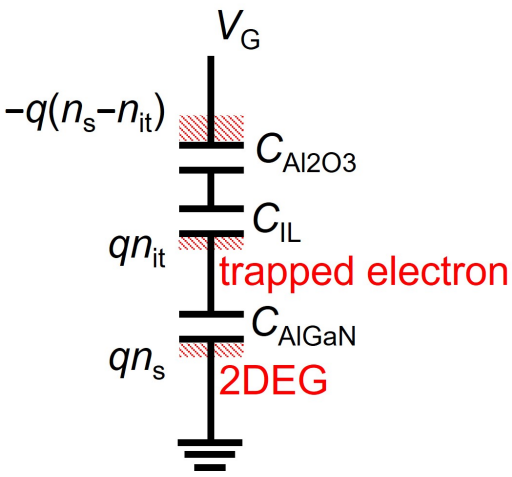

Figure B.3: The equivalent circuit of a metal/Al_2O_3/IL/AlGaN/GaN device considering the interface traps.

Thus, the total capacitance is now given by

$$\begin{aligned}\frac{1}{\widetilde{C}_{\mathrm{tot}}} &= \left(\frac{1}{C_{\mathrm{Al_2O_3}}} + \frac{1}{C_{\mathrm{IL}}}\right) + \frac{qn_{\mathrm{s}}}{q(n_{\mathrm{s}} + n_{\mathrm{it}})C_{\mathrm{AlGaN}}} \\ &= \left(\frac{1}{C_{\mathrm{Al_2O_3}}} + \frac{1}{C_{\mathrm{IL}}}\right) + \frac{1}{C_{\mathrm{AlGaN}} + (n_{\mathrm{it}}/n_{\mathrm{s}})C_{\mathrm{AlGaN}}} \\ &= \left(\frac{1}{C_{\mathrm{Al_2O_3}}} + \frac{1}{C_{\mathrm{IL}}}\right) + \frac{1}{C_{\mathrm{AlGaN}} + C_{\mathrm{it}}}.\end{aligned} \tag{B.24}$$

This result indicates that there is an additional capacitance contributed by the interface traps $C_{\mathrm{it}} = (n_{\mathrm{it}}/n_{\mathrm{s}})C_{\mathrm{AlGaN}}$, being parallel to the AlGaN capacitance. If we consider the contribution from interface traps as an AC admittance, the equivalent circuit of a metal/Al_2O_3/IL/AlGaN/GaN device can be reconstructed as shown in Fig. B.4, which we employed in Chapter 3.

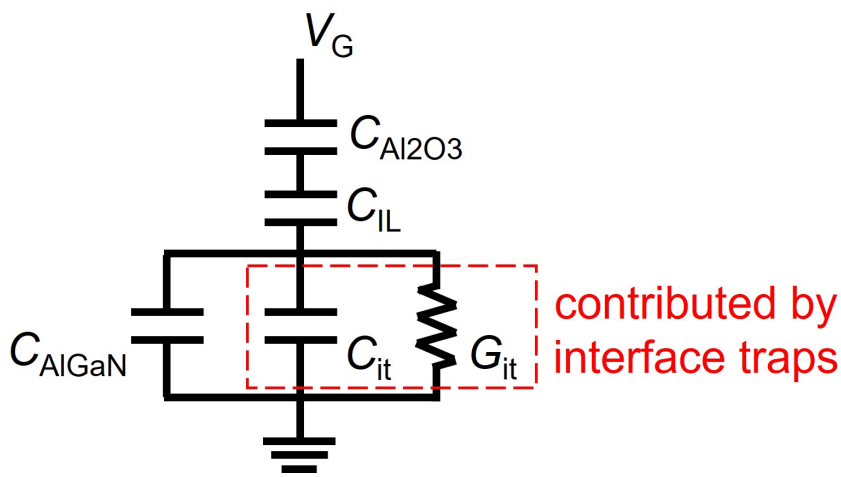

Figure B.4: The reconstructed equivalent circuit of a metal/Al_2O_3/IL/AlGaN/GaN device considering the interface traps.

List of publications

Journal

[1] Duong Dai Nguyen, Takehiro Isoda, Yuchen Deng, and Toshi-kazu Suzuki, "Normally-off operations in partially-gate-recessed AlTiO/AlGaN/GaN field-effect transistors based on interface charge engineering", Journal of Applied Physics **130** (1), 014503, 2021.

[2] Kazuya Uryu, Yuchen Deng, Son Phuong Le and Toshi-kazu Suzuki, "Electron mobility enhancement in n-GaN under Ohmic-metal", AIP Advances **13**, 075002, 2023.

[3] Duong Dai Nguyen, Yuchen Deng, and Toshi-kazu Suzuki, "Low-frequency noise in AlTiO/AlGaN/GaN metal-insulator-semiconductor field-effect transistors with non-gate-recessed or partially-gate-recessed structures", Semiconductor Science and Technology **38**, 095010, 2023.

[4] Yuchen Deng, Jieensi Gelan, Kazuya Uryu and Toshi-kazu Suzuki, "AlGaN/GaN devices with metal-semiconductor or insulator-semiconductor interfacial layers: Vacuum level step due to dipole and interface fixed charge ", Journal of Applied Physics **135**, 084504, 2024.

Conference

[1] Hirotomo Demura, Yuchen Deng, Duong Dai Nguyen, and Toshi-kazu Suzuki, "Threshold voltages of AlGaN/GaN metal-insulator-semiconductor devices with AlN or Al2O3 gate insulators", 46th Int. Symp. on Compound Semiconductors, TuB1-6, oral presentation (2019).

[2] Duong Dai Nguyen, Yuchen Deng, and Toshi-kazu Suzuki, "Impacts of nitrogen plasma surface cleaning on threshold voltages of AlTiO/AlGaN/GaN MIS devices", 51st Int. Conf. on Solid State Devices and Materials, PS-4-17, poster presentation (2019).

[3] Takehiro Isoda, Jumpei Shimura, Duong Dai Nguyen, Yuchen Deng, and Toshi-kazu Suzuki, "Threshold voltage control in AlGaN/GaN MIS devices with AlTiO gate insulators and gate-recess structures", The papers of technical meeting on electron devices, IEE Japan, EDD-21-032, oral presentation (2021).

[4] Duong Dai Nguyen, Takehiro Isoda, Yuchen Deng, and Toshi-kazu Suzuki, "Interface-charge-engineered normally-off AlTiO/AlGaN/GaN field-effect transistors", 82nd JSAP Autumn Meeting, 13a-N305-4, oral presentation (2021).

[5] Hideyuki Matsuyama, Yuchen Deng, and Toshi-kazu Suzuki, "Effects of insulator/semiconductor interfacial layer insertion in AlGaN/GaN MIS devices with AlN gate insulators ", The papers of technical meeting on electron devices, IEE Japan, EDD-22-021, oral presentation (2022).

[6] Yuchen Deng, Hibiki Anaba, Hideyuki Matsuyama, Kazuya Uryu and Toshi-kazu Suzuki, "Effects of AlN/AlGaN interfacial control layers in AlN/AlGaN/GaN devices", 2022 JAIST international Symposium Quantum Devices and Metrologies, poster presentation (2022).

[7] Kazuya Uryu, Yuchen Deng, Son Phuong Le and Toshi-kazu Suzuki, "Electron mobility enhancement in n-GaN under Ohmic-metal", 70th JSAP Spring Meeting, 17p-A301-14, oral presentation (2023).

[8] Kazuya Uryu, Yuchen Deng, Son Phuong Le and Toshi-kazu Suzuki, "Electron mobility enhancement in n-GaN under Ohmic-metal: characterization by multi-probe-Hall measurement ", The papers of technical meeting on electron devices, IEE Japan, EDD-23-024, oral presentation (2023).

[9] Kazuya Uryu, Yuchen Deng, and Toshi-kazu Suzuki, "Characterization of recess Ohmic contact to AlGaN/GaN heterostructure using single or hybrid electrode structures", 84th JSAP Autumn Meeting, 22p-B201-12, oral presen-

tation (2023).

[10] Kazuya Uryu, Yuchen Deng, and Toshi-kazu Suzuki, "Recess Ohmic contact to AlGaN/GaN heterostructure using single or hybrid electrode structures", 55th Int. Conf. on Solid State Devices and Materials, N-3-04, oral presentation (2023).

[11] Yuchen Deng, Jieensi Gelan, Kazuya Uryu and Toshi-kazu Suzuki, "Threshold Voltage Modulation of AlGaN/GaN Devices via Vacuum Level Step Control Using Thin Oxide Interlayers", 2023 International Workshop on Dielectric Thin Films for Future Electron Devices – Science and Technology –, S6-2, oral presentation (2023).

Award

[1] **Student Poster Presentation Award for**

Yuchen Deng, Hibiki Anaba, Hideyuki Matsuyama, Kazuya Uryu and Toshi-kazu Suzuki, "Effects of AlN/AlGaN interfacial control layers in AlN/AlGaN/GaN devices", 2022 JAIST international Symposium Quantum Devices and Metrologies, poster presentation (2022).

[2] **IWDTF Young Researcher Award for**

Yuchen Deng, Jieensi Gelan, Kazuya Uryu and Toshi-kazu Suzuki, "Threshold Voltage Modulation of AlGaN/GaN Devices via Vacuum Level Step Control Using Thin Oxide Interlayers", 2023 International Workshop on Dielectric Thin Films for Future Electron Devices – Science and Technology –, S6-2, oral presentation (2023).

Bibliography

[1] K. Benson, Analog Dialogue **51**, 45 (2017).

[2] Infineon, URL `https://www.infineon.com`.

[3] S. Colak, B. Singer, and E. Stupp, IEEE Electron Device Lett. **1**, 51 (1980).

[4] H. Kroemer, Proceedings of the IRE **45**, 1535 (1957).

[5] T. Mimura, S. Hiyamizu, T. Fujii, and K. Nanbu, Jpn. J. Appl. Phys. **19**, L225 (1980).

[6] Y. Ohno and M. Kuzuhara, IEEE Trans. Electron Devices **48**, 517 (2001).

[7] L. Wang, 25th International Conference on Microelectronics p. 576 (2006).

[8] I. Vurgaftman, J. R. Meyer, and L. R. Ram-Mohan, J. Appl. Phys. **89**, 5815 (2001).

[9] I. Vurgaftman and J. R. Meyer, J. Appl. Phys. **94**, 3675 (2003).

[10] E. O. Johnson, RCA Electronic Components and Devices **13**, 27 (1965).

[11] N. Tanaka, *Nitride compound semiconductor electronic device fabrication process and research on electron transport within the device* (2010).

[12] S. M. Sze and K. K. Ng, *Physics of Semiconductor Devices* (John Wiley & Sons, New Jersey, 2007).

[13] C. Bulutay, B. K. Ridley, and N. A. Zakhleniuk, Phys. Rev. B **62**, 15754 (2000).

[14] P. Barlow, R. Davis, and M. Lazarus, Proc. IEE **5**, 177 (1986).

[15] A. Nigam, T. N. Bhat, S. Rajamani, S. B. Dolmanan, S. Tripathy, and M. Kumar, AIP Adv. **7** (2017).

[16] I. P. T. Institute, URL `http://www.ioffe.ru/SVA/NSM/Semicond/GaN/index.html`.

[17] F. Bernardini, V. Fiorentini, and D. Vanderbilt, Phys. Rev. B **56**, R10024 (1997).

[18] O. Ambacher, B. Foutz, J. Smart, J. R. Shealy, N. G. Weimann, K. Chu, M. Murphy, A. J. Sierakowski, W. J. Schaff, L. F. Eastman, R. Dimitrov, A. Mitchell, and M. Stutzmann, J. Appl. Phys. **87**, 334 (2000).

[19] M. Khan, A. Bhattarai, J. Kuznia, and D. Olson, Appl. Phys. Lett. **63**, 1214 (1993).

[20] M. Asif Khan, J. N. Kuznia, D. T. Olson, W. J. Schaff, J. W. Burm, and M. S. Shur, Appl. Phys. Lett. **65**, 1121 (1994).

[21] S. Arulkumaran, T. Egawa, H. Ishikawa, and T. Jimbo, Appl. Phys. Lett. **82**, 3110 (2003).

[22] W. Xu, H. Rao, and G. Bosman, Appl. Phys. Lett. **100**, 223504 (2012).

[23] J.-J. Zhu, X.-H. Ma, B. Hou, W.-W. Chen, and Y. Hao, Appl. Phys. Lett. **104**, 153510 (2014).

[24] Y. Liu, J. A. Bardwell, S. P. McAlister, S. Rolfe, H. Tang, and J. B. Webb, Phys. Status Solidi C **0**, 69 (2002).

[25] N. Tsurumi, H. Ueno, T. Murata, H. Ishida, Y. Uemoto, T. Ueda, K. Inoue, and T. Tanaka, IEEE Trans. Electron Devices **57**, 980 (2010).

[26] S. Huang, Q. Jiang, S. Yang, C. Zhou, and K. Chen, IEEE Electron Device Lett. **33**, 516 (2012).

[27] V. Kumar, A. Kuliev, T. Tanaka, Y. Otoki, and I. Adesida, Electron. Lett. **39**, 1758 (2003).

[28] T. Oka and T. Nozawa, IEEE Electron Device Lett. **29**, 668 (2008).

[29] Yong Cai, Yugang Zhou, K. J. Chen, and K. M. Lau, IEEE Electron Device Lett. **26**, 435 (2005).

[30] X. Hu, G. Simin, J. Yang, M. Asif Khan, R. Gaska, and M. Shur, Electron. Lett. **36**, 753 (2000).

[31] Y. Uemoto, M. Hikita, H. Ueno, H. Matsuo, H. Ishida, M. Yanagihara, T. Ueda, T. Tanaka, and D. Ueda, IEEE Trans. Electron Devices **54**, 3393 (2007).

[32] N. Harada, Y. Hori, N. Azumaishi, K. Ohi, and T. Hashizume, Appl. Phys. Express **4**, 021002 (2011).

[33] C. Yadav, P. Kushwaha, S. Khandelwal, J. P. Duarte, Y. S. Chauhan, and C. Hu, IEEE Electron Device Lett. **35**, 612 (2014).

[34] Z. Lin, W. Lu, J. Lee, D. Liu, J. S. Flynn, and G. R. Brandes, Appl. Phys. Lett. **82**, 4364 (2003).

[35] G. Li, T. Zimmermann, Y. Cao, C. Lian, X. Xing, R. Wang, P. Fay, H. G. Xing, and D. Jena, IEEE Electron Device Lett. **31**, 954 (2010).

[36] C. T. Lee, Y.-J. Lin, and D.-S. Liu, Appl. Phys. Lett. **79**, 2573 (2001).

[37] K. A. Rickert, A. B. Ellis, F. J. Himpsel, J. Sun, and T. F. Kuech, Appl. Phys. Lett. **80**, 204 (2002).

[38] K. Isobe and M. Akazawa, AIP Adv. **8** (2018).

[39] C. Wang and X. Li, Appl. Surf. Sci. **622**, 156954 (2023).

[40] T. Hashizume, S. Ootomo, and H. Hasegawa, Appl. Phys. Lett. **83**, 2952 (2003).

[41] C. Liu, E. F. Chor, and L. S. Tan, Appl. Phys. Lett. **88**, 173504 (2006).

[42] A. Kawano, S. Kishimoto, Y. Ohno, K. Maezawa, T. Mizutani, H. Ueno, T. Ueda, and T. Tanaka, Phys. Status Solidi C **4**, 2700 (2007).

[43] S. Yagi, M. Shimizu, M. Inada, Y. Yamamoto, G. Piao, H. Okumura, Y. Yano, N. Akutsu, and H. Ohashi, Solid-State Electron. **50**, 1057 (2006).

[44] C. Gupta, S. H. Chan, A. Agarwal, N. Hatui, S. Keller, and U. K. Mishra, IEEE Electron Device Lett. **38**, 1575 (2017).

[45] D. Kikuta, K. Ito, T. Narita, and T. Kachi, Appl. Phys. Express **13**, 026504 (2020).

[46] S. P. Le, T. Ui, T. Q. Nguyen, H. A. Shih, and T. Suzuki, J. Appl. Phys. **119**, 204503 (2016).

[47] A. Colon, L. Stan, R. Divan, and J. Shi, J. Vac. Sci. Technol. A **35**, 01B132 (2017).

[48] S. P. Le, D. D. Nguyen, and T. Suzuki, J. Appl. Phys. **123**, 034504 (2018).

[49] S. Dutta Gupta, A. Soni, V. Joshi, J. Kumar, R. Sengupta, H. Khand,

B. Shankar, N. Mohan, S. Raghavan, N. Bhat, and M. Shrivastava, IEEE Trans. Electron Devices **66**, 2544 (2019).

[50] D. D. Nguyen and T. Suzuki, J. Appl. Phys. **127**, 094501 (2020).

[51] D. D. Nguyen, T. Isoda, Y. Deng, and T. Suzuki, J. Appl. Phys. **130**, 014503 (2021).

[52] D. D. Nguyen, Y. Deng, and T. Suzuki, Semicond. Sci. Technol. **38**, 095010 (2023).

[53] T. Sato, J. Okayasu, M. Takikawa, and T. Suzuki, IEEE Electron Device Lett. **34**, 375 (2013).

[54] M. Nozaki, K. Watanabe, T. Yamada, H.-A. Shih, S. Nakazawa, Y. Anda, T. Ueda, A. Yoshigoe, T. Hosoi, T. Shimura, and H. Watanabe, Jpn. J. Appl. Phys. **57**, 06KA02 (2018).

[55] J.-C. Gerbedoen, A. Soltani, M. Mattalah, M. Moreau, P. Thevenin, and J.-C. D. Jaeger, Diamond Relat. Mater. **18**, 1039 (2009).

[56] T. Q. Nguyen, H. A. Shih, M. Kudo, and T. Suzuki, Phys. Status Solidi C **10**, 1401 (2013).

[57] Y. Liu, J. Bardwell, S. McAlister, S. Rolfe, H. Tang, and J. Webb, Phys. Status Solidi C **0**, 69 (2003).

[58] H.-A. Shih, M. Kudo, M. Akabori, and T. Suzuki, Jpn. J. Appl. Phys. **51**, 02BF01 (2012).

[59] H.-A. Shih, M. Kudo, and T. Suzuki, Appl. Phys. Lett. **101**, 043501 (2012).

[60] H.-A. Shih, M. Kudo, and T. Suzuki, J. Appl. Phys. **116**, 184507 (2014).

[61] S. P. Le, T. Q. Nguyen, H. A. Shih, M. Kudo, and T. Suzuki, J. Appl. Phys. **116**, 054510 (2014).

[62] Y. L. Chiou and C. T. Lee, IEEE Trans. Electron Devices **58**, 3869 (2011).

[63] S. Ganguly, J. Verma, G. Li, T. Zimmermann, H. Xing, and D. Jena, Appl. Phys. Lett. **99**, 193504 (2011).

[64] M. Esposto, S. Krishnamoorthy, D. N. Nath, S. Bajaj, T.-H. Hung, and S. Rajan, Appl. Phys. Lett. **99**, 133503 (2011).

[65] M. Ťapajna and J. Kuzmík, Appl. Phys. Lett. **100**, 113509 (2012).

[66] J. Son, V. Chobpattana, B. M. McSkimming, and S. Stemmer, Appl. Phys. Lett. **101**, 102905 (2012).

[67] T. H. Hung, S. Krishnamoorthy, M. Esposto, D. N. Nath, P. S. Park, and S. Rajan, Appl. Phys. Lett. **102**, 072105 (2013).

[68] M. Ťapajna, M. Jurkovič, L. Válik, Š. Haščík, D. Gregušová, F. Brunner, E.-M. Cho, T. Hashizume, and J. Kuzmík, J. Appl. Phys. **116**, 104501 (2014).

[69] M. Matys, B. Adamowicz, A. Domanowska, A. Michalewicz, R. Stoklas, M. Akazawa, Z. Yatabe, and T. Hashizume, J. Appl. Phys. **120**, 225305 (2016).

[70] M. Ťapajna, L. Válik, F. Gucmann, D. Gregušová, K. Frohlich, Š. Haščík, E. Dobročka, L. Tóth, B. Pécz, and Kuzmík, J. Vac. Sci. Technol. B **35**, 01A107 (2017).

[71] G. Dutta, S. Turuvekere, N. Karumuri, N. DasGupta, and A. DasGupta, IEEE Electron Device Lett. **35**, 1085 (2014).

[72] Y. Li, Y. Guo, K. Zhang, X. Zou, J. Wang, Y. Kong, T. Chen, C. Jiang, G. Fang, C. Liu, et al., IEEE Trans. Electron Devices **64**, 3139 (2017).

[73] T. Sato, K. Uryu, J. Okayasu, M. Kimishima, and T. Suzuki, Appl. Phys. Lett. **113**, 063505 (2018).

[74] M. Akazawa and T. Hasezaki, **255**, 1700382 (2018).

[75] J. Koba and J. Koike, AIP Adv. **12** (2022).

[76] W. Choi, O. Seok, H. Ryu, H.-Y. Cha, and K.-S. Seo, IEEE Electron Device Lett. **35**, 175 (2013).

[77] T. E. Hsieh, E. Y. Chang, Y. Z. Song, Y. C. Lin, H. C. Wang, S. C. Liu, S. Salahuddin, and C. C. Hu, IEEE Electron Device Lett. **35**, 732 (2014).

[78] M. Hua, J. Wei, G. Tang, Z. Zhang, Q. Qian, X. Cai, N. Wang, and K. J. Chen, IEEE Electron Device Lett. **38**, 929 (2017).

[79] J. Garrido, J. Sanchez Rojas, A. Jimenez, E. Munoz, F. Omnes, and P. Gibart, Appl. Phys. Lett. **75**, 2407 (1999).

[80] O. Ambacher, B. Foutz, J. Smart, J. Shealy, N. Weimann, K. Chu, M. Murphy, A. Sierakowski, W. Schaff, L. Eastman, et al., J. Appl. Phys. **87**, 334

(2000).

[81] F. Bernardini, V. Fiorentini, and D. Vanderbilt, Phys. Rev. B **63**, 193201 (2001).

[82] E. Miller, E. Yu, C. Poblenz, C. Elsass, and J. Speck, Appl. Phys. Lett. **80**, 3551 (2002).

[83] A. Winzer, R. Goldhahn, G. Gobsch, A. Link, M. Eickhoff, U. Rossow, and A. Hangleiter, Appl. Phys. Lett. **86** (2005).

[84] S. Mohney and X. Lin, Journal of electronic materials **25**, 811 (1996).

[85] K. Schweitz and S. Mohney, J. Electron. Mater. **30**, 175 (2001).

[86] M. P. Seah and W. A. Dench, Surf. Interface Anal. **1**, 2 (1979).

[87] L. Pauling, *The Nature of the Chemical Bond* (Cornell University Press, 1960).

[88] E. H. Nicollian and J. R. Brews, *MOS (metal oxide semiconductor) physics and technology* (John Wiley & Sons, 2002).

[89] Y. Hori, Z. Yatabe, and T. Hashizume, J. Appl. Phys. **114** (2013).

Acknowledgment

First of all, I would like to express my sincere gratitude to Prof. Toshi-kazu Suzuki for guiding me through this work. I also want to express my thanks to Prof. Masashi Akabori for his support during my course, and to Prof. Toshu An for his instructions in both minor research and doctoral dissertation. Moreover, sincerely thanks to Prof. Eisuke Tokumitsu and Prof. Taketomo Sato for giving me very helpful instructions during my work on doctoral dissertation. Finally, Many thanks to my former and current lab members, Hirotomo Demura, Duong Dai Nguyen, Jumpei Shimura, Hideyuki Matsuyama, Hibiki Anaba, Jeensi Gelan and Kazuya Uryu for their kindly supports during experiments.